UNIVERSITÀ DI PARMA

Università degli Studi di Parma
Dottorato di Ricerca in
Ingegneria Civile e Architettura
Ciclo XXXIII°

A multi-scale approach to interpret Hot Mix Asphalt (HMA) creep behaviour at intermediate temperatures

PhD Dissertation

Coordinatore: Prof. Sandro Longo
Tutor: Prof. Antonio Montepara
Co-tutor: Dr. Elena Romeo

Candidato: Antonio Roberto

Anni accademici: 2017/2018 - 2019/2020

UNIVERSITÀ DI PARMA

Università degli Studi di Parma
Dottorato di Ricerca in Ingegneria Civile e Architettura
Ciclo XXXIII

A multi-scale approach to interpret Hot Mix Asphalt (HMA) creep behaviour at intermediate temperatures

PhD Dissertation

Coordinatore: Prof. Sandro Longo
Tutor: Prof. Antonio Montepara
Co-tutor: Dr. Elena Romeo

Candidato: Antonio Roberto

Anni accademici: 2017/2018 - 2019/2020

To Valentina and Elena

"Look deep into nature,
and then you will understand everything better."

Albert Einstein

Contents

List of Figures

List of Tables

Acknowledgement

This dissertation is the combination of several efforts. I perfectly remember the starting point of my Ph.D course experience, I had idea about the initial hypothesis but no ideas about its development. Due to this, I owe my huge gratitude to several people.

First of all, I have to say a huge thank you to my Tutor Prof. Antonio Montepara and Co-tutor Dr. Elena Romeo. I owe my thankfulness to you for supporting me during this 3-years period. Without your knowledge, experience and availability this research project would have been just a dream. I would like to say thank you also to Prof. Gabriele Tebaldi, who has given me the possibility to meet several expert-people worldwide. I owe my gratitude to you for several international opportunities.

I have to say thank you to Prof. Gordon D. Airey and Dr. Davide Lo Presti for hosting me at Nottingham Transportation Engineering Center (NTEC). I spent very special academic and every-day-life moments during my journey there. I would get the opportunity to say thank you to Dr. Ana Jiménez del Barco Carrión, Dr. Gustavo Menegusso Pires, and all the technicians (John, Martin, Lawrence, Richard and Margaret) for the laboratory support.

I want to say thank you to the Prof. Jan Król for our collaboration and also for inviting me at Warsaw University of Technology.

I owe gratitude to my parents and brothers for supporting me during my educational experiences and moments. I know it is difficult to better understand the explained topics.

A huge acknowledgement is for Valentina, who has supported and has been supporting me during this period. I have to say sorry for some difficult moments. Thank you to our daughter Elena, who has been giving us the opportunity to differently live and enjoy our life.

I would like to thank my colleagues Stefano, Bia and Francesco for the amazing collaboration and for developing awesome research and laboratory activities. Thank you for supporting me before and during my first English-conference-speech. Thank you to Michele Terzano who hugely helped me.

Thank you to all the people who I have met during this three-year-period. Thank you to all my friends in Parma and Laurino. Thank you to Jen and Josh for hosting me during my Nottingham-experience. I owe my gratefulness to you and to your families for adopting me. I will never stop to tell you: thank you. Thank you to all the Nottingham friends especially to both the Baptistes, Josh and Oli, for helping me.

Thank you Prof. Mario Tribaudino, Prof. Daniele Ferretti, Prof. Claudia Graiff, Dr. Luca Chiapponi, Dr. Luciana Mantovani, and Dr. Laura Bergamonti, to give me the opportunity of developing interdisciplinary activities.

The last but not least, thank you to the laboratory technicians, Andrea, Vittorio, Francisco, and Eustachio, who have helped me to develop all the home-made devices which I will explain into the following paragraphs.

Ringraziamenti

Questa tesi di dottorato è il risultato di diversi sforzizi. Ricordo perfettamente il momento iniziale del mio percorso formativo di dottorato, avevo idea delle ipotesi di base del mio progetto ma non ero assolutamente consapevole di quanto faticoso sarebbe stato il suo sviluppo. Pertanto, devo la mia gratitudine a molte persone.

Prima di tutto devo ringraziare il Tutor e il Co-tutor di questa tesi, rispettivamente il Prof. Antonio Montepara e la Dott.ssa Elena Romeo. Vi devo la mia gratitudine per avermi supportato durante tutto questo periodo formativo di 3 anni. Senza la vostra conoscenza, esperienza e disponibilità questa ricerca sarebbe stata solo un sogno. Vorrei ringraziare anche il Prof. Gabriele Tebaldi che mi ha dato la possibilita di conoscere diversi esperti mondiali. Vi sono grato per le diverse opportunità internazionali che mi avete dato.

Devo ringrazire il Prof. Gordon D. Airey e il Dott. Davide Lo Presti per avermi ospitato al Nottingham Transportation Engineering Center (NTEC). Ho trascorso meravigliose esperienze accademiche e di vita durante tutto il periodo di scambio. Vorrei cogliere l'occasione per ringraziare la Dott.ssa Ana Jiménez del Barco Carrión, il Dott. Gustavo Menegusso Pires, e tutti i tecnici (John, Martin, Lawrence, Richard e Margaret) per avermi aiutato nelle attività di laboratorio.

Ringrazio anche il Prof. Jan Król per la splendida collaborazione che abbiamo avuto e per avermi invitato a trascorrere un periodo di studio e approfondimento presso la Warsaw University of Technology.

Devo la mia gratitudine ai miei genitori e ai miei fratelli per avermi supportato e sopportato durante questo periodo. Lo so che è difficile per voi capire gli argomenti.

Un grande ringraziamento è per Valentina che mi ha supportato e continua a supportarmi. Scusami per alcuni momenti difficili. Grazie a nostra figlia Elena, che ci sta dando l'opportunità di godere e vivere in modo diverso i momenti della nostra vita.

Vorrei ringraziare anche i miei colleghi Stefano, Bia e Francesco per la fantastica collaborazione e per lo sviluppo di affascinanti attività di laboratorio. Grazie anche per avermi incoraggiato prima e durante il mio primo discorso in inglese. Grazie anche a Michele Terzano per avermi aiutato.

Grazie a tutte le persone nche ho incontrato in questi tre anni. Grazie a tutti gli amici di Parma e Laurino. Grazie a Jen e Josh per avermi ospitato durante la mia esperienza a Nottingham. Davvero grazie a voi e alle vostre famiglie per avermi adottato. Non smetterò mai di dirvi grazie. Grazie a tutti gli amici di Nottingham specialmente ai fratelli Baptiste, Josh e Oli.

Prof. Mario Tribaudino, Prof. Daniele Ferretti, Prof.ssa Claudia Graiff, Dott. Luca Chiapponi, Dott.ssa Luciana Mantovani, e Dott.ssa Laura Bergamonti, grazie per aver reso possibile lo sviluppo di diverse attività interdisciplinari.

L'ultimo grazie ma non meno importante degli altri va ai tecnici di laboratorio Andrea, Vittorio, Francisco ed Eustachio che mi hanno aiutato nello sviluppo delle strumentazioni che verrano descritte nei paragrafi seguenti.

Abstract

Nowadays, heavy traffic levels and climatic changes combination can lead to a premature pavement failure. This phenomenon is usually due to the accumulation of permanent deformations. In the last few years, the aptitude of hot mix asphalt (HMA) pavements to accumulate the permanent deformation has been linked to the asphalt binder behaviour. But, as it is deeply-rooted into the pavement-scientific community, the HMAs' "glue", the so called mastic, plays a key role on the mechanical and cracking behaviour of HMAs. The mastic is defined as the combination between filler (up to 0.075 mm) and the asphalt binder. Consequently, this dissertation try to open the possibility of studying the accumulation of the permanent deformations directly on mastics using a new tensile creep test. The pursuit of the proposed objective aims at introducing a multi-scale approach for the creep behaviour. Therefore, the mastics properties have been compared with the HMA cracking and mechanical behaviours to understand and distinguish the role of the mastic phase and its components on the performance level of the HMAs. In order to achieve the targeted aim, three different categories of fillers (by-product, conventional, and reclaimed) were involved in the research activities. The mentioned filler groups represent the Ladle Furnace Steel (LFS) slags, which were hydrated and not hydrated, the limestone and the limestone-based materials, and the Reclaimed Asphalt Pavement (RAP) (50% and 20% by the weight of the aggregates were used), respectively. Referring at the mixtures containing RAP, the reclaimed material was treated with the Waste Cooking Oil (WCO), which was used as rejuvenator. The mentioned materials were combined with two asphalt binders, neat and SBS modified, to prepare mastics and HMAs. To obtain the creep parameters, mastics were evaluated using the standard test MSCR at 64 °C, applying 3.20 kPa and 0.10 kPa as shear stresses, and a new experimental testing method performed at 7 °C using 60 N as tensile load, which was applied for 180 seconds. While, the HMAs were tested performing the Superpave protocol at 10 °C. Successively, the obtained parameters of mastics were compared with the energetic and the creep parameters of HMAs. The energetic characterization was done using the HMA fracture mechanic framework. The interpretation of the results showed that the mastic creep behaviour highly effects the capability of HMAs to dissipate energy during the stress condition, especially when the by-product materials are used.

Sommario

Oggi giorno, la combinazione tra incremento dei livelli di traffico e cambiamenti climatici spesso provoca la rottura prematura delle pavimentazioni stradali. Questo fenomeno è solitamente dovuto all'accumulo delle deformazioni permanenti. Negli ultimi anni, l'accumulo di tali deformazioni nelle pavimentazioni confezionate a caldo (HMA) è stato collegato al comportamento del legante bituminoso. Nella comunità scientifica è noto che il collagene, detto mastice per questo tipo di pavimentazioni, ha un ruolo importante sul coportament meccanico e a fessura delle HMA. Pertanto, questo progetto di ricerca si pone come obbiettivo primario lo studio dell'accumulo delle deformazioni permanenti direttamente sui mastici. Lo scopo principale di tale analisi è quello di proporre un modello interpretativo capace di correlare le proprietà di creep del mastice alla capacità dissipativa e meccanica delle miscele confezionate a caldo. Per poter raggiungere L'obiettivo prefissato, tre categorie di filler sono state impiegate: by-product, conventional, e reclaimed. Ognuno di questi rappresenta i seguenti materiali: Scorie di acciaieria, sia idratate che non idratate, materiale calcareo e a base di calcare, e il fresato d'asfalto (le percentuali ponderate sul peso degli aggregati sono state il 20% e il 50%). Questi matteriali sono stati poi mescolati sia con bitume naturale sia con bitume modificato per ottenere i campioni di mastice e HMA. I parametri necessari alla definizione del modello interpretativo sono stati ottenuti testando i mastici con un test standard chiamato MSCR a 64 °C, utilizzanto 3.20 kPa e 0.10 kPa come sforzo di taglio, e una nuova procedura di prova eseguita a 7 °C utilizzando come carico di trazione 60 N. Mentre le miscele di conglomerato sono state testate con utilizzando il protocollo Superpave a 10 °C. Successivamente i parametri dei mastici sono stati comparati alla capacità energetica, ottenuta utilizzando il HMA fracture mechanic framework, e meccanica dei conglomerati bituminosi. Le leggi interpretative del comportamento a creep sono state poi definite per ogni gruppo di filler, dimostrando che il mastice influisce sulla capacità dissipativa delle miscele in modo particolare quando i materiali by-product utilizzati vengo inclusi nelle miscele.

1

Introduction

1

1.1. General Statement

This dissertation starts with an important Einstein's thought "*Look deep into nature, and then you will understand everything better*".

Have you ever asked yourself what is happening? Have you ever notice that something has changed?

Answering these questions is important to understand what we are doing to and for the environment where we live. Nowadays, if we look outside we can see cities that are quickly growing and becoming a cluster of people, buildings and infrastructures. The direct consequence of this phenomenon is the increase of both pollution level and CO_2 emissions due to the necessity to improve the production of food, energy and whatever we need. This condition has been leading to increase the temperature of our Planet, our *home*. It could seem strange to talk about these topics at the beginning of a Ph.D. dissertation in asphalt pavement engineering, but it will be much more clear in the following paragraphs.

In the last few years, countless problems are spreading all around the globe due to temperature rise and increased variability of climatic conditions. Natural disasters such as storms, forest fires , flooding are becoming more and more frequent.

Basically, the direct consequences of these phenomena are both social and economical problems. In 2014, Laframboise and Acevedo [14] has summoned up interesting data, the most vulnerable countries are the major victims of the natural disasters.

From the economical point of view, it means the developing economies have much more difficulties for rising up after natural disasters. Nevertheless, the dollar value of disaster damage is much larger in advanced economies because of the amount and concentration of capital. This plight also threatens the road infrastructure building, maintenance, and rehabilitation investments.

In 2017, several studies have highlighted the weak efficiency of the material selection for road and pavement building [15]. The applications, which involve these kinds of materials, may result in rapid failure. The prediction of how climate change impacts the transportation infrastructures is therefore important [16].

Currently, the solution suggested by the scientific community is the possibility to improve the resilient properties of the road infrastructures. The *resilience* is the ability of a system to recover to its original state following a disruption. By going on this solution, it will be possible to dip the costs of the road infrastructure system. Therefore the long-term reliability and functioning of transportation system have to be adapted to the now extreme weather condition and events [17].

As people are struggling to achieve the highest resilient level, raw materials for road activities are hard to find. The situation heretofore has been exacerbated by the mistreatment of both soil and subsoil. This condition will be leading the extraction activities to stopping soon.

The linkage among resilient infrastructures, cost optimization, and the solution to

the scarceness of raw materials is the *sustainability*.

Nowadays, this old concept has been reviewed, and it has been defined as the best mix between people, environment and profits.

The United Nations (UN) has proposed seventeen sustainable development goals which are shown in Figure 1.1[1] (2030 deadline).

Since 2015, the Europe Union (EU) [18] thought to start answering to the following questions, how can I close the loop of manufactured-products? How can I reduce gas-emissions and waste-productions? The European Commission has approved several provisions for answering to the proposed-questions [18–20]. It has been trying to boost a carbon-neutral, resource-efficient and competitive economy.

This economic program is called Circular Economy Action Plan [18]. Such, with this strategy, EU has evaluated the opportunity to transform its economy and generate new and sustainable competitive advantages for Europe. *Transition* was the keyword of this action plan, and its objective is the linear economy which is based on three main steps, extraction of raw material, design and waste production.

Figure 1.2[2] shows, on a schematic-way, how is possible passing from a linear to a closed-loop circular economy. The waste-arrows in Figure 1.2 establish to send back to the previous step the obtained refuses.

In 2018, a monitoring framework [19] was published. The results remarked the improvements due to the closed-loop circular economy.

[1] United Nation web-page: Sustainable Development Goals.
[2] EIT Raw Materials-Spring School on Circular Economy.

Figure 1.1 Global sustainable development goals. Adopted from [1]

Figure 1.2 Passing from linear to circular economy. Adopted from [2]

The recycling rates of different wastes were improved with an average of 54,5%. The resonant-effects of this positive-sign influenced jobs, growth and investment in circular economy sectors. Consequently, 3.9 million job positions were generated.

On the financial point of view, the economic-growth improved of 6.1% compared to 2012. This means € 141 billion of value added. It is mandatory to remark, this economic data were effected by the economic-crisis which spread around the state-members. If the crisis had not disseminated, these indices would have probably been higher. Nevertheless, the private investments has achieve € 15 billion. Constructively, due to these scored-EU-goals, in 2019, EU published an important Staff Working Document (SWD) which proposed to improve the actions for developing the European-circular economy as better as possible [20].

The EU thinks synergetic actions could increase the sustainability in production by using both recycling and reusing practices. By walking on that way, waste-materials receive a chance for becoming innovative-materials into the industries' production-loop. This scenario has helped new sources become available in the asphalt pavement industry. Bio-binders and all the so-called green materials represent a new frontier.

Green material applications represents a huge leap for the asphalt pavement market and stakeholders. The European Asphalt Pavement Association (EAPA) has showed that

the production of asphalt pavement materials and their applications have not completely recovered after the 2008-financial crisis, which have characterised by the average increase of 1.4% per year [3]. Nevertheless, the European Asphalt Industry is represented by four-thousands of plants producing about 300-million tonnes of asphalt pavement materials per year.

In the last few years, the best sustainable material for the pavement application has been the so-called Reclaimed Asphalt Pavement (RAP). In 2018, the total amount of available RAP in USA was higher than in Europe, 91.70 and 51.80 million tonnes, respectively. These data are not negative because (by considering both hot and warm recycling procedures) the re-used percentage of RAP are higher for both USA and Europe, 90.5% and 76%, respectively [3].

Other sustainable actions has taken start for materials coming from the end of the supply chain such as steel slags, coal ashes, municipal waste ashes, residual of plastic, etc.. Currently, these materials are studied by the scientific community. The use of these new materials can lead to improving the pavement market.

Nevertheless, the production chain of asphalt pavements needs high level of energy consumption increasing CO_2 emissions.

An important report edited by both the EAPA and the Eurobitumen Association[4] shows that the carbon footprint of asphalt road is decreasing (it is about 35% lower than the past years). This is due to the use of reduced-temperature asphalt materials, which offer the possibility to use low temperatures during the manufacturing operation.

The questionable point linked to these applications is how they affect the performance level of asphalt pavements. By referring to the long-lasting period the situation is not completely clarified. [21]. Underwood [21] showed that the use of a multi-scale approach can help to improve the service life of the pavements. This approach is able to predict the performance level of asphalt pavements, but it needs to be implemented by mechanical tests for the Hot Mix Asphalt (HMA).

Due to the difficult interpretation of results, which are affected by the chemical interaction occurring between asphalt binders and fillers, the IC and mastics are not completely characterised.

The concerns of the study herein aim at developing a visco-elastic interpretative law of mastic behaviour in terms of energy dissipation (fracture energy and dissipated creep strain energy). The proposed objective is achieved using a multi-scale approach. For that reason, the following paragraphs analyse the state of art of the experimental approaches for mastic behaviour.

[3] EAPA web-page: Asphalt in figure 2018.
[4] EAPA and Eurobitumen: Fit for tomorrow: Asphalt paving safe, comfortable, sustainable

1.2. Experimental approaches for mastic behaviour

The main filler characteristics which have the greatest influence on mastics' properties are essentially: the shape, structure, size of the particles and their Specific Surface Area (SSA).

As highlighted above, the grain size of the filler plays an important role in terms of stiffening of mastics [22–24]. It was shown that the fine grain size reduces the viscosity and softening point of the mastic while increasing the penetration index, increasing mastics and HMAs susceptibility to both fatigue fracture and rutting. The density and fractional void of the filler, usually expressed in terms of Rigden Void (RV), are two other characteristics that affect the stiffening of the mastic.

Roberto et al. [25], Faheem and Bahia [26], and Faheem et al. [27] have shown how fillers with high RV are able to absorb more asphalt binder, increasing the friction between filler particles, but compromising the workability of the mixture.

SSA is the property of the filler that most affects the performance of the mastic [28, 29] by acting on the physical interaction between asphalt binder and mineral fillers. When the SSA of fillers is high, the cohesive strength of mastics is improved, preventing failure at higher temperatures such as rutting. Conversely, the properties of the asphalt binder mainly affect the damage accumulation rate and the creep-related performance of the mastic. It was observed that the creep behaviours slightly differ according to the type of filler employed, while it is significantly variable with the type of binder [30]. However, some particular types of fillers, especially those obtained from waste materials recycling, are able to affect the rate of permanent deformation due to their particular composition that chemically interacts with the asphalt binder, fully modifying its behaviour [25]. Despite the important role of mastics in determining the performance of HMAs, to date there are no standardised testing methods to assess mastic properties. Many efforts were made by several researchers to evaluate the response of the mastic to different loading in different test configurations and equipment, such as Dynamic Shear Rheometer (DSR) [31], Annular Shear Rheometer (ASR) [32–34], Dynamic Mechanical Analysis (DMA) [35–37] and Tension Compression Testing [12, 38, 39]. Experimental approaches were therefore attempted to define a fundamental interpretative model of mastic behaviour intrinsic to that particular binder-filler combination. It was possible to identify models that interpret specific behaviours, but the definition of an univocal interpretative model for mastics has not been set yet. In many models, the approach bases on Linear Elastic Fracture Mechanics (LEFM) and/or Elasto-Plastic Fracture Mechanics (EPFM). However, it must be considered that these approaches are not suitable for asphalt materials because their fracture behaviour is mostly influenced by their ductile and time-dependent characteristics. Therefore, it is essential to develop a model that takes into account the total energy dissipated during load applications.

To this purpose, a home-made gravity machine was developed to load a modified dog-bone shaped specimen (MDTT) according to [12] in load control mode, in order to

evaluate the response of the mastic in terms of rate of damage accumulation at intermediate temperatures (7°C). The strains were measured using a Digital Image Correlation (DIC) system already successfully used on asphalt mastic specimens in simple direct tensile configuration [12, 25, 40].

Several studies were performed to evaluate the performance of the mastic either by developing new test configurations or by modifying existing tests. These experimental researches mainly focused on identifying the response of mastics in terms of fatigue, rutting and fracture resistance.

1.2.1. Mastic's fatigue resistance

Kim and Little [41] used micromechanical and rheological methods to characterize the fatigue behaviour of mastics using the Dynamic Shear Rheometer (DSR) with an 8 mm circular plate and a 2 mm gap. By performing a dynamic torsional shear stress sweep test, it was possible to determine linear viscoelastic stress levels and to measure the linear viscoelastic complex shear modulus G* at 25°C and at different frequencies.

Faheem et al. [42] and Faheem and Bahia [43] also used the DSR performing fatigue tests on mastics under repeated shear cyclic loading at 28°C. The complex shear modulus (G*) and phase angle (δ) were measured as a function of the number of loading cycles, imposing a frequency of 10 Hz. Fatigue strength was estimated from the number of load cycles required to reduce the complex shear modulus (G*) of the sample by 50%.

Kim et al. [36, 37] and Kim and Little [41] developed a test equipment and methods to replace the DSR fatigue tests for mastics, entitled Dynamic Mechanical Analysis (DMA). The test specimen is cylindrical to simplify stress distribution and facilitate calculation. The DMA machine measures the resistant torque of the sample due to a displacement-controlled rotational input. The DMA analysis investigates the resistance of the mastic to fatigue damage, defined as the growth and propagation of microcracks under the action of torsional shear. DMA involves three tests. The first test determines the deformation range within which the sample shows linear viscoelastic behaviour and consists of a torsional shear strain sweep. Subsequently the specimen is subjected to a dynamic frequency sweep test that is performed at three temperatures and at different frequencies. The last one consists of a controlled shear strain cyclic fatigue test at 25°C and at high levels of strain causing fatigue damage.

Van Rompu et al. [32, 33], Delaporte et al. [44, 45], and Di Benedeto et al. [34] introduced a new test protocol called Anular Shear Rheometer (ASR) that allows to measure the complex shear modulus of mastics. The ASR applies a cyclic sinusoidal shear stress or sinusoidal deformation on a hollow cylinder of mastic (or asphalt binder), at different temperatures and frequencies. The dimensions of the sample (5 mm thickness, 95 mm internal diameter and 40 mm height) allow to consider homogeneous strains and stresses. Three transducers, positioned at a distance of 120° around the sample, measure the deformations during the test. When small deformations occur, it is assumed that the behaviour

is in the linear-elastic domain; in this case the modulus value, independent of strain amplitude, is called G*. When the applied deformation levels are high, the modulus is no longer in the linear domain, and is called the equivalent complex modulus (G_e^*). The test temperature is 10°C and the test frequency is 10 Hz. The innovation of the ASR is the measurement of the shear modulus during fatigue tests.

Miró et al. [46] developed a strain sweep test called EBADE test (in Spanish Ensayo de BArrido de DEformaciones) to study the fatigue behaviour of mastics at different temperatures. The EBADE consists of a cyclic tension-compression test with controlled strain during which several increasing strain amplitudes are applied every 5,000 cycles at a frequency of 10 Hz. The test is considered to be completed when the specimen is completely damaged. From this test it is possible to determine the maximum stress, the complex modulus and the energy dissipated density for each cycle.

Hospodka et al. [47] studied a new specimen shape for testing asphalt mastic fatigue using DSR. They replaced the traditional cylindrical specimen with a hyperboloid of one sheet. This shape allows to determine the point of failure and to prevent adhesive or interface problems between the mastic specimen and the top or bottom plate of the DSR.

1.2.2. Mastic's rutting resistance

Vacin et al. [48] tested mastic samples using DSR and characterized them by discrete relaxation and retardation spectra in small strain conditions. The test was performed in plate-plate and torsion bar configuration at high temperatures (up to 80°C). The shear compliance J(t) was calculated from the relaxation and retardation spectra while dynamic measurements were used for the linear visco-elastic characterization.

Faheem et al. [42] evaluated the contribution of filler to the rutting resistance of the mastic, conducing repeated creep and recovery testing in accordance with the procedure of the National Cooperative Highway Research Program (NCHRP) project 9-10 [49]. A shear stress in loading and unloading sequence of 100 Pa (1 sec. followed by 9 sec. rest period) was applied. The tests were performed at three different temperatures: 52° C, 58° C and 64° C. To assess the rutting resistance of the mastics, the accumulated permanent deformation at the end of the 100th cycle was examined. Later on, Faheem et al. [27] used the Multiple Stress Creep and Recovery (MSCR) test, in accordance with ASTM D7405 [50], to evaluate mastic rutting resistance. Tests were performed at three stress level, 0.1kPa, 3.2kPa, and 10kPa, and two temperatures, 58°C and 64°C. The indicators of rutting resistance were individuated as the non-recoverable creep compliance, (Jnr), and percent recovery at a stress level of 3.2 kPa and 58°C.

Also Cardone et al. [39] used MSCR according to ASTM D7405 [50] to evaluate the rutting behaviour of mastics. They performed 10 creep-recovery cycles on short-term aged mastics applying a creep loading time of 1 s and recovery time of 9 s. They tested at three stress level, 0.1, 3.2 and 10 kPa, as Faheem et al. [27] but at a wider range of temperatures (58°C, 64°C, 70°C and 76°C).

1.2.3. Mastic's fracture resistance

Williams [51] developed a test method to determine the fracture damage properties of asphalt mastic. However, this test allowed to monitor only the propagation of the crack tip represented by the variation of the asphalt fibril geometry by applying imaging techniques, but not measuring the strength of the mastic before its failure. Kim et al. [52] implemented the test introduced by Williams [51] to study mastic time-dependent fracture behaviour, focusing on instantaneous traction and strain within the fracture process zone. During the test, conducted at 24°C, two cameras were used to monitor the three-dimensional displacements, while the strength was registered by a load cell installed in the system. The test results were subsequently incorporated into the theoretical cohesive zone model to characterize the ductile non-linear viscoelastic damage behaviour.

Montepara et al. [12] developed a displacement-control direct tensile test based on the Standard SuperPaveTM Direct Tension Test (DTT) to evaluate the fracture behaviour of mastics. Strain development and fracture initiation were identified using a specific Digital Image Correlation System (DIC) developed by Birgisson et al. [13]. The improvements compared to the standard DTT involved the use of a servo-hydraulic load frame to achieve more travel and the optimization of the specimen geometry to assure uniform stress distribution within the specimen web and adequate gauge length to apply the DIC system. The test was performed at 10°C with a load application speed of 1.68 mm/sec.

Qiu et al. [53] developed a modified direct tension test with a loading–healing–reloading procedure to characterize the cracking and healing behaviour of bituminous mastic. A parabolic shaped specimen was used to guarantee that the stress concentration in the middle of the specimen was such that the cracking and healing occur at the same position. The test consisted in a direct tension displacement-controlled load application to obtain damaged specimens with different crack sizes at various post-peak elongations. The test was performed at 0°C with a displacement speed of 10 mm/min. Real crack sizes after unloading from each target elongation were analysed by a fluorescence microscope, examining the average width of a single crack perpendicular to the elongation direction.

1.3. Objective statement

The objective of this dissertation is the evaluation of the creep behaviour of HMAs at intermediate temperatures. In order to achieve the targeted point, a multi-scale approach was used. This was based on the analysis of creep behaviour of both mastics and HMAs. The first one was evaluated using a standard test (MSCR) and a new experimental procedure designed during this research activity, while the HMAs have been characterised through the Superpave specification. To accomplish the proposed aims the research program must be divided into three branches, which were conducted independently, as shown in Figure 1.3.

The first one is the characterization of the involved materials. This part of the study

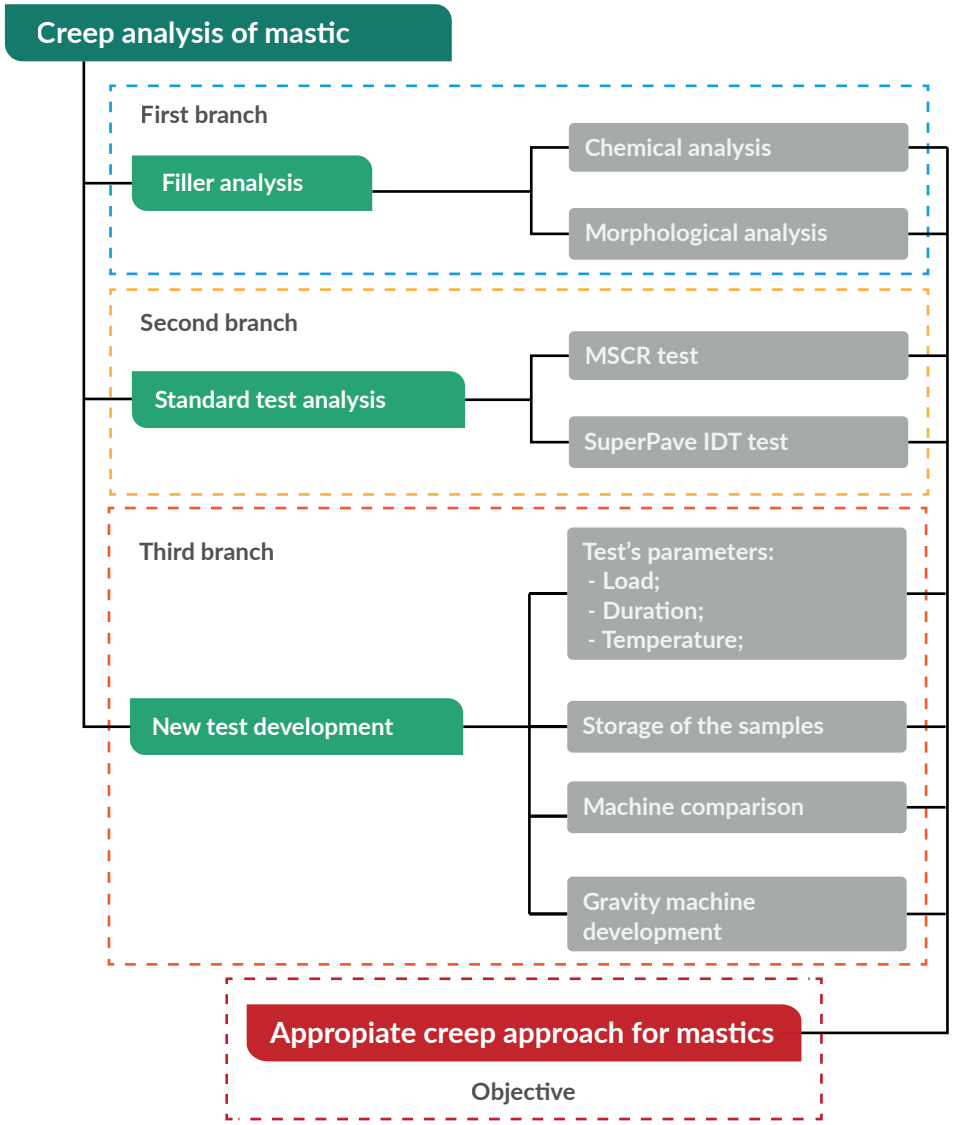

Figure 1.3 Schematic representation of overall research plan

aims to introduce innovative reused-materials. This branch want to open the possibility to better understand the role of the finest parts of this "waste" materials to allow going through a circular economy as fast as possible.

The second one is the study of both the HMAs and FAMs through standard tests. In this research the used standard tests are the SuperPave IDT and the MSCR test. This part wants to collect data to find out the probable correlation which may occurs among mastics, FAMs and HMAs.

The third branch is dedicated to the development of the new test method. The achievement of the final setup has involved several analysis such as the comparison between different testing machines, the recovery time into the climatic chamber, the duration of the test, the load to apply, etc..

The obtained outcomes will lead to define the creep relationship occurring between the HMAs' phases.

1.4. Scope

The definition of the creep connection was performed analysing both HMA and mastic behaviours. As mentioned above, the experimental procedures used are the Superpave protocol for the HMAs, while the MSCR and a new testing protocol were used to characterise mastics.

The used materials were basically two asphalt binders (SBS modified and Neat bitumens), five fillers, and limestone aggregates (12.5 mm maximum size). The involved filler materials can be split in two categories: conventional and alternative materials. The first one represents the material typically used for the road construction, maintenance, and rehabilitation. Those materials are one limestone filler and two limestone based fillers containing 20% of hydrated lime. While, the second category includes one reclaimed material (RAP), one type of WCO, which was used as rejuvenator, and one type of ladle steel slags (LFSs).

Focussing on the alternative fillers, two different RAP content (RAP%), 50% and 20% by the weight of the aggregates, were used. While, the LFSs were considered after a 48 hour hydration treatment and as received.

Considering both alternative and conventional materials, fourteen combination for each HMA analysed phase were obtained.

The prepared HMA samples were all tested at 10 °C performing the Superpave specification, which is based on the IDT configuration and composed by the three tests: the resilient modulus, the creep compliance, and the tensile strength tests. Therefore, both mechanical and cracking behaviour were analysed considering the HMA fracture mechanic framework [6, 7, 54].

On the other hand, mastics were prepared using a semi-mechanical mixing procedure which has been statistically validated during this research project. The obtained samples were tested using the DSR, by performing the MSCR test at 64 °C involving both the standard shear stresses, 100 Pa and 3200 Pa, respectively, and the new testing protocol properly designed during this research project. This experimental procedure imposes to test the samples at 7 °C applying a tensile static load (60 N) for 180 seconds. By using the MSCR both the Elastic Recovery (E_R) and the Non-recoverable Creep Compliance (J_{nr}) were computed. Those allowed to understand both the elastic capacity and the aptitude of cumulating deformation of mastics in shear condition. While, the new test method allows

to evaluate the Creep Compliance of materials (J_{MTCT}) and the m-value. Thus, both of them allow to evaluate how prone the material is to accumulate permanent deformation and how fast the mastic accumulate it.

1.5. Dissertation outline

This dissertation is divided into six chapters and two appendices. All the written-chapter are introduced by a literature review which is focussed on the topics covered. A brief summary of each chapter is given below:

Chapter 1 - ***Introduction*** focusses on the context of the dissertation and it also provides to introduce the objective and the scopes of the dissertation.

Chapter 2 - ***Towards sustainable pavements*** describes the used materials and their combinations. It is linked to the fist branch of the Figure 1.3. The chapter also explains how the pavement engineering is turning its wondering gaze on the possibility to reuse waste materials as much as possible. To better introduce this topic, several recycling and reusing practices for pavement engineering are described. The chapter is concluded by describing the methodology used for manufacturing the investigated samples for each phase of the HMA.

Chapter 3 - ***Standard experimental analysis*** provides to give the specification of the standard test used. It focusses on explain the protocol parameters analysed to established the properties of the HMA and mastic.

Chapter 4 - ***The new tensile creep test*** introduces the overall analysis performed to develop the new testing methods. The main topic has explained going through the procedure used for determining the testing load, duration and temperature. The testing configuration has involved several recovery time into climatic chamber from 1 to 12 hours. On this way it was possible to establish both how much time is needed for starting the test after preparing the sample and if the creep behaviour is affected by the storage period. Another important topic of this chapter is the development of a specific gravity machine for performing the test.

Chapter 5 - ***Interpretative model*** shows and explains the interpretative laws which occur between the different mastics and HMAs. Therefore, the results were divided by the typology of filler and discussed.

Chapter 6 - ***Conclusion*** summarizes the key conclusions from this research and presents recommendations for future studies.

2

Towards sustainable pavements

As described into the Chapter 1, several governments' action plans are trying to achieve the highest sustainable-level in different fields.

As Thierry et al. [55] suggested, an integrated supply chain model is required for improving the sustainable level of the production chain. This new approach has to allow products coming back to the users from the end-point by a recovery operation. This operation could be, for example, re-use, repair, re-manufacture or recycling.

Currently, by focussing on the road and pavement field, the evaluation of the best sustainable procedure is demanded to the so-called Life Cycle Assessment (LCA) analysis. The Federal Highway Administration (FHWA) has defined the LCA as *an emerging technology that works to quantify environmental impacts over the entire life cycle of the pavement system* [56].

Since 2015, the FHWA-sustainability concept [56] has led by an important hypothesis: sustainability is linked to economic, environmental, and social impacts, which are often collectively referred to as the *"triple-bottom line"*. Moreover, these sustainability-concepts are definitely *context sensitive*, thereby a combination of both cost-benefit analysis and LCA for designing good trade-offs has been aiming to calibrate the best sustainable result on the triple-bottom line.

Trade-offs are mandatory needed because, sometimes, sustainable solutions and/or materials are counterproductive for sustainability. For example, using a recycled-materials does not improve the infrastructure sustainable-level when long-transporting operations are needed. In fact, the economic impact and gas emissions of transporting negatively affect the society and environment.

In the last few decades, increasing of traffic level and climatic change are negatively affecting pavements' behaviour. For example, turnover between freezing and scorching temperatures, and traffic congestions can eventually lead to a quick failure of pavements.

Worldwide, several studies [57–62, e.g.] are struggling for investigating the effects of "waste" materials. These residuals could be employed in the common practice, just if their effects on pavements' performance are correctly defined and computed.

For example, Mohamed et al. [57] and Roberto et al. [60] studied the possibility of reusing plastic-wastes for obtaining modifying-additives for HMAs. Roberto et al. [60] mechanically investigated the PMA technique for on site HMA-manufacturing procedures. Walking trough this solution, it could be possible to reduce CO_2-emissions and energy consumption by cutting-off several transporting-operations linked to polymer-modified bitumens. Jimenez Del Barco-Carrion et al. [61] studied the possibility of combining RAP with Bio-binders for increasing green pavements and reducing the gas-emissions.

The study herein aims to understand how the dismissed material can provide the possibility to reduce the finite resource usage by re-using them into the road infrastructure construction, maintenance, and rehabilitation. Therefore, this dissertation wants to im-

prove the scientific knowledge about the material characterization. Thus, the LCA tool is not considered but, perhaps, further extension thereof will focus on the possibility of combining multiscale approach and LCA analysis to improve the selection of pavement and road materials.

Two sustainable materials, the ladle steel slags (LFS) and the RAP material, were characterised in the following paragraph. Both have been compared with three limestone materials which are commonly used in HMAs' manufacturing practices.

To better understand the advantages and disadvantages of the alternative materials this chapter has been opened with both LFS and RAP literature reviews, which explain a worldwide overview. After elucidating the state of art of LFS and RAP suitability and sustainability, the characteristics of the used materials has been described.

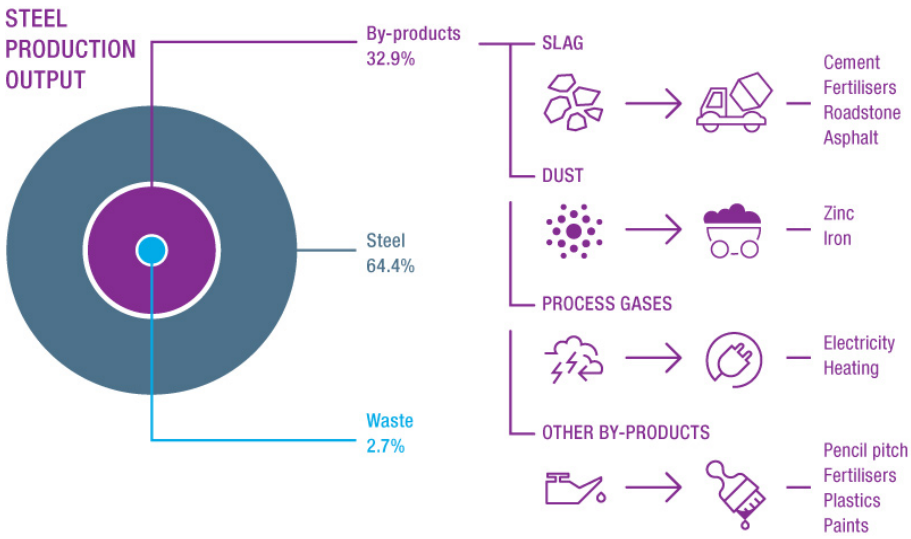

Figure 2.1 Steel production outputs and their reusing destinations. [3]

2.1. LFS: road-engineering material?

Nowadays the amount of steel and iron is increased up to 147 054 thousands tonnes [3][1], and its production outputs are characterised by 64.4% of steel, 32.9% of so-called "*by-products*" and 2.7% of wastes (Fig. 2.1). Basically, steel-making operations (Fig.2.2) is distinguished by the type of furnaces: Basic Oxygen Furnace (BOF); Eletrical Arc Furnace (EAF); Ladle Furnace (LF). The necessity to move towards the circular economy has shed light on the possibility of reusing steel making disposed by-products, which are not considered wastes since September 1995 [63].

Steel slags are part of by-products which are produced during the final stages of steel production adding quicklime to the heated-steel coming from the furnace, and the material is therefore subjected to desulfurization, degassing of oxygen, nitrogen, and hydrogen, removal of impurities, and final decarbonization. By focussing on the LFS only, their are obtained during the refining operation [64].

This kind of material is characterised by the presence of several chemical compounds, Table 2.1 shows their compound heterogeneity, their own gradation curve with a maximum size up to 1-2 mm [58, 65, 66], and high porosity (Rigden voids approximately 40% [58])and particle density level (from 2.8 g/cm^3 [65] to 3.2 g/cm^3 [58]).

Generally, the steel production is a batch process in which the chemical reactions are not ended [67], thereby LFS composition is characterised by silicates and aluminates of calcium and magnesium [64]. Their content is non-uniform [67] and both the free-

[1] Webpage of the World Steel Association (update April 2020).

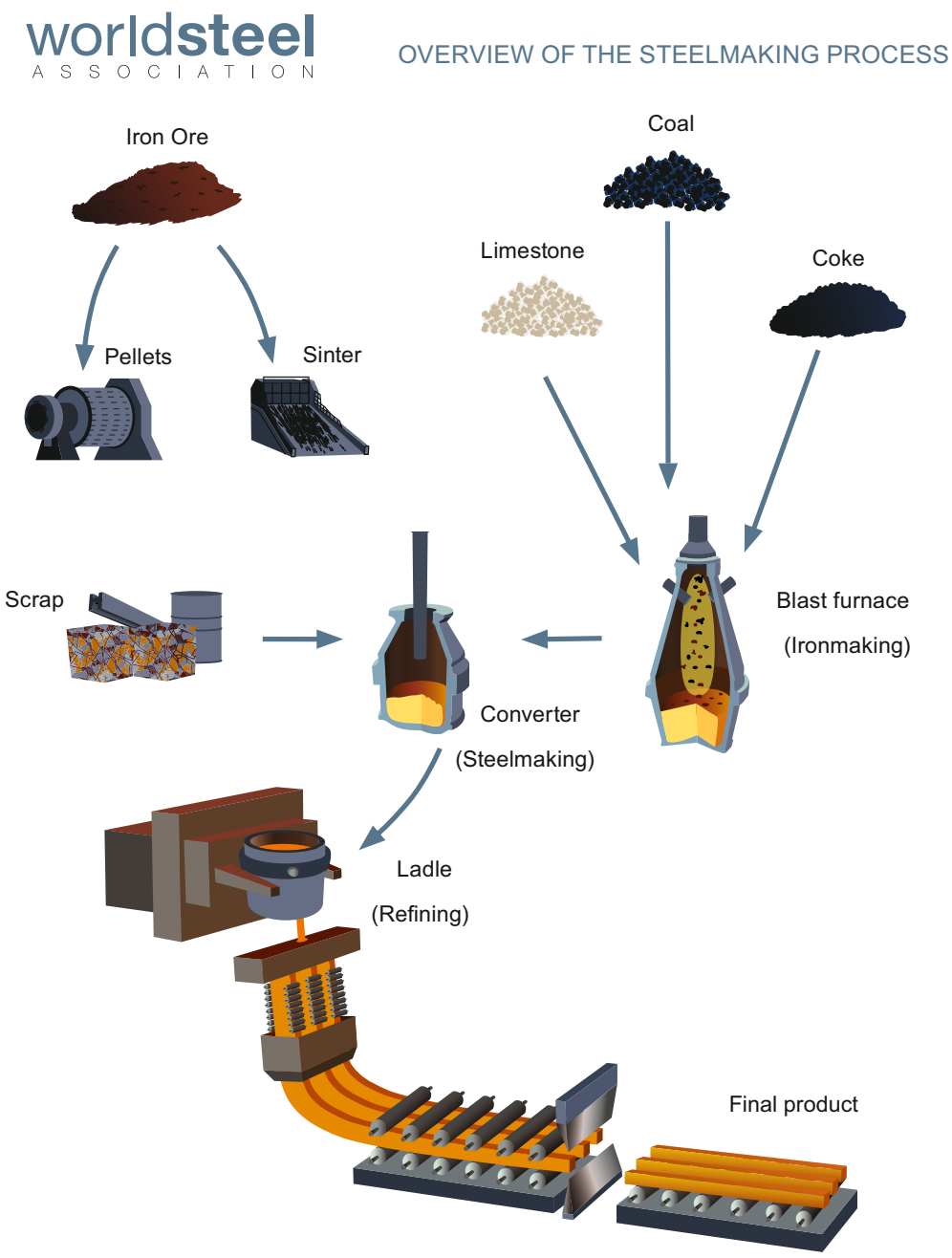

Figure 2.2 Steel making operations. Adopted from [3]

Table 2.1 Chemical composition from different authors by XRD analyses.

Compound	*Chemical composition* (%)			
	Bocci [58]	Setién et al. [68]	Kriskova et al. [71]	Shi and Hu [70]
CaO	48.77-50.36	50.50-57.50	51.50	57.00
SiO_2	20.21-21.64	12.60-19.80	28.30	26.80
MgO	13.06-16.42	7.50-11.90	11.30	3.20
Al_2O_3	8.92-9.36	4.30-18.60	1.20	5.20
TiO_2	1.82-2.04	—	—	0.30
FeO/Fe_2O_3	1.47-1.96 (FeO)	1.60-3.30 (Fe_2O_3)	—	1.59
S	1.37-1.63	—	—	—
MnO	0.32-0.37	0.40-0.50	—	1.00
Na_2O	0.07	—	—	—
Cr_2O_3	0.02-0.06	—	3.9	—
P_2O_5	0.03	0.00-0.01	—	—
K_2O	0.01	—	—	—

— means not detected or clarified.

calcium oxide (CaO) and magnesium oxide (MgO), among others, generally represent 50-60% of the total weight of LFSs [64, 67, 68] and their content is strictly furnace-type-dependent [69]. The material's composition is also distinguished by a CaO/SiO_2 equal to 2 [70]. This chemical composition characterises the material with hydraulic capacity.

In the last few years, the use of LFS is spread in different fields such as road application [58, 63], soil stabilization [64], earthwork and armourstones for hydraulic structures [63]. Motz and Geiseler [63], referring to all of the steel slag types, declared that the suitability of steel slags has to be proven by determining the technical properties, as well as the environmental compatibility.

By considering bituminous-based pavements, the LFS use is limited due to the following problems: volumetric instability and expansion connected to the miscellaneous chemical composition which is extremely H_2O and CO_2 reactive, hydration and carbonation phenomena, respectively; bitumen absorption linked to the high porosity of the material; less workability and compaction of the mixtures containing LFS; leaching problems.

The first one of this criticisms is probably the most important because of the duration of the mixtures containing LFS and it is common for all the types of steel slags. The hydration phenomenon starts from dumping operation of steel slags due to weathering conditions [72], and if it is not completed, hydration cans generate swelling problems for bound and unbound layers [63]. The most reactive components for these materials are the CaO and MgO, which react with water or environmental moisture as follow:

$$CaO + H_2O \longrightarrow Ca(OH)_2 \quad (2.1)$$

$$MgO + H_2O \longrightarrow Mg(OH)_2 \quad (2.2)$$

Ortega-López et al. [64] distinguished two different kinds of free-CaO morphologies, "*primary*" and "*secondary*" CaO, and one of free-MgO in the LFS composition. Both of the them are important in the liquid phase (at high temperature) to protect the refractory wall of the furnace.

The reaction 2.1 is exothermic and extremely quick. Comparing the CaO and $Ca(OH)_2$ densities, it is possible to notice that the first one is lower, meaning the chemical instability leads to volume increase (swelling up to 100%), and this effect is high for vapour-using procedures [73]. By considering this hydration-process, the majority of the free lime in steel slags will hydrate in a few days if water access is allowed [69]. Generally, the amount of hydrated free-CaO is the primary morphology, while the secondary hydrates slowly because of the confinement or enclosure of its particles [64].

The free-MgO is characterised by a slow hydration (reaction 2.2), and it can last for many years producing the increase of volume [69]. The presence of this compound is quite difficult to be estimated and cannot be evaluated by chemical analysis, thereby only the X-ray diffraction give a semi-quantitative estimation. Considering the long-term swelling, the free-MgO is able to produce volumetric expansion computable with a factor from 2 to 10 [64].

Among others, important consequences of these complex chemical reactions are also linked to the carbonation. This complex phenomenon allows to find $CaCO_3$ (calcite and vaterite) [68] and $MgCa(CO_3)_2$ (dolomite) [69] into the LFS dust without significant swelling problems.

Due to the complexity of the chemical interaction and reaction, it is not easy to establish *a priori* the volumetric expansion [64]. Several studies [58, 64, 68, 74, 75] were focussed on the evaluation of the hydration phenomenon and its consequences, but the use of LFS still needs caution [66]. Therefore, other studies were focussed on the possibility of limiting the CaO and MgO effects through the modification of the cooling system of the liquid slag [72] or by creating a protective bituminous coverage of the LFS particles [66]. Choi et al. [72] evaluated the possibility of avoiding the presence of both free-CaO and -MgO, modifying the production chain of steel-making-plants.

The other criticism linked to the chemical composition of the LFS, generally for all the steel slag, is the leaching phenomenon. Several studies [63, 76] remarked that the use of the steel slag was not linked to the environmentally relevant elements in the solid material, but it was linked to the potential elements that could be leached out. It is well known that CaO and MgO can increase the pH of the effluent solutions [77] due to their alkaline potential [78]. Bocci [58] highlighted the possibility of reducing the leaching of certain elements (in particular Al) by limiting the LFS content (up to 6.5% by mix weight) into HMAs.

Bitumen absorption and less workability are mainly linked to the high porosity of the material and the bitumen-LFS interaction. Several studies [58, 66, 76, 79] investigated these specific effects. Skaf et al. [66] demonstrated the good LFSs' adhesion with bitumen,

highlighting the quality of the formed mastic. Nevertheless, the interaction between LFS and bitumen increases the viscosity and stiffness of mastics, reducing the workability of HMAs [59], and leading to high air-void content of final mixtures [58]. The void content is also linked to the porosity of steel slags.

More recently, Pasetto et al. [65] have conducted an investigation on the effects of the LFS on the viscoelastic behaviour of both mastics and FAMs. This study has confirmed the increase of both viscosity and stiffness of mastics. These effects highlight also the increase of rutting performance when the LFS are included as filler into the mixtures. The porous structure of steel slags seems increasing the shearing resistance by absorbing the extensive oil which cause the permanent deformation at high temperatures [79]. Generally, HMAs containing steel slags show improvements in the indirect tensile strength (ITS), resilient modulus, rutting resistance, fatigue life, creep modulus, and stripping resistance [76]. Nevertheless, the increase in tensile strength leads also to brittle phenomenon as remarked by Pasquini et al. [59].

The introduction of the LCA as parallel tool for the selection of the materials has given the opportunity to obtain important consideration about the impact of mixtures containing steel slag on the above defined *triple-bottom line*. The introduction of steel slags has led to important reduction in terms of LCA [80]. However, the mixtures containing steel slag are heavier and they negatively affect the transport cost and emissions, as well as the bitumen consumption due to their high absorption capacity [81]. However, Mladenovic et al. [82] carried out LCA for comparing the environmental impacts of the construction of asphalt wearing courses with the use of siliceous aggregates (the "*conventional scenario*"), and the use of alternative, steel slag aggregates (the "*alternative scenario*"). The results of this study showed a 20% reduction of impacts when similar transport distances are considered and compared for both natural aggregates and steel slag mixtures. This confirms the suitability and sustainability of LFSs and the other kinds of steel slags as road-engineering materials.

2.2. RAP practices: use of a complex potential material

Existing asphalt pavement materials are commonly removed during resurfacing, rehabilitation, or reconstruction operations. Once removed and processed, the pavement material becomes RAP, which contains valuable asphalt binder and aggregates. Gundla and Underwood [83], regarding the RAP micromechanical model, distinguished three main RAP phases: RAP clusters; virgin aggregates (generated during the milling operation); and aged binder which can be either contained into the RAP aggregates or being in a solid free phase.

With increased demand and limited aggregate and binder supply, HMA producers have begun using RAP as a valuable component in HMA [84]. RAP is a useful alternative to virgin materials because it reduces the use of virgin aggregates and the amount of vir-

gin asphalt binder required in the production of HMAs. The use of RAP also conserves energy, lowers transportation costs required to obtain quality virgin aggregates, and preserves resources [56]. Nevertheless, the worldwide governments have made huge efforts to promote the use of RAP but, in the common practice, the average RAP content in HMA usually does not exceed 20-30% of the total mix.

Nowadays, the best RAP industry is the Japanese one, which has achieved a similar national average in both colder northern and warmer southern regions which vary from 20 to 60% , as shown in Figure 2.3 in asphalt mixtures [4].

Looking at EU zone, the situation is still uncertain, in fact, the amount of RAP in asphalt layers is limited to 10-30% (Hungary, Sweden, Poland) or even prohibited in wearing courses (Czech Republic, Spain), while in others the RAP can be used up to 100% (Germany, Norway, Denmark) [85].

Different studies have been carried out whether increasing RAP percentages in HMA is feasible or not [86–88]. Maupin and Diefenderfer [88] reported the results of testing plant-produced mixes including 21–30% of RAP, showing that the addition of RAP slightly raised the high temperature resistance, but it decreased the performance at intermediate and low temperatures.

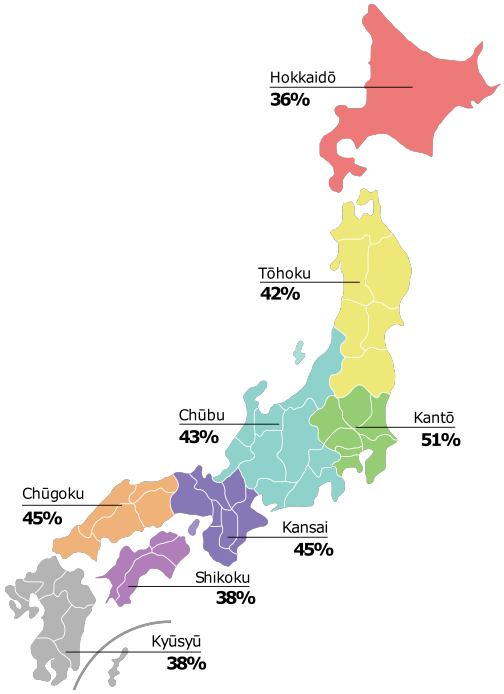

Figure 2.3 Japanese-map with regional average of RAP-reusing. [4]

Other studies have been focussed on an appropriate mix-design developed to achieve high RAP content in HMA [89–92]. On this regard, Zhou et al. [93] developed a balanced RAP mix design for high RAP content mixtures based on changing the binder content of the mix to optimize the maximum density. The conclusion of this study was that high RAP mixes can have better or similar performance to virgin mixes, but they must be well designed following appropriate mix design methods. Celauro et al. [91] conducted another investigation of mixtures with 50% RAP content concluding that, undertaking a tailored design with such a high percentage of RAP, good mixtures could be obtained. Results of the NCHRP Report 752 [94], as well as Sabouri et al. [86], showed that an increase in RAP content leads to an increase in permanent deformation resistance but also to an increase in stiffness, leading to cracking problems and consequently reduction

in fatigue life.

This problem is due to the presence of aged asphalt binder that during the mixing activity blends with the virgin asphalt binder and modifies its rheological characteristics. Currently, different approaches are being followed to develop proper mix design considering the blending between RAP and virgin materials.

In Europe the method is based on the physical properties (penetration and softening point) of both RAP and virgin binders (EN 13108-8:2005), whilst in the US the blending models take into consideration the initial rheological characteristics of the binders as described by the NCHRP Report 452 (2001). After building blending charts both specifications use the final RAP percentage in the mix to obtain the value that the property under assessment (i.e. penetration, softening point, etc.) would have after the manufacture of the mixture.

Jiménez Del Barco Carrión et al. [9], and consequently Lo Presti et al. [95] focused their attention on the evaluation of Degree of Blending (DoB) and tried to use it as mix design component. The methodology proposed was a combination of both European and US methodology. Nevertheless, RAP percentage is not the percentage of RAP binder that will be blended with the virgin binder, but depends on several factors (RAP binder content, virgin binder content in the final mixture and the degree of blending between virgin and aged binders). Pires et al. [96] emphasised the importance of having a detailed binder blend design as preliminary step.

Considering the criticisms above, to increase the RAP using, the RILEM-Technical Committees (RILEM TC264 RAP TG5, and RILEM TC237-SIB TG 6) have been trying to standardise practices for RAP characterization, studying the two-main characteristics of the reclaimed material, the gradation of the RAP source and the activation of the contained aged binder.

The need of analysing the gradation is due to the presence of the clusters. Recommendation of RILEM TC237-SIB [62] suggested to use appropriate RAP cluster- and activation-sensitive tests named fragmentation and cohesion tests, respectively.

The fragmentation test represents the cluster-sensitive test, which measures the resistance of RAP clusters and particles under several shocks induced by dropping a steel mass (Proctor hammer) [62]. Consequently, Preti et al. [97] studied the reliability of the RILEM-test, concluding that the fragmentation test can provide key information on the quality of the RAP materials.

The cohesion test is able to label RAP materials as "*active*" or "*inactive*", depending on the capacity of the residual bitumen to glue the particles together after compaction [62]. The results obtained have shown a link between the needle penetration of the aged binder undergone to extraction and the cohesion after compaction.

Even though the introduction of the mentioned tests, the degree of activity of the residual bitumen/aged bitumen has not been clarified yet. In the last few decades, several studies [83, 85, 98, 99] have given different definition of the activity of the aged bitumen,

generating confusion on defining the activation phenomenon and the parameters linked to it.

Considering the hot, warm and half-warm mixtures, the asphalt technologists typically consider two scenarios for the degree of activity: "*full availability*" and "*black rock*". The first one represents the 100% activation distinguished by the full melting of the residual bitumen, while the second one is the 0% activation which indicates no melting phenomenon occurs [85], disrupting the correct bitumen dosage of the mixtures.

As understandable, although RAP is widely used into the common pavement mixture practices, the way towards high RAP contents is still challenging the scientific community. However, the suitability of RAP as sustainable material has been confirmed.

Due to the necessity of increasing the activity of the aged RAP bitumen, to reduce the use of virgin asphalt binders, new active materials have been using, which are named rejuvenators. These materials are characterised by a low or very low viscosity, and their main tasks is softening the harden aged RAP bitumen.

In the last few years, several studies [100–110] have tried to understand the feasibility of high RAP content HMAs by using chemical- and bio-rejuvenators.

These studies found that producing high RAP HMAs is possible by using these type of additives, but more attention is required in terms of workability and level of compaction of the prepared mixtures.

Important observation were done on the possibility of reducing the mixing temperature [100–102] if the rejuvenators are well measured out. This operation can allow to reduce the CO_2 emissions.

Currently, the attention of the scientific community is moving on the possibility of using bio-materials [101, 107, 109, 110] as rejuvenators. The study herein has focussed on the evaluation of a Waste Cooking Oil (WCO) as rejuvenator.

The WCO material is one of the much more produced waste worldwide, especially in China (more than 26 million tons) and USA (13,65 million litres) [103]. This material is a very low viscosity fluid which can be able to guarantee good performance as high RAP HMA additive.

Ahmed and Hossain [107] highlighted the efficiency of WCO to increase the penetration of RTFOT aged bitumens. The author also highlighted substantial redaction in rotational viscosity at warm temperatures (especially at 120°C). However, the WCO dosage is still debated and its use has not tested in field yet.

2.3. Investigated-materials

The herein study is focussed on defining a multiscale approach to interpret the creep behaviour of HMAs by correlating a new-tensile creep test, properly designed for mastics, to both SuperPave IDT and MSCR tests (HMA standard tests). Therefore, mastic and HMA specimens were manufactured and tested.

Table 2.2 Asphalt binders characterization.

Materials	Test	Standard	Unit	min*	max*	PG*
SBS Modified	Pentration@25°C	UNI EN1426	0.1 mm	45	80	64-22
	Softening Point	UNI EN1427	°C	80	—	
Neat	Pentration@25°C	UNI EN1426	0.1 mm	50	70	58-22
	Softening Point	UNI EN1427	°C	70	—	

— means not detected or clarified.
* Referred to the data sheet given by the company.

The materials involved for this dissertation are limestone aggregates and filler, two different limestone-based fillers containing 20% $Ca(OH)_2$, one RAP, one LFS material, two virgin asphalt binders, and one WCO. Excluding the two asphalt binders, the involved materials can be distinguished into two categories: conventional and alternative materials.

Each one of these has been combined with two commercial asphalt binders, one SBS modified and one neat, respectively. The modified bitumen is characterised by 3.5% of SBS linear polymers. The characteristics of both the materials are summarised in Table 2.2.

The investigated mixtures were manufactured using limestone virgin aggregates, and their grading-curves were obtained following the SuperPave Protocol based on control points [111]. As reported in Figure 2.4, the nominal-maximum aggregates size is 12.5 mm. This gradation and aggregate type are commonly used at University of Parma for investigating both mechanical and cracking behaviours of HMAs [25, 60, 112, e.g.], thereby they were considered as reference mixtures for this research. Virgin aggregates were also used for the IC preparation, considering the aggregate grading curve up to 0.500 mm.

2.4. Characterization of the conventional fillers

In this dissertation the conventional materials are represented by the pure-limestone and two limestone-based fillers. The reasons of using this three limestone materials are mainly two: the first one is the necessity of obtaining data from materials typically used into common pavement practices; the other one is to understand whether the new creep test is susceptible to the so-called active fillers or not. To accomplish the objectives, the pure limestone filler selected is also contained into the other two fillers, which are distinguished by the presence of two different type of hydrated lime, as shown in Table 2.3. The grain size distribution is the same for all the used fillers (Table 2.3).

The particle density of fillers was evaluated by following the pyknometer method (EN 1097-7). The measurements are reported in Table 2.4. The particle density is defined as

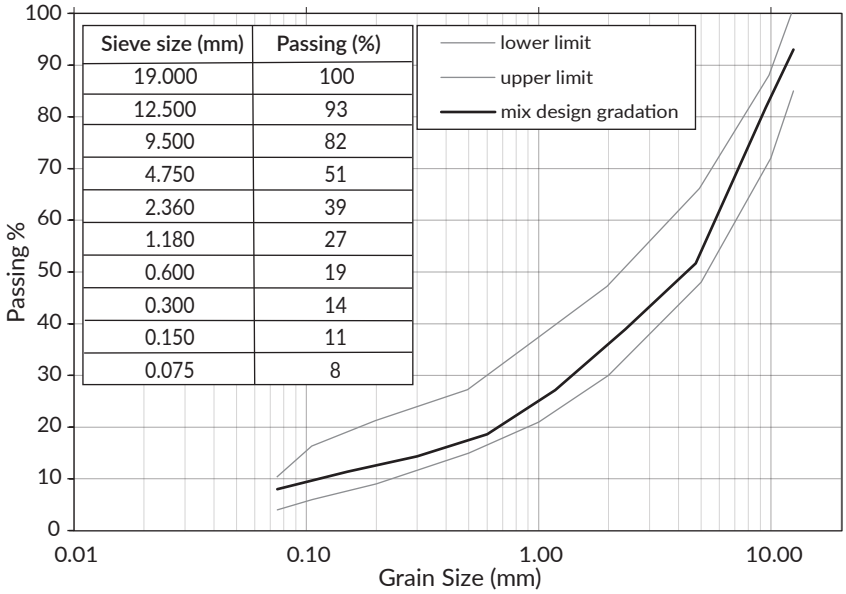

Figure 2.4 Virgin aggregates gradation curves.

Table 2.3 Labels of the three conventional fillers and their composition.

Filler label	Composition			
	$CaCO_3$ (%)	$Ca(OH)_2$ (%)	Hydrate lime type	Gradation (μm)
L	100	—	—	0 - 100
A	80	20	High surface area	0 - 100
F	80	20	Standard	0 - 100

— means not detected or clarified.

Table 2.4 Particle density of the conventional analysed fillers.

	L	A	F
Particle density (g/cm^3)	2.439	2.757	2.531

as the mass of a unit volume of fillers [113]. As noticeable, whilst the density for the filler containing the standard $Ca(OH)_2$ is quite similar to the limestone one, the A-filler density is higher the others. This is likely due to the high specific surface area (SSA) of the contained $Ca(OH)_2$.

The characterization of the described materials also involved a Scanning Electron Microscope (SEM) analysis. A SEM is a type of electron microscope which is able to produce images by scanning the material with a focussed beam of electrons. The interaction be-

tween electrons and atoms allows to obtain a detailed image of the grain topography and recognise their main chemical composition. The results obtained were reported in Figure 2.5, showing both the main chemical spectrum and the grain topography.

As shown in Figure 2.5, the shape of the grains is much more angular and elongated for the A-filler than the others. Moreover, their size is bigger than L and F. For that reason, the image scale for the A differs.

Before starting looking at the chemical spectrum, it is worth to indicate that the analysis of the chemical composition is a qualitative analysis. Therefore, the y and x axes are not reported. Figure 2.5 shows that the main components of the analysed fillers are Ca and O. The criticism of this approach is basically linked to the measurement nature. In fact, obtaining the C and H peaks in the materials spectrum is impossible. Due to that, the spectrum was used just to verify that other chemical compounds were not contained.

2.5. Alternative materials

The following section shows and explains the characterization of both the LFS and RAP.

2.5.1. LFS characterization

The problems highlighted by several studies in LFS are linked to their physio-chemical properties, which can cause volumetric instability [58, 69, e.g.], high bitumen absorption [66, 76, 79], and leaching phenomenon.

Considering the criticisms highlighted in the literature review reported, they can be divided in three groups: volumetric expansion due to hydration phenomena; bitumen adsorption linked to both the high porosity level and the fineness of the grains; leaching problems caused by the complex chemical composition of LFSs.

In this study the LFS's properties have been obtained for the material as received from the company and aged, as reported in Figure 2.6. The LFS ageing process is the hydration phenomenon which occurs either at the end of the manufacturing process or when the material is dumped [67].

To better understand the effects of the hydration process, two ageing procedures were performed, considering three different recovery periods (15 days, 7 days and 48 hours). While, the first one is the weathering condition, in which the material is left reacting with the ambient moisture, the second one was split into two hydration conditions: the first one considers the stoichiometric ratio suggested by Bocci [58] H_2O/CaO equal to 0.32; the second one was based on H_2O/CaO equal to 2 which allowed to obtain a full immersion condition of LFSs;

Referring at the material as received, it was stored for a short period (2 days) before starting both mastic and HMA specimens preparation

In this analysis, the characterization of the LFS was based on: X-ray fluorescence (XRF), X-Ray Diffraction (XRD) used for evaluating the chemical composition; the Scan-

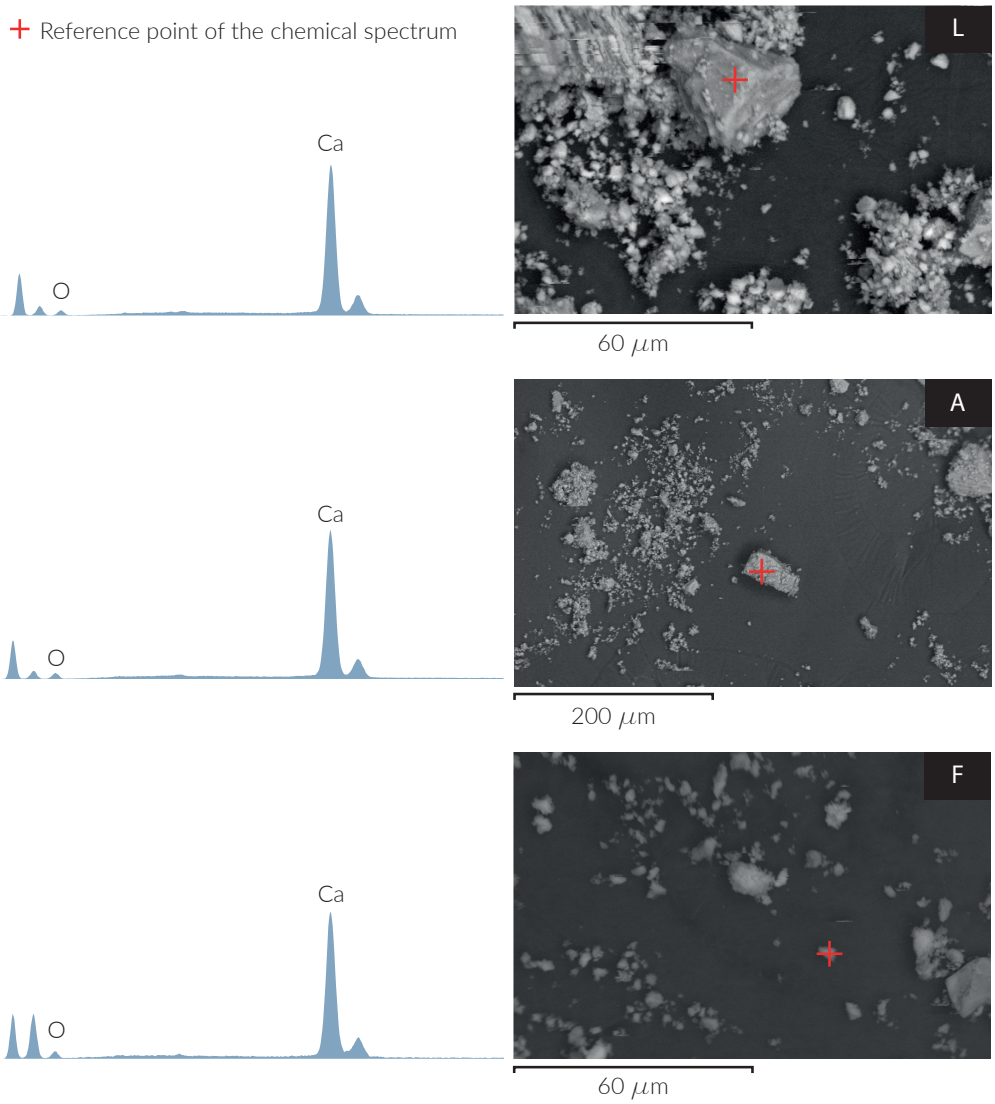

Figure 2.5 SEM analysis of both limestone and limestone-based materials.

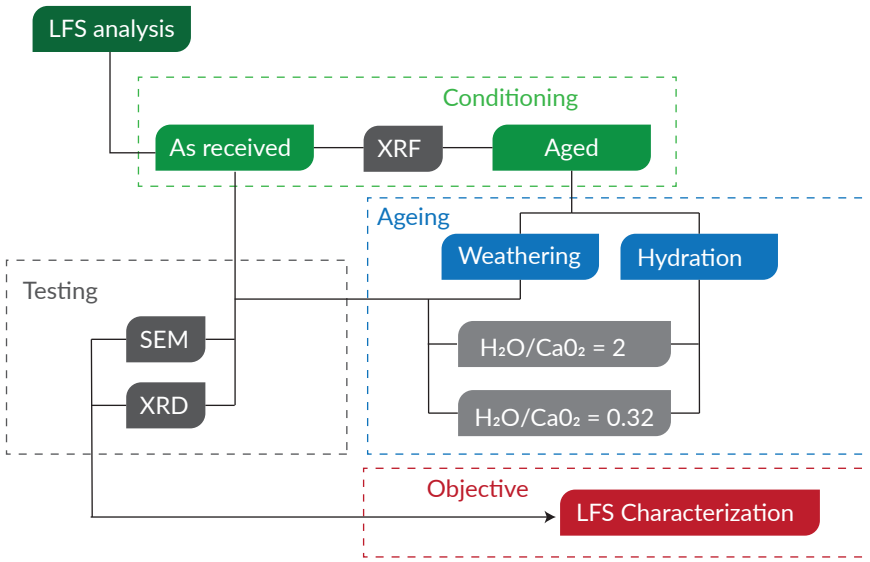

Figure 2.6 Schematic summary of the LFS characterization.

ning Electron Microscopes (SEM) employed for evaluating the LFS's morphology and the chemical composition maps.

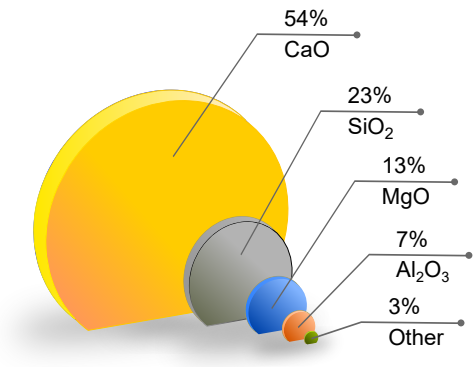

Figure 2.7 Analysed LFs chemical composition. XRF analysis based on bounds.

The XRF spectrometry is an effective quantitative technique typically used for the elemental composition of any material [114]. The XRF samples were prepared using about three grams of the dried and milled material. Before analysing the material, each sample was first pressed in a boric acid binder to obtain a thin layer pressed powder pellet (37 mm in diameter). Successively, a sequential wavelength dispersive XRF spectrometer (Axios-Panalytical), equipped with a 4 kW Rh tube and SuperQ 3.0 software, was used.

The X-ray Fluorescence (XRF) analysis was employed for highlighting the chemical composition of the as-received-material (hereafter mentioned as bulk material), which is reported in both Figure 2.7 and Table 2.5. The XRF results indicate the presence of the chemical element weighted on the oxide bounds. It is worth to specify that 54% of CaO, for example, indicates the presence of Ca and do not define the presence of the chemical compound CaO. Consequently, the

Table 2.5 Other chemical compound by XRF analysis.

Oxidation	P_2O_5	Cr_2O_3	K_2O	Na_2O	MnO	TiO_2	Fe_{tot}	FeO	S
Content (%)	0.01	0.01	0.02	0.02	0.48	0.49	0.66	0.85	1.00

SEM and XRD were required to identify the presence of the water sensitive compounds.

After obtaining the results of the XRF, the H_2O/CaO was calculated and the hydration procedures were started. Consequently, the prepared samples were subjected to both SEM and XRD analyses. These analyses were conducted for evaluating the best procedures (time and H_2O/CaO) for hydrating the LFS.

The XRD allowed to compute the presence of the water reactive components before and after the hydration periods considered. The XRD is a technique based on the diffraction of the atomic structure of the material analysed. It is typically used for the identification of crystalline materials as well as of fine-grained materials [114]. The XRD was performed with a Bruker D2 Phaser powder diffractometer with the following specifications: Cu K (λ = 1.54178 Å) radiation, 30 kV and 10 mA, Ni filtered, 2 between 5 and 70°, steps of 0.02°, and a sampling time of 1, s. The diffractometer acts with $\theta - \theta$ focalizing geometry and takes advantage of a solid state detector. A sample rotation of 30 rpm was applied to minimize crystal preferential orientation effects. The diffraction patterns were identified and semi-quantified using the Bruker software EVA and the Crystallography Open Database (COD). The XRD results are reported as function of the Bragg's angle (2θ) which represents the angle of the incident X-rays [114].

The analysis started evaluating the crystal structures of the bulk material and, consequently, the hydrated specimens, previously dried into a draft oven, were analyses.

Figure 2.8 shows the XRD results of the bulk material and also highlight the main XRD pattern of the CaO. As it is possible to notice, the bulk material does not contain CaO, in fact its XRD pattern does not show any peaks at CaO diffraction points. This means that the CaO has already reacted during the storage period. In fact, the presence of $Ca(OH)_2$, as shown in Figure 2.8 can be justified by the full reaction of the CaO. Oppositely, as expected, the MgO (Figure 2.8) was still active to react with water.

By observing Table 2.6, it is possible to observe the complexity of crystal structure of grains. Moreover, as expected by the XRF results, the majority of the crystal contains CaO.

After the characterization of the bulk material, the analysis of the hydrated specimens was performed. Figure 2.9 shows the comparison of XRD results for all the analysed samples. As it is noticeable, the diffraction patterns are similar between the bulk material and the weathered one. This confirms that the CaO has already reacted during the storage period. Probably, this phenomenon is due to the fineness of the CaO particles which require a quite short time of exposure to either moisture or water. Conversely, the MgO is still active after 15 days for all the considered hydrating periods.

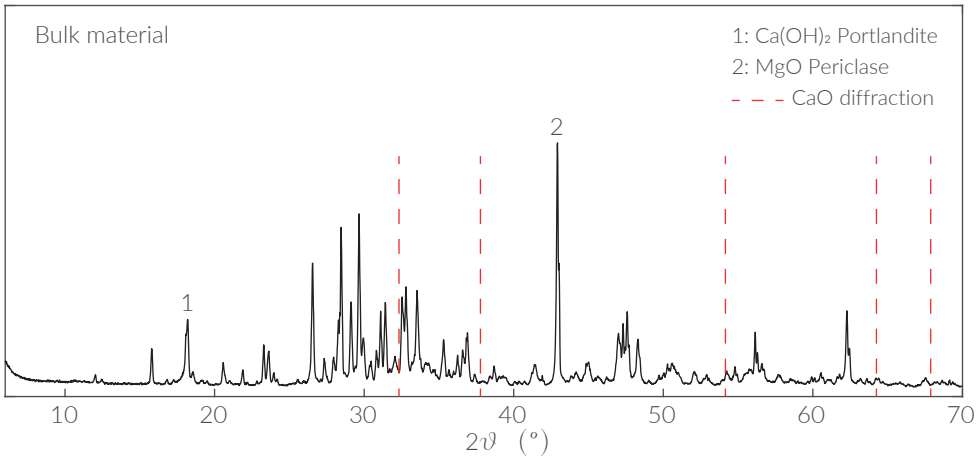

Figure 2.8 XRD analysis of bulk material.

Table 2.6 Crystal structures of the bulk material.

Name	Chemical formula	Mineral name
Calcium Silicate	$Ca_2(SiO_4)$	Olivine
Magnesium Oxide	MgO	Periclase
Calcium Magnesium Silicate	$Ca_5MgSi_3O_{12}$	—
Calcium Aluminum Oxide	$Ca_{12}Al_{14}O_{33}$	Mayenite
Calcium Aluminum Oxide Fluoride	$Ca_{12}Al_{14}O_{32}F_2$	—
Calcium Fluoride Silicate	$Ca_4Si_2O_7F_2$	Cuspidine
Calcium Silicate	Ca_2SiO_4	Larnite
Calcium Aluminum Silicate	$Ca_2(Al(AlSi)O_7)$	Gehlinite
Aluminum Hydroxide	$Al(OH)_3$	Nordstrandite
Calcium Hydroxide	$Ca(OH)_2$	Portlandite
Calcium Fluoride	CaF_2	Fluorite
Calcum Silicate	$CaSi_2O_5$	—

Figure 2.9 also shows that when the LFS hydrates there is a new diffraction, which is higher when the H_2O/CaO ratio is equal to 2. At that condition, the patterns are equal for the considered hydrating periods. For that reason, 48 hours and the full immersion condition were considered as the best hydration time and process, respectively.

Figure 2.10 highlights the difference which occurs between the bulk density and the material full immersed into a water bath for 48 hours. This change into the diffraction pattern is represented by a hydrated calcium aluminum silicate known as Zeolite ($CaAl_2Si_7O_{18} \cdot 6\,H_2O$).

The SEM as previously described allows to obtain the grain topography and the chem-

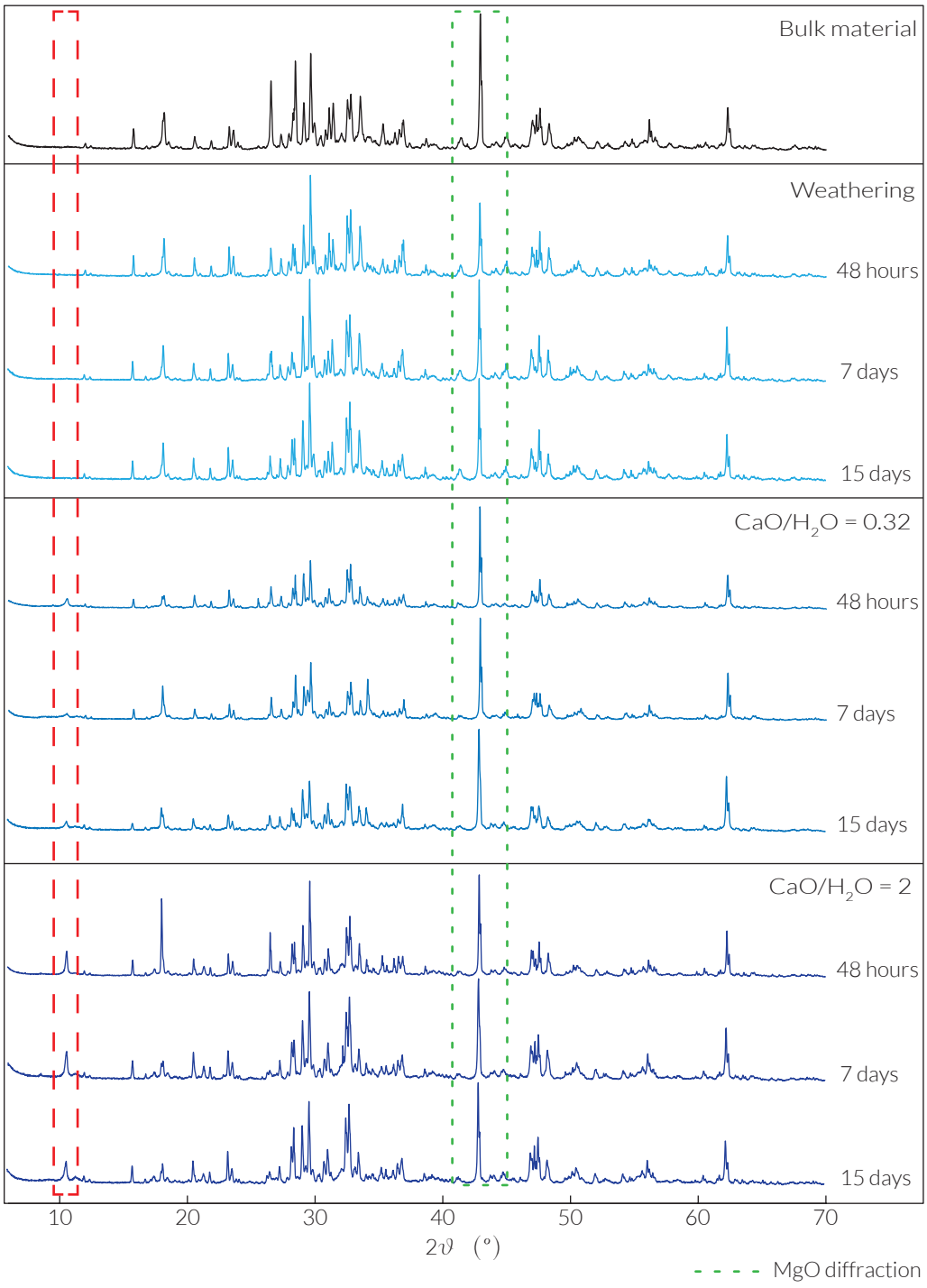

Figure 2.9 XRD analysis for evaluating the chemical structure at different hydration levels.

ical compounds distribution expressed as a map for each chemical element found.

The SEM specimen was observed by a scanning electron microscope coupled with an energy dispersive system (SEM-EDS) JSM IT300LV Jeol 6400 equipped with an Oxford EDS microprobe. Microprobe analysis was performed with the following operating conditions: 20 or 25 kV and 1.2 mA current, 1 μm beam diameter, and a counting time of 75 s. Analyses at 25 kV were performed in order to enhance the contribution of the higher energy peaks in metals and heavy metals.

The SEM results, shown in Figure 2.11 and Figure 2.12, remark the XRD results. In fact, the main chemical elements computed by the mapping function of the instrument confirm the crystal structures showed in Table 2.6. In the mentioned figures, the fineness of the material is also confirmed.

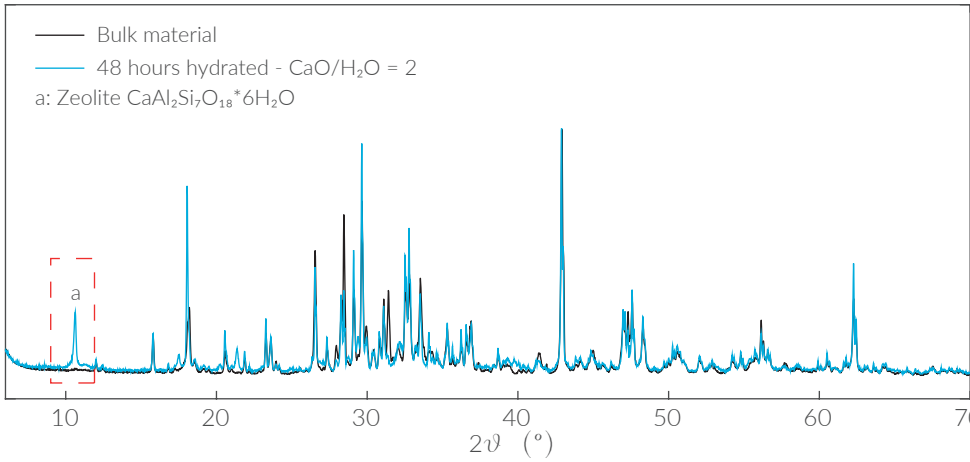

Figure 2.10 Difference between the bulk density and the material full immersed into a water bath for 48 hours.

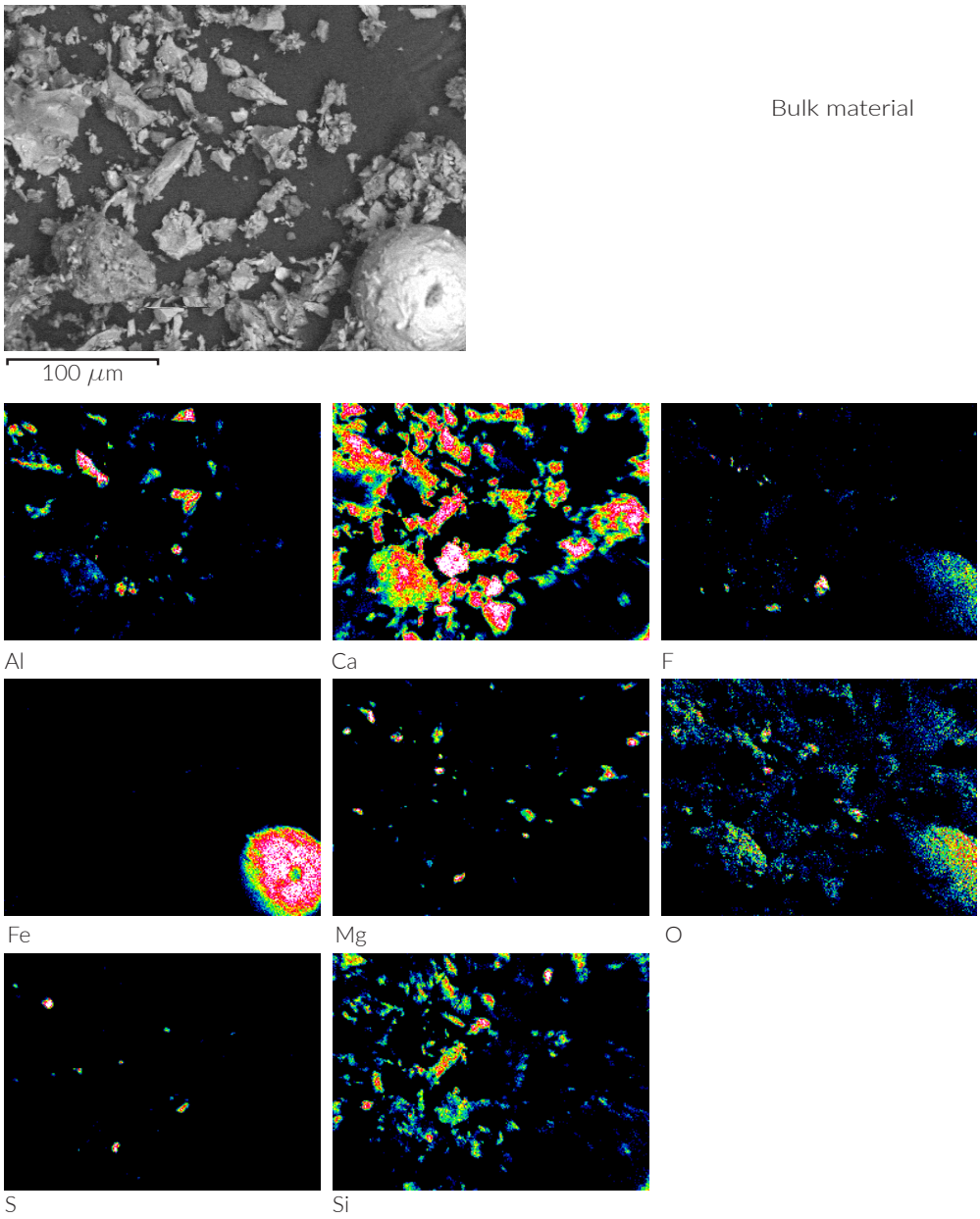

Figure 2.11 SEM analysis of the LFS bulk material with chemical composition map.

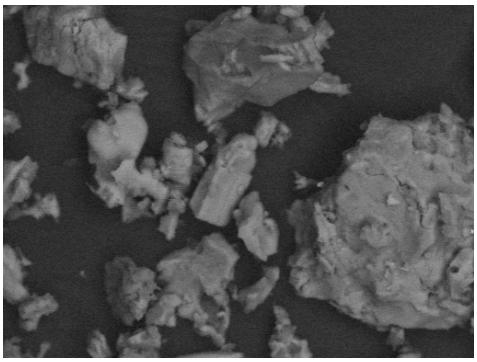

48 hours

$CaO/H_2O = 2$

60 μm

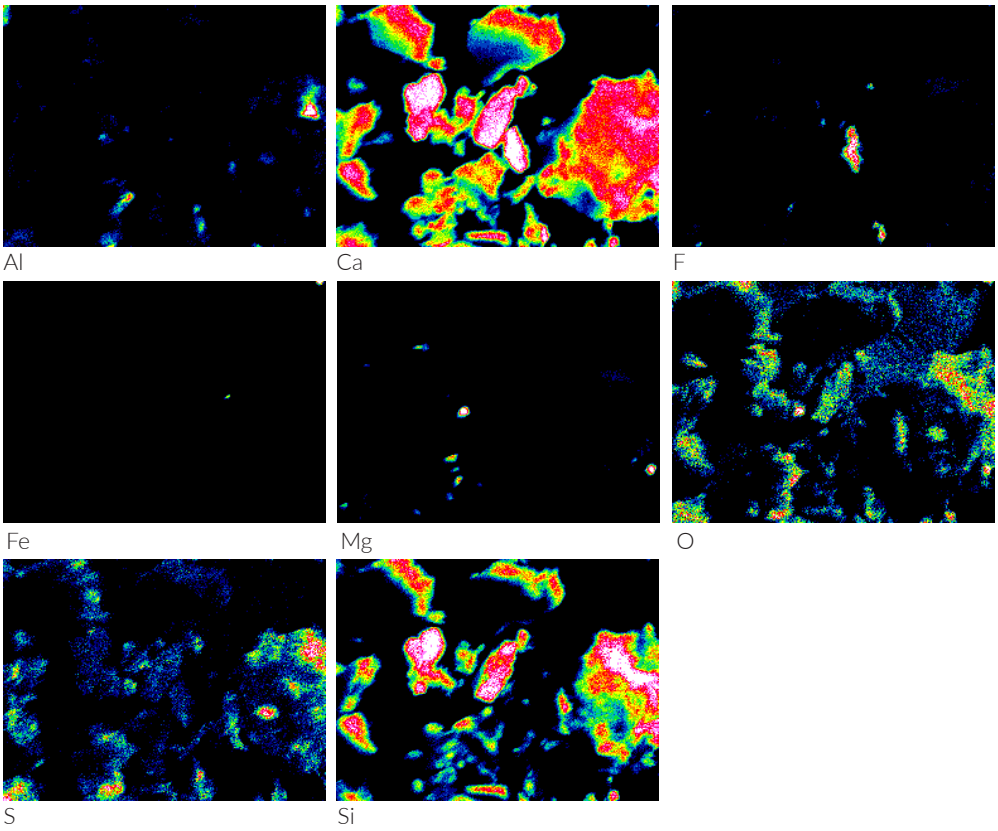

Figure 2.12 SEM analysis of the LFS hydrated for 48 hours with chemical composition map.

2.5.2. RAP materials characterization

RAP material usually comes from scarification and/or maintenance of old pavements. This material is obtained by milling operations. These practices are performed by using proper machines which can mill up to 40 cm layer-depth. The speed of this operation depends on the depth which the operators have to mill. The common practice for milling is to consider a maximum milled depth up to 20 cm. The higher is the milling-speed, the lower is the homogeneity of the RAP grading-curve. Preti et al. [97] have studied two innovative methods for characterizing the RAPs. These are both based on the 2018-RILEM note [62]. These studies aim at reducing the RAP-cluster presence into the grain distribution of available-RAPs.

In this case of study, one RAP (I-RAP) was firstly characterised and secondly investigated. The gradation curve of the material as received (named black curve) is shown in Figure 2.13a. The black curve represented has been obtained by sampling 20kg of the selected RAP, which is passing at the 16-mm sieve. In order to obtain significant results, the material was disposed on the floor, and quartered, obtaining 4 samples (about 5 kg each), which were successively sieved. The results shown in Figure 2.13a represent the average value of the 4 samples.

As noticeable in Figure 2.14, which shows the SEM analysis on the material, clusters are also into the lowest part of the grading curve. Moreover, the RAP is also characterised by the presence of dangerous substance as Cr (Chromium).

As mentioned above, the RAP problem is strictly linked to the contained-aged bitumen. In order to quantify the amount of this material, the analysed RAPs was subjected to extraction operations. Table 2.7 shows the details of the recovered aged bitumen, which are the average values of three repetitions.

Several studies [9, 92, 96, 98] has shown that when the RAP is preheated, there is a full or partial activation of the aged binder. For that reason in this study, the appropriate pre-heating temperature was selected by using the specification of the RILEM TG5 group.

As required by the RILEM TG5 DoA specification, which are not published yet but are well described by Lo Presti et al. [85], the RAP analysed was dried at 40°C for 48 hours. It worth to remark that the analysed RAP is stored into big bags and kept into a stockroom (Figure 2.13b). Therefore, the materials was not wet.

Before starting conditioning the RAP at the indicated temperatures (70, 100, 140, 170, and 190°C), the appropriate amount of materials for obtaining 50-blow-Marshall

Table 2.7 Aged binder characterization.

Materials	Aged binder total gradation (%)	Aged binder 0.5 mm gradation (%)	Pen grade @ 25°C (0.1 mm)
I-RAP	4.54	5.39	15.4

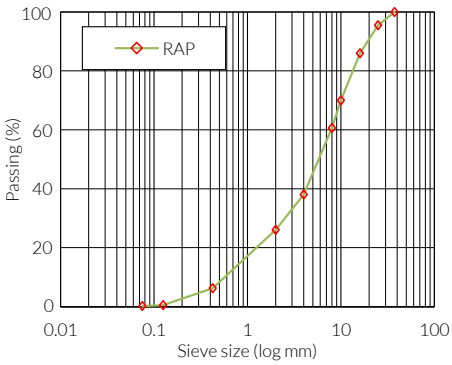

(a)

(b)

(c)

(d)

Figure 2.13 Black curve of the analysed RAP (***a***) and the recovered RAP (***b***) before drying and sieving operation. Marshall sample (***c***) and ITS testing configuration (***d***) for selecting the preheating temperature.

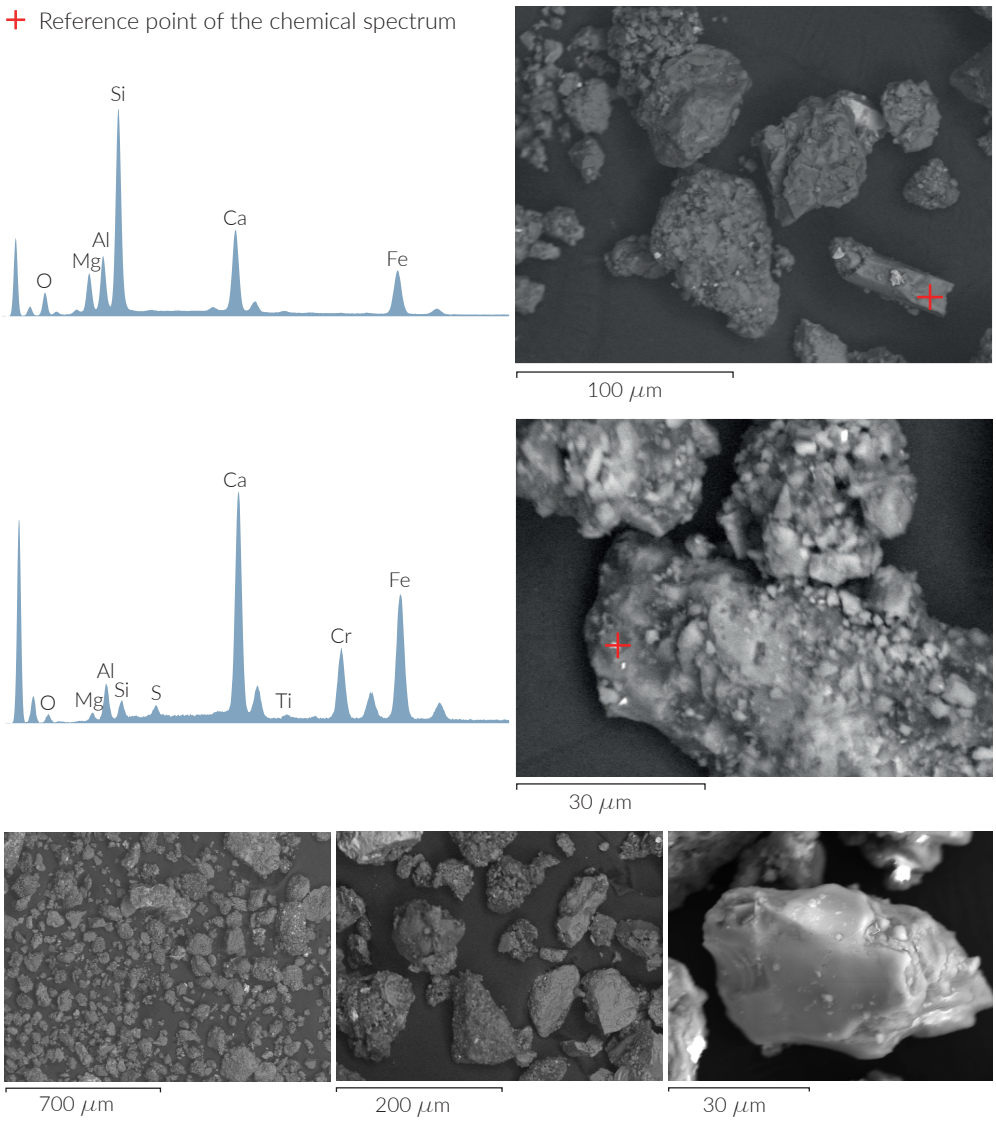

Figure 2.14 SEM analysis of the I-RAP.

Table 2.8 Height of the trial samples.

Sampled weight (g)	Sample 1 (mm)	Sample 2 (mm)	Sample 3 (mm)
1000	59.4	60.3	59.8
1200	68.8	67.5	68.6
1500	75.7	76.8	75.1

samples was defined by preparing trial samples distinguished by different weight (1000, 1200, and 1500 g). This operation was performed trying to reach the targeted Marshall-sample height (63.5 ± 1.27 mm). Thereby, 3 batches for each weight were filled with 1000, 1200, and 1500 g of RAP. Consequently, they were heated at 190°C for 4 hours, and, successively, compacted with the Marshall hammer considering 50 blows for each side of the sample. This temperature (190°C) was selected for preparing trials because it allows the maximum melting of the aged binder, which can lead to samples characterised by lower heights than the targeted one. The results of this analysis remarked to select a weight into the range 1000-1200 g, as reported in Table 2.8. In this case of study, 1100 g was selected as proper amount of material for obtaining the targeted height.

After determining the calibrated weight, 5 trays, for each indicated temperature, were prepared and heated for 4 hours. Consequently, the materials were firstly hand mixed, and successively compacted with Marshall hammer performing 50 blows for each sample's surface. After compacting, samples were allowed to cool down for at least 12 hours, and consequently extracted from the Marshall mould (Fig. 2.13c).

After the specimen preparation, the volumetric analyses was performed for calculating the specimen bulk density, the maximum density of the material, and the air voids contained into analysed samples. The maximum density ($\rho_{mv} = 2.450$ g/cm^3) of the analysed RAP was calculated by performing the EN 12697-5 (Procedure A: Volumetric procedure). In order to establish a statistical value of ρ_{mv}, three repetition of the procedures were performed. The bulk density (ρ_{bdry}) was obtained by following the EN 12697-6 (Procedure B: Saturated Surface Dry (SSD)). Consequently, the air void content for each specimen was calculated by using the following equation:

$$v_v\,(\%) = \frac{\rho_{mv} - \rho_{bdry}}{\rho_{mv}} \cdot 100 \tag{2.3}$$

where:

- ρ_{mv} = maximum density of the mixture, in g/cm^3
- ρ_{bdry} = bulk density, in g/cm^3;
- v_v = air void content.

Lo Presti et al. [85] requires the ITS testing procedure for evaluating the DoA of the material. The indirect tension test was conducted by performing the procedure as

indicated in the EN 12697-23. The ITS expressed in megaPascals (MPa) is calculated as follow:

$$ITS = \frac{2 \cdot P}{\pi \cdot D \cdot H} \quad , \qquad (MPa) \tag{2.4}$$

Where *ITS* is the tensile strength in MPa; *P* is the peak load, expressed in N; *D* is the diameter of the specimen, expressed in mm; *H* is the thickness of the specimen, expressed in mm. The testing set up was composed by a servo-hydraulic machine, and an appropriate designed device, as shown in Figure 2.13d.

Before testing, the samples were located into the machine climatic chamber, which was set at 25°C. All the specimens were allowed to cool at least for 12 hours. During the test, the applied load and displacement data were saved considering an 30 Hz-acquisition rate.

The average results of the RAP characterization in terms of pre-heating temperature was shown in Table 2.9. The analysed material exhibits quite the same bulk density, and consequently air void content, when it was pre-heated with T > 140 °C. However, in terms of ITS, 190 °C melted the aged binder but it also produced an ageing process. In fact, the ITS for the samples pre-heated at 190°C was lower than both 140° and 170° pre-heated materials.

$$DoA(\%) = 100 \cdot \frac{x_{RAP}(T, test)}{max(x_{RAP})} \tag{2.5}$$

Where x_{RAP} is the ITS results of the RAP at a specific temperature "T", and the $max(x_{RAP})$ is the maximum value observed among the temperatures evaluated.

Considering the approach suggested by the RILEM TG5 group, the DoA was also computed by using the Equation 2.5. As shown in Table 2.9, the maximum DoA was achieved at 170°C. For that reason, it was selected as pre-heating RAP temperature during the specimen preparation process for all the analysed HMA-phases. Much more specifications about the mix-design procedure of the materials containing RAP are given at the §3.3.2

Table 2.9 Results of the RILEM TG5 DoA procedure used for selecting the right pre-heating temperature.

Temperatures (°C)	Bulk density (g/cm^3)	Air voids (%)	ITS (MPa)	Height (mm)	Diameter (mm)	DoA (%)
70	2.099	14.3	0.184	67.9	101.5	16.4
100	2.150	12.2	0.487	68.9	101.7	43.4
140	2.220	9.4	1.057	64.4	101.3	94.2
170	2.213	9.7	1.122	63.9	101.6	100.0
190	2.213	9.7	0.792	64.4	101.3	70.6

3

Experimental methodologies

In the last decades, the introduction of the Superior Performing Asphalt Pavement (SuperPave™) method represents the huge leap for the characterization and analysis of the HMAs. This methodology was introduced by the Strategic Highway Research Program (SHRP) and allows to obtain a performance-based mix-design. Achieving this kind of material characterization has been possible combining both asphalt binder rheological properties and HMA behaviours by using proper mechanical tests (frequency and temperature sweep tests, BBR tests, tension compression tests, IDT tests). The SuperPave mix-design is based on considering the environment (climate), traffic and structural sections as means for achieving the required level of performance [111].

Following this protocol, the mechanical characterization was based on the Superpave IDT testing-configuration, which was defined by Roque et al. [115]. The measurement and analysis system is distinguished by three tests, resilient modulus, creep compliance and tensile strength. The starting point of this important testing procedure was 1992 when Roque and Buttlar [116] used the IDT as a suitable testing configuration for HMAs. The Roque's development [116] allows to find out the correlation that occurs between stress distribution, Poisson's ratio and asphalt concrete's modulus. Buttlar and Roque [5] better understood the efficiency of the creep compliance test and correlated it to the crack initiation during tests.

Successively, based on the tensile strength results [117] an energy analysis framework was developed [6, 7, 54], which was based on the Paris' law. This was called HMA fracture mechanics framework and it is valid into the viscoelastic range. Its principles are based on the introduction of an innovative concept: the energetic threshold. This innovation is based on the observations made by Zhang et al. [6] who split the crack concept, defining both the micro and the macro crack. Whilst, micro-crack allows the evaluation of effects due to the healing properties of materials, macro-crack describes the cracking initiation and propagation into the materials when micro-cracks coalesce each other.

The rheological characteristics of asphalt binders were based on the so-called Performance grade which was obtained through the evaluation of both $|G^*|$ and δ, AASHTO MP19, called complex modulus and phase angle, respectively.

In the last few decades, different studies [118–121] have started introducing a new test for evaluating the accumulation of permanent deformation in both asphalt binders and mastics. This test is the so-called Multiple Stress Creep Recovery (MSCR) test labelled as AASHTO TP 70. Important suggestions were introduced by Bukowski J. et al. [119], in which the authors highlighted important differences between the mentioned AASHTO standards, showing that the MSCR test accuracy is higher.

Therefore, considering the mentioned standard methodologies, for the study herein a SuperPave mechanical characterization and a MSCR analysis have been performed. Chapter 3 describes the scientific bases of the used-tests, and also the procedures performed for preparing the specimens for both the used standard tests.

3.1. Characterization of HMAs

In this study, the HMA characterization has been performed by using two different approaches, mechanical and energetic, both based on the same testing configuration, the standard SuperPave™ IDT performed at 10°C.

3.1.1. Standard SuperPave IDT

The importance of better understanding the visco-elastic response of asphalt-based consists in predicting the capability of the pavement to achieve the designed-end-life limit.

Inappropriate models are often used to determine the pavement system behaviour [116]. Generally the Poisson's ration and Young's modulus are used to perform those kinds of analysis, but they are able to describe just a particular response of the system [116]. Particularly, the Young's modulus is not measurable into the laboratory [116], but it needs a back calculation such as the FWD-data analysis [116], referring just to one temperature level, which is the on-site testing temperatures [116].

The IDT specimen stress propagation Figure 3.1b is as similar as to the wheel load application. Roque and Ruth [122] assessed the IDT moduli have an important capability to predict both strains and deflections measured on full scale pavements at low temperatures. Therefore, Roque and Buttlar [116] indicated the IDT configuration, shown in Fig.3.1a, as suitable for the HMA characterization. Considering the standard SuperPave IDT, the mechanical characterization is based on performing three different parameters as defined by Roque et al. [115]:

- resilient modulus (M_R);
- creep compliance ($D(t)$);
- tensile strength (S_t).

The Resilient Modulus is defined as the ratio of the applied stress to the recoverable strain under repeated load condition (Eq. 3.1). The Resilient Modulus test is performed in load control mode by applying a repeated haversine waveform load to the specimen for a 0.1 second followed by a rest period of 0.9 seconds. The load is selected to keep the horizontal strain in the linear viscoelastic range, in which horizontal strain is typically 150 to 350 micro-strain.

$$M_R = \frac{P \cdot GL}{\Delta H \cdot t \cdot D \cdot C_{CMPL}} \tag{3.1}$$

where:

- M_R is the Resilient Modulus;
- P Maximum load selected to keep the horizontal strain in the linear viscoelastic range;

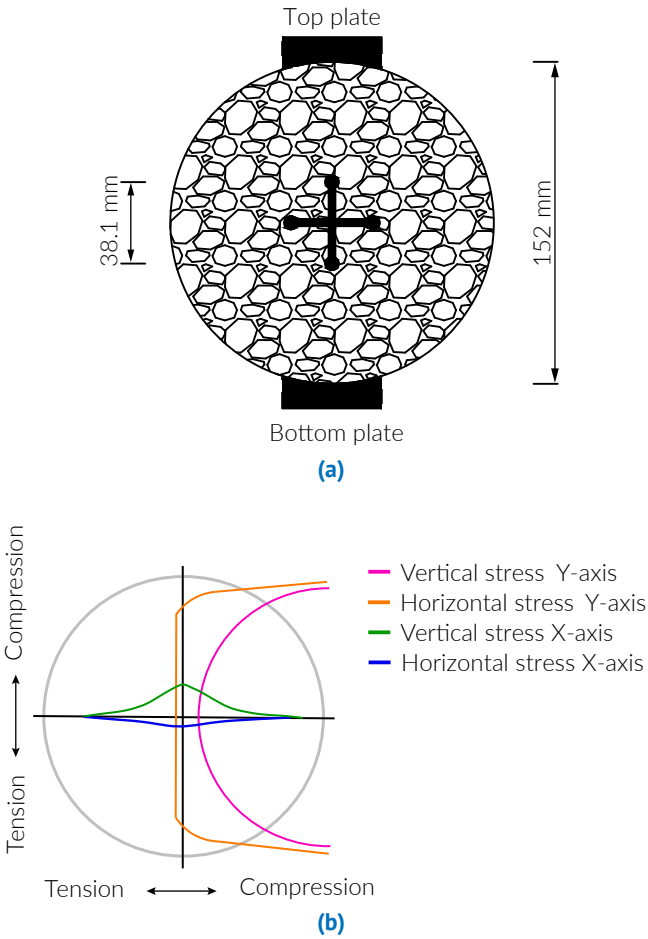

Figure 3.1 SuperPave *(a)* testing-configuration and *(b)* stress distribution.

- GL gauge length;
- D, t are the geometrical characteristics of the specimens, diameter and thickness, respectively;
- ΔH is the horizontal deformation;
- C_{CMPL} is the 3-D compliance factor.

The creep compliance test describes the time-dependent-behaviour of asphalt mixtures, which is typically used for evaluating the damage accumulation rate describing the phenomenon through the *creep compliance* at 1000 s and the *m-value* in the range 500 s to 1000 s.

Whilst, the creep compliance is a time dependant strain $\varepsilon(t)$ divided by the applied stress $\sigma(t)$, and considering the elaboration proposed by Roque et al. [115], it is computed by Equation 3.2, the m-value is the rate of the damage accumulation.

$$D(t) = \frac{H_m^{(t)} \cdot D \cdot t}{P} \cdot C_{CMPL} \tag{3.2}$$

where:

- $H_m^{(t)}$ measured horizontal deflection at time t;
- D, t are the geometrical characteristics of the specimens, diameter and thickness, respectively;
- P is the creep load;
- C_{CMPL} is the 3-D compliance factor.

The test is conducted in a load control mode by applying a static load selected to keep the horizontal strain in the linear viscoelastic range[1] [5], which is below an horizontal strain of 500 micro-strain. The load is then held for 1000 seconds. If the horizontal strains are not between 150 and 200 micro-strain at 30 seconds, the load is immediately removed from the specimen, and specimen is allowed to recover for a minimum 3 minutes before reloading at a different level.

As indicated above, the SuperPave parameters are 3-D factor dependent. This dependency is linked to the particular testing configuration [116]. Due to this, the stress is split into its own components, vertical and horizontal stresses, respectively, as shown in Figure 3.1b.

Buttlar and Roque [5] have widely discussed this phenomenon by analysing the fracture growth into HMAs. The authors have highlighted the correlation between the creep behaviour and Poisson's ratio. If the creep computation is obtained by considering Hook's law [5] and a biaxial stress state that exists on the specimen faces ($\sigma_z = 0$), it is possible calculating the creep by using the Equation 3.3.

$$D(t) = \frac{\varepsilon_x}{\sigma_x - \nu\sigma_y} \tag{3.3}$$

Where:

- ε_x is the horizontal strain;
- σ_x is the horizontal stress;

[1] Buttlar and Roque [5]: *"The analysis system presented...is valid only for specimens tested at temperatures and loading times at which the material exhibits linear elastic or linear viscoelastic behavior".*

- σ_y is the vertical stress;
- ν is the Poisson's ration.

Moreover, by introducing the 3-D correction factors [116] is possible computing the creep considering a proper non-dimensional creep compliance factor (C_{CMPL}) through the above-indicated Equation 3.2. The 3-D compliance factor is calculated through the following Equation 3.4:

$$C_{CMPL} = 0.6354 \cdot \left(\frac{X}{Y}\right)^{-1} - 0.323 \tag{3.4}$$

Where the X/Y is the absolute value of ratio of measured horizontal deflection (X) to measured vertical deflection (Y) [5].

Buttlar and Roque [5] carried out the linear correlation (Equation 3.4) which occurs between the compliance factor and $(X/Y)^{-1}$, and also defined the C_{CMPL} limitation which depends on (t/D). The mentioned relationship for being linear requires the following (t/D)-limitation (Equation 3.5):

$$0.20 \leq \left(\frac{t}{D}\right) \leq 0.65. \tag{3.5}$$

By following the mentioned considerations, the authors have determined the Poisson's ratio as function of both t/D and X/Y, as shown in Figure 3.2.

$$\nu = -0.10 + 1.480\left(\frac{X}{Y}\right)^2 - 0.778\left(\frac{t}{D}\right)^2\left(\frac{X}{Y}\right)^2 \tag{3.6}$$

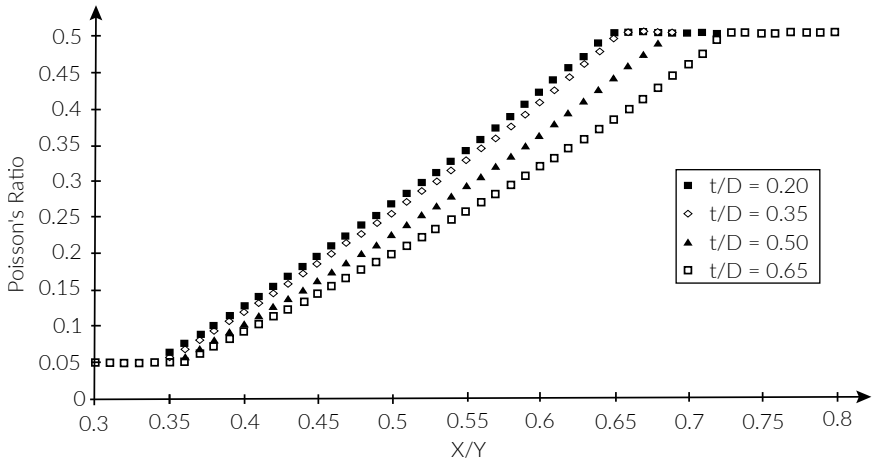

Figure 3.2 Buttlar and Roque [5]: Poisson's ratio versus X/Y and t/D.

Equation 3.6 is a fitting curve of data shown into Figure 3.2. It was obtained by using a linear regression and least squares estimators [5]. This methods is valid if Poisson's ratio respects the following constrain:

$$0.05 \leq \nu \leq 0.5. \tag{3.7}$$

The upper limit of 0.50 was selected to coincide with the upper bound of Poisson's ratio for elastic materials [5].

The tensile strength test is conducted in a displacement control mode by applying a constant rate displacement of 50mm/min until the specimen fails. The horizontal and vertical deformation, and the applied load are recorded at the rate of 30Hz during the test. The maximum tensile strength is calculated as the Equation 3.8:

$$S_t = \frac{2 \cdot P \cdot C_{sx}}{\pi \cdot t \cdot D} \tag{3.8}$$

where:

- S_t maximum indirect tensile strength at first fracture;
- D, t are the geometrical characteristics of the specimens, diameter and thickness, respectively;
- P failure load when the first fracture appears;
- $C_{sx} = 0.984 - 0.01114 \cdot \left(\frac{t}{D}\right) - 0.2693 \cdot \nu + 1.436 \cdot \nu$;
- ν is the Poisson's Ratio.

Referring at the S_t, the effects of the testing configuration are linked to the bulging of specimens [116]. Because of that C_{sx} is used for correcting the 2-D plane stress solution. Roque and Buttlar [116] highlighted by a finite element analysis that the correction of the 2-D plane stress is related to both the Poisson's Ratio and the thickness-diameter ratio.

3.1.2. HMA fracture mechanic framework

The further leap forward the performance characterization of HMAs has been done by Roque et al. [117]. This study tried introducing new fracture parameters for investigating the crack-growth-rate in SuperPave specimens. However, gyratory compaction and volumetric mix-design procedures were investigated for improving the SuperPave protocol. The proposed approaches suggested by the authors were basically two:

- an energy-based approach;
- a compliance-based approach.

Both the investigated approaches were based on the effective crack length concept which assumes that all damage is a crack growth result. The authors also highlighted the differences in mixture behaviour are also due to the effects of healing process and effects of damage in the form of micro-cracking during the crack initiation. The procedure developed [117] separates both the described effects. Due to this principles, both micro-cracking and crack growth are interpreted as damage.

Based on Roque et al. [117]'s approach, Zhang et al. [6] has introduced the new concept of energy threshold. This crack growth law has the following features:

- generalized loading conditions and healing can be considered;
- a threshold concept, was introduced, which results in discontinuous, step- wise crack growth;
- both crack initiation and crack propagation are addressed;
- the dissipated creep strain energy limit was identified as a threshold to crack initiation and propagation;
- it was found that the value of this threshold can be determined from simple creep compliance and strength tests using the Superpave Indirect Tensile Test (IDT) system.

The differences between Zhang et al. [6] and previous approaches is linked to base assumption, the previous one have based on Paris' law which is based on the linear-elastic fracture mechanics (LEFM). Therefore, Zhang et al. [6] has considered the viscoelastic behaviour of HMAs. Walking on this way, the author has introduced the possibility to take into consideration also the healing effects. Combining visco-elasticity and continuum damage approach, the authors have developed the crack-growth rate shown in Figure

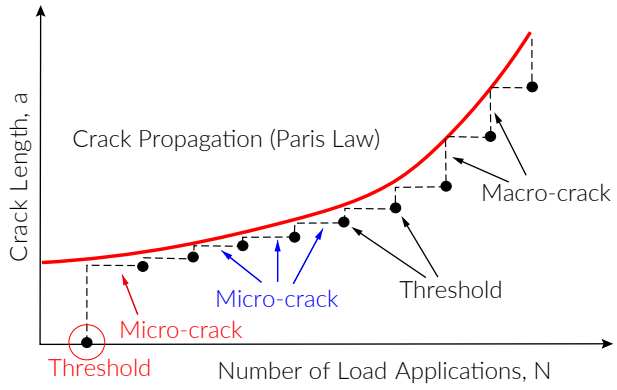

Figure 3.3 HMA fracture mechanics framework: fracture propagations.

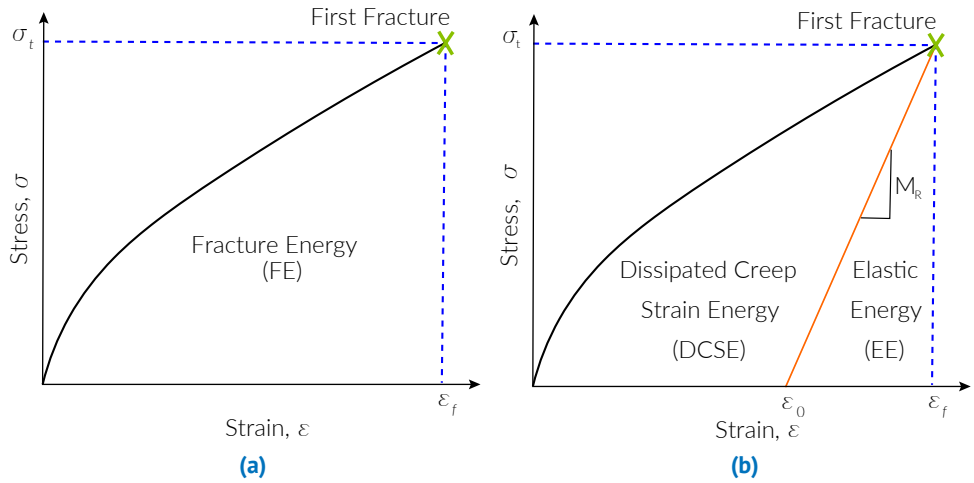

Figure 3.4 Stress and strain distribution *(a,b)* at first fracture [6].

3.3. This framework was based on the differences which occur between micro and macro cracks. Both the phenomena are governed by the energy threshold. The crack-growth law is called HMA fracture mechanics framework.

Zhang et al. [6] defined two energy thresholds:

- Facture energy (FE): it is defined as the area below the stress and strain curve (Figure 3.4a) at the first fracture calculate as suggested by Roque et al. [115]; Going through this computational framework it is possible calculating the EE and DCSE (Figure 3.4b), which describe the energy dissipate by to both the elastic response and the accumulation of permanent deformation of materials, as follow:

$$EE = \frac{1}{2}\sigma_f(\varepsilon_f - \varepsilon_0) \tag{3.9}$$

$$DCSE = FE - EE \tag{3.10}$$

Where:

$$\varepsilon_0 = \frac{M_R\varepsilon_f - \sigma_t}{M_R}$$

The FE describes the energy required for cracking the material with a single heavy load and it defines the upper threshold (Figure 3.5);

- Dissipated creep strain energy ($DCSE_{min}$): it is linked the creep compliance of materials. This threshold describe the minimum energy required for cracking the materials under repeated load condition and it represents the lower threshold (Figure 3.5).

Considering the introduced energy parameters, Roque et al. [7] discussed a no failure model and two different cracking models (Figure 3.5).

Figure 3.5a describes the no failure condition and shows the healing effects which are linked to the micro-crack. The meaning of this model is: the micro-crack is able to recovery if the lower threshold is not achieved.

Figure 3.5b represents the failure model linked to cracking due to the application of a single-heavy-load. This means the first crack appears when the energy level, due to the single-application of the heavy-load, is achieved.

Figure 3.5c highlights the achievement of the minimum energy which allow the micro-cracks to coalesce each other and the micro-cracks appear; The energy achievement is due to the application of repeated loads.

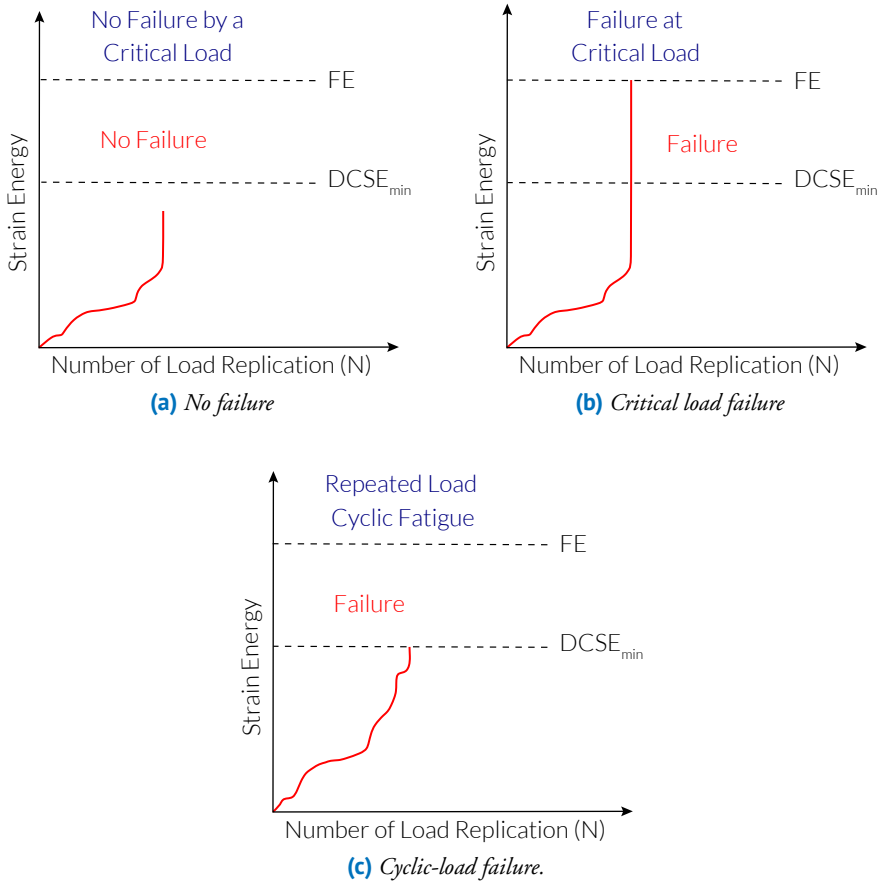

Figure 3.5 HMA fracture mechanic: fracture propagations and failure models [7].

3.2. Mastic characterization: MSCR test

The MSCR test was created for better evaluating the strain recovery aptitude of modified asphalt binders [123] and it is performed by using a dynamic shear rheometer (DSR) (AASHTO TP 70). Before the introduction of the MSCR test, the effects of polymer modifications of binders had not measured properly. Indeed, it was not possible obtaining into the laboratory proper parameters able to describe the effectiveness of polymer modifications. After the introduction of this testing method contractors as well as companies and departments of transportation were able to quantify this lacking-requirement [123].

Bukowski J. et al. [119] evaluated the accuracy of this test by comparing AASHTO MP19 and MSCR test. The results have confirmed the hypothesis made by Dubois et al. [123], the MSCR test is able to give us better data series.

The introduced testing-method is based on determining two parameters: the percentage of elastic recovery, R, and the non-recoverable creep compliance, J_{nr}. This parameters describe how much the materials are prone to accumulating permanent deformation.

Calculating both the MSCR parameters require applying two different shear stress 100 and 3200 Pa, each repeated for 10 cycles. Figure 3.6 shows a single cycle which is characterised by a 10-second-duration. Each cycle consists of 1 second of loading time and 9 seconds of recovery time. The testing procedure consists on firstly apply a shear stress of 0.1 kPa (for 10 cycles) and immediately after a 3.2 kPa shear stress (for additional 10 cycles).

Typically, the obtained raw-data are characterised by three different shear strain (γ) as shown in Figure 3.6. They are defined as follow:

- γ_p is the maximum shear stain at the end of the loading application (1 second);

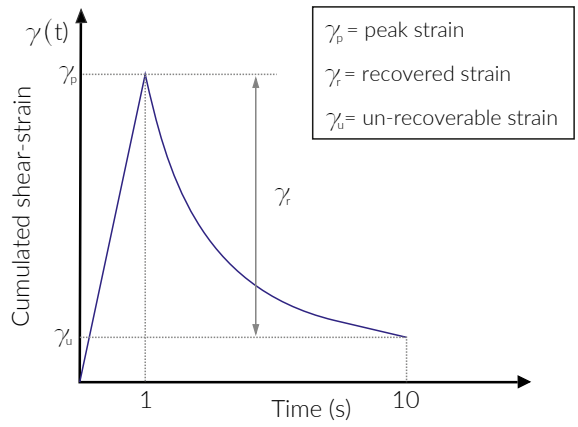

Figure 3.6 Typical MSCR test curve: single peak [8].

- γ_r is the recovered strain at the end of the recovering-time (9 seconds). It is equal to $\gamma_p - \gamma_u$;
- γ_u is the cumulated strain at the end of the ith cycle;

Deeply going onto describing the recovery capability of the investigating materials, R and J_{nr} need to be calculated and also better defined.

The R allows the evaluation of the material capability to recover the deformation due to the applied stresses: the higher is R the greater is the material recovery. This parameter is obtained through the following Equeation 3.11:

$$R = \frac{\sum_i^{10} E_{r_i}}{10} \quad , \qquad [\%] \tag{3.11}$$

where:

$$R_{r_i} = \frac{\gamma_{p_i} - \gamma_{u_i}}{\gamma_{p_i}} \tag{3.12}$$

The calculation of the parameters needs to be replicated for each applied load.

The J_{nr} evaluates the material permanent deformation aptitude. The higher is the J_{nr} value, the greater is the material tendency to accumulate permanent deformation. This parameter is obtained through the following Equation 3.13:

$$J_{nr} = \frac{\sum_i^{10} J_{nr_i}}{10} \quad , \qquad [1/kPa] \tag{3.13}$$

where

$$J_{nr_i} = \frac{\gamma_{u_i}}{\tau} \tag{3.14}$$

where τ is the applied stress which can be either 0.1 or 3.2 kPa. Thus, it is mandatory calculating the J_{nr} for both 0.1 and 3.2 stress cycles.

The calculating parameters allow plotting the so-called MSCR curve. Figure 3.7 shows the standard limit for asphalt binders which must be equal to 60% and also the R-J_{nr}-couples for 3.2 kPa stress. Combining both the mentioned limits defines the elasticity for the analysed materials [8, 123]. If the couples are over both the limits, the investigated material have enough elasticity for respecting the standard limits imposed by contractors.

More recently, several studies explained the important interaction which occurs between asphalt binder and filler [25, 44, 124]. With the introduction of this new "procedure", several studies were performed to understand the recovery behaviour of asphalt pavements by using the MSCR test at different HMA-stages [118, 125, 126]. For that reason the MSCR test has been used as a comparing-resource for better understanding mastic behaviours and also calibrating the new creep test for mastics.

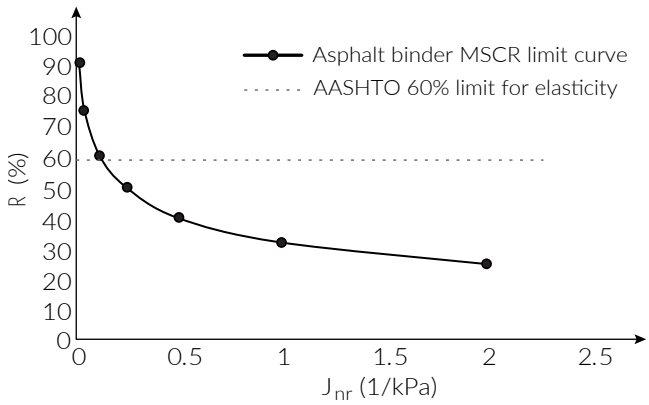

Figure 3.7 MSCR curve showing the standard limits for asphalt binders [8].

3.3. Specimen preparation

The materials described in the Chapter 2 were combined to obtain 14 combinations, 7 unmodified and 7 SBS polymer modified mixtures. The materials containing RAP were prepared considering two different RAP percentages (RAP%), 20% and 50%, respectively. Much more information are given into the following paragraph in which the mix-design of the materials containing RAP is explained. On the other hand, the phases containing LFS were prepared considering the "by-product" as 100% filler of the mixtures.

Before starting explaining the specimen preparation procedure, it is worth to give information about the labels used for indicating the tested materials, which are summarised in Table 3.1.

Focussing on one of the used labels (MR50, e.g.), it is possible to recognise the type of filler, the asphalt binder nature, and either the RAP% or the hydration process. By considering Figure 3.8, the first letter of the used labels indicates the nature of the asphalt binder, which can be 3.5% SBS Modified or Neat, while the second letter remarks the filler type. The last part of labels is a number, 20 or 50, when the RAP is used, while it is H or NH, which is based on whether the LFS hydration is performed or not.

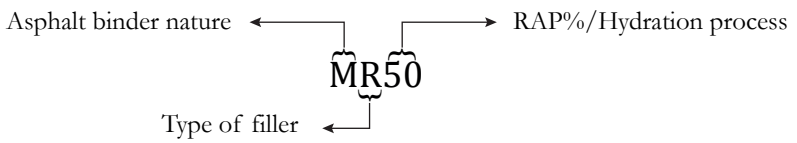

Figure 3.8 Label explanation.

Table 3.1 Summary of the used labels for indicating the tested materials.

Asphalt binder	Asphalt binder label	Filler	Filler label	Material label
SBS Modified	M	Limestone	L	*ML*
SBS Modified	M	Limestone + Hydrated lime*	A	*MA*
SBS Modified	M	Limestone + Hydrated lime**	F	*MF*
SBS Modified	M	LFS not hydrated	SNH	*MSNH*
SBS Modified	M	LFS Hydrated***	SH	*MSH*
SBS Modified	M	Limestone + 50% RAP	R50	*MR50*
SBS Modified	M	Limestone + 20% RAP	R20	*MR20*
Neat	N	Limestone	L	*NL*
Neat	N	Limestone + Hydrated lime*	A	*NA*
Neat	N	Limestone + Hydrated lime**	F	*NF*
Neat	N	LFS not hydrated	SNH	*NSNH*
Neat	N	LFS Hydrated***	SH	*NSH*
Neat	N	Limestone + 50% RAP	R50	*NR50*
Neat	N	Limestone + 20% RAP	R20	*NR20*

* 20% of SSA hydrated lime.

** 20% of standard hydrated lime.

*** LFS hydrated for 48 hours into a water bath.

3.3.1. MSCR specimen preparation

The sample preparation was done pre-heating both the asphalt binder used (N and M) and the fillers. The first one was placed in a draft oven at equiviscous temperature (160°C and 170°C for the N and M, respectively) up to becoming fluid (about 1 hour), while the filler needed to be recovered for 4 hours at mixing temperature 160°C to avoid the moisture damage of the mastic [127].

The pre-heated asphalt binder was placed in a heated 500-ml pot. Successively, the filler was gradually added in the 500-ml pot, and mixed with asphalt binder by a semi-mechanical procedure (it will be discussed further in the dissertation §4.3.1) to obtain the mastic.

The obtained materials were then poured in 25-ml vials to ease the pouring operation of the material directly on the 25-mm plate of the DSR.

3.3.2. RAP treatment procedures

The frameworks used to decide the treatment procedures for the RAP were: the Replaced Virgin Binder (RVB) procedure proposed by Lo Presti et al. [92] and improved by Jiménez

Del Barco Carrión et al. [9] for the computation of the proper virgin binder dosage in function of the RAP%, DoB% and RAb%, and the procedure proposed by Lo Presti et al. [85] which allows to evaluate the DoA of the analysed RAP.

Summarising, the RVB% represents the real percentage of virgin binder that will be replaced by RAP and rejuvenator [9]. It is calculated as follow:

$$RVB\% = 100 \cdot \frac{RAP\% \cdot DOB\% \cdot RAb\% \cdot (1 + REJ\ ratio)}{binder\ content\ in\ the\ mixtures} \qquad [9] \qquad (3.15)$$

where the RAP% is the total RAP percentage to add in the mixture by weight [9]; DOB% is the assumed degree of blending between RAP and virgin binders [9]; RAb% is the amount of aged binder contained in the RAP [9]; REJ ratio is the ratio between the rejuvenator content and the RAb (Rej/RAb) [9].

The evaluation of the correct mix design was divided into three parts: Evaluating which part of the RAP grading curve is the most active; Evaluating the DoA of the RAP with and without WCO treatment; Evaluating the RVB%.

In order to understand which part of the grading curve of the considered RAP has higher DoA, the reclaimed material was divided into two categories, %passing at 10 mm and %passing at 16 mm, respectively. After that, the Lo Presti et al. [85]'s procedure was performed considering: 140, 170 and 190°C as suitable temperatures for the RAP; and, 4 hour RAP pre-heating operation before Marshall compaction. The production of the specimens (3 for each combination) was done as follow:

- The RAP was dried at 40°C for 24 hours instead of 48 hours. This decision was made because the RAP stockpile was recovered into stockroom.
- The dried material was successively quartered and divided into three 1200-g-batches. Consequently they were recovered at the selected pre-heating temperatures for 4 hours before compaction.
- After the recovery time, the Marshall specimens were compacted performing 50 blows for each side of the specimens (EN 12697-30). After the compaction, the specimens into the moulds were allowed to cool down for 20 minutes.
- Successively, the specimens were de-moulded recovered at room temperature for at least 12 hours.
- The obtained specimens were undergone to thickness measurement and to the computation of the bulk density in order to analyse the air void content (AVC%) (EN 12697-6).
- Successively, the specimens were conditioned into a climatic chamber at 20°C for 12 hours. At the end of the cooling operation the specimens were tested by performing the ITS test (EN 12697-23).

The AVC% analysis showed that the minimum amount of voids was achieved at 140°C for both the considered part of the grading curve, as shown in Figure 3.9a. Looking at the high temperature (Figure 3.9a), the AVC% is similar at 140°C and 170°C, while at 190°C the %passing at 10 mm exhibited lower voids content than the other parts of the grading curve.

In terms of DoA% (Figure 3.9b), it is possible to recognise that the 100% activity, which is weighted on the max ITS value obtained for all the investigated temperature (Equation 2.5 at § 2.5.2), is achieved pre-heating the RAP at 170°C for both the analysed RAP categories.

By interpreting both AVC% and DoA% data (Figure 3.9), it is possible to define that there are not significant differences between the two grading parts of the analysed RAP. Therefore, the passing 16 mm grading was chosen as the reclaimed material to use.

After having decided the grading curve, the mix-design was focussed on the evaluation of the RVB% law (Figure 3.9c) [9], which was drawn by considering the penetration grade (Pen): 15.4 0.1 mm (Table 2.7), referring to the RAP; and, 70 0.1 mm and 80 0.1 mm for the neat and SBS modified bitumens (Table 2.2), respectively.

By considering the analysis previously described (AVC% and DoA%) and both the RAP% and the aged bitumen Pen, the hypothesised DoB% was 80%, as reported in Table

Table 3.2 Computation of the RVB% using the Jiménez Del Barco Carrión et al. [9]'s approach.

Virgin Binder	DoB%	RAP%	VB%*	RVB%	Pen. grade (0.1 mm)
Neat	80	20			
			4.7	15.46	55.25
			5.2	13.97	53.62
			5.7	12.74	54.89
Neat	80	50			
			4.7	38.64	33.50
			5.2	34.92	41.25
			5.7	31.86	43.21
SBS Modified	80	20			
			4.7	15.46	62.01
			5.2	13.97	63.55
			5.7	12.74	64.85
SBS Modified	80	50			
			4.7	38.64	42.33
			5.2	34.92	45.00
			5.7	31.86	47.33

* Virgin Binder content into the designed virgin mixture.

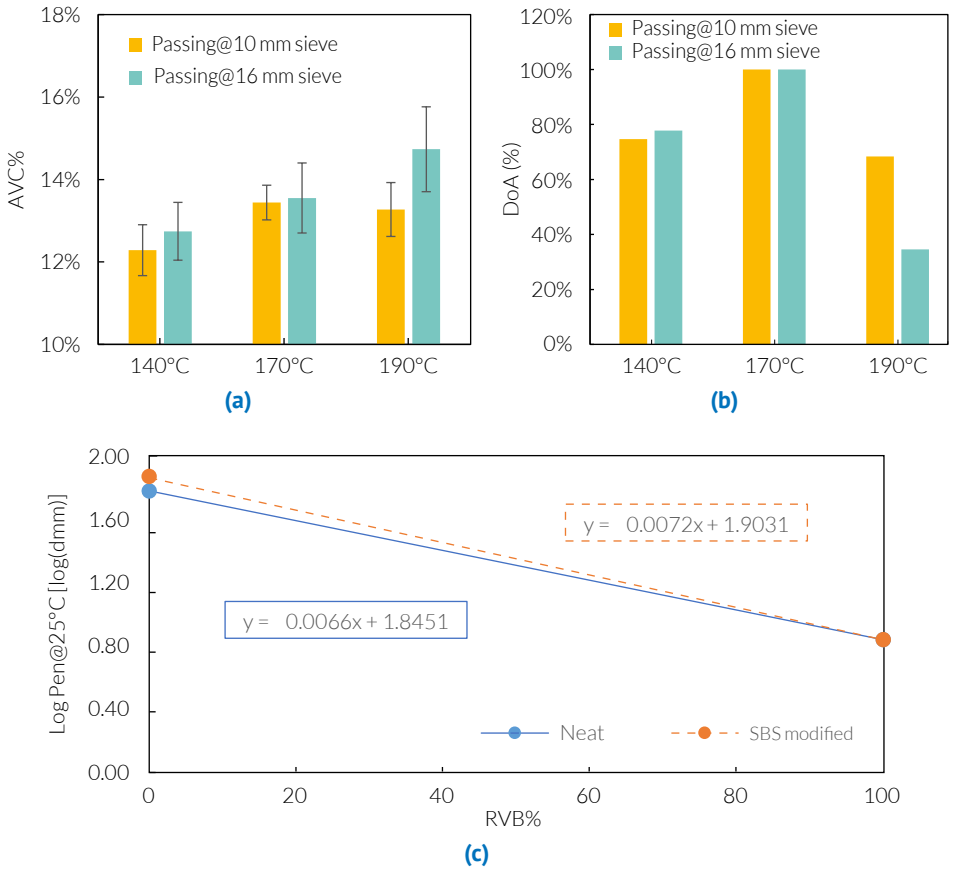

Figure 3.9 (***a***) AVC% analysis and DoA (***b***) computation of Marshall specimens made with different RAP grading. (***c***) Blending chart obtained by using the methodology proposed by Jiménez Del Barco Carrión et al. [9] to compute the RVB% law for both the used asphalt binders.

3.2. This decision was made by supposing a partial absorption of the re-activated aged bitumen (RAb = 15.4 0.1 mm) by virgin aggregates. This hypothesis was supported by the RVB concept which implies to subtract the RVB% to the virgin binder percentage (VB%). By using this concept, and considering the mixing process performed to obtain the HMAs, it was therefore expected a lower coverage of the virgin aggregates by the virgin binders, thus they will be coated by the RAb. After the coating process, both VB and RAb blend together.

Under this hypothesis, the RVB% and the expected penetration grade of the blended bitumen were calculated, and the results were shown in Table 3.2. As it is possible to recognise, for both the RAP% the expected Pen is upper or equal to the virgin binder one, except for the combination neat bitumen plus 50% RAP. Thus, the use of a rejuvenator was suggested only for this combination.

In order to be fair with introducing sustainable concepts and solution in the road and pavement infrastructures, the use of a WCO as rejuvenating additive was evaluated. The method used for this computation was not based on the RVB% because Jiménez Del Barco Carrión et al. [9] concluded that a right rejuvenator dosage has to be defined to obtain rejuvenating effects on the used RAP. For that reason, the right WCO% was established by using the Lo Presti et al. [85]'s method described above.

The WCO% design was therefore performed by finding the optimal trade-off between AVC% of 100%-RAP Marshall specimens, their ITS, and DoA%. Figure 3.10 summarises the results collected during the WCO% design.

The 50-blow Marshall specimens were prepared by following the same procedures previously described, but the RAP material was treated pouring the WCO directly on it during a short-mixing operation (1 min). The WCO dosage was calculated by the weight of the aged binder content. After that mixing operation, WCO treated materials were recovered for 2 hours at room temperature and, successively, for 2 hours into the draft-oven at considered temperature (140 °C and 170 °C)[2].

In terms of AVC% of the 50-blow Marshall specimens, the lower amount of voids was registered for the combination made with 10% of WCO (Figure 3.10a). The AVC% reduction obtained by passing from 100% RAP to WCO-treated 100% RAP specimens is into the range 2.5% - 3.5%, considering 140 °C recovered specimens, and 2.3% - 5.5%, for 170 °C specimens.

In terms of ITS, the maximum value was achieved by the materials treated with 6% WCO (by the weight of the RAb) pre-heated at 140 °C, while not significant variation were recorded for the RAP pre-heated at 170 °C and treated with the WCO, as shown in Figure 3.10b. In fact, the maximum ITS for the RAP pre-heated at 170 °C was achieved by the 100% not WCO treated RAP (Figure 3.10b). This difference is likely due to the

[2] 140 °C and 170 °C were considered because of for the passing at 16 mm grading curve the best AVC% was achieved at 140 °C, while the maximum DoA% at 170 °C. To be fair with the sustainability concept, the possibility of decreasing the pre-heating temperature was also considered as an opportunity for enhancing high level of CO_2 reduction.

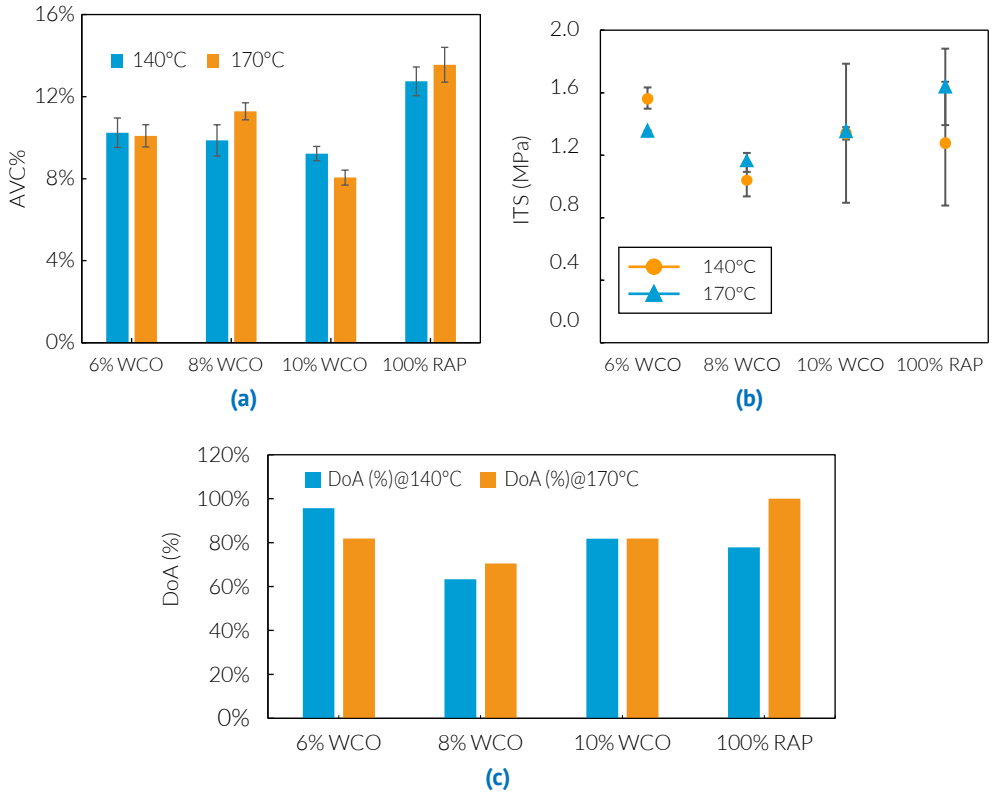

Figure 3.10 WCO effects on the AVC% (***a***) and ITS (***b***) of Marshal specimens prepared with 100% RAP pre-heated at 140°C and 170°C. Evaluation of the WCO% on the DoA (***c***).

softening effects of the WCO [107], which are emphasised when the RAP is treated with 8% WCO for both the pre-heating temperatures.

The DoA%, shown in Figure 3.10c, is weighted on the ITS, therefore it follows the same trend, which highlights the softening effects the specimens treated with 6% WCO and pre-heated at 140°C. However, the best trade-off in this case of study is not the 6% WCO treated material because the high ITS can signify that the reactivated RAb is very stiff, which may imply stiffening effects of the mixtures containing it. For the study herein, it was decided to use 10% WCO as good rejuvenator dosage for the neat mixtures containing 50% RAP.

The treatment characteristics and specifications for using the RAP in the mixtures has been summarised in Table 3.3. The chosen pre-heating temperature was 140 °C because there were no differences in terms of DoA especially when the WCO is used as rejuvenator. The duration of 4 hours, for the recovery period into the oven, was selected. It has to be considered split into two phases (2 hours at room temperature + 2 hours into the oven at

Table 3.3 Summary of the mix design for the mixtures containing RAP.

Bitumen	RA%	VB%	RVB%	WCO%	Pre-heating temperature
Neat	20%	5.20%	13.97%	-	140 °C
Neat	50%	5.20%	34.92%	10%	140 °C
SBS Modified	20%	5.20%	13.97%	-	140 °C
SBS Modified	50%	5.20%	34.92%	-	140 °C

- Not required.

140 °C) when the WCO was used.

3.3.3. Preparation of the HMA specimens

The HMA specimen preparation was performed using the SuperPave specification [111]. Their composition is summarised in Table 3.4 In order to respect the control points imposed by the mixing method, the virgin aggregates were firstly mechanically sieved with both wet and dry sieving operation, and successively two 6000 g batches were prepared for each mixture. The grading curve of the virgin aggregates has already been discussed in the Chapter 2 at § 2.3 (Figure 2.4) and also shown in Table 3.5. The mixtures containing RAP were designed substituting the virgin grading with the reclaimed one, and the RAP% were calculated by the total weight of the virgin aggregates (Table 3.5).

Since the interlocked skeleton provides the elastic response of HMAs, the same grading curve was used for all the analysed HMAs. This was decided to highlights the influence of fillers on the visco-elastic behaviour of HMAs.

After the batches filling operation, the HMA specimen preparation came along placing the batches into the oven at mixing temperature (which is the equiviscous temperature, 160 °C for the neat bitumen and 170°C for the SBS modified one, respectively) for 4 hours. A 500 ml pot, containing 360 g of filler, was also place in the draft oven.

The mixing operation continued putting the virgin aggregates into the mixer and mixing them for 1 minutes to homogenise the grading curve. Successively, the optimum asphalt binder content required by the grading curve used as reference (5.2% for all the mixtures) was added, and, consequently stirred for 1 minute to obtain a good coverage of the aggregates. After that, the filler was placed into the mixer and a 4 minutes mixing was performed. Considering the mixtures containing RAP, the reclaimed material, previously treated with the WCO when it is required, was introduced into the mixtures before adding the asphalt binder. This operation was done to achieve a good homogeneity between the RAP and virgin aggregates. Successively, the obtained mixtures were placed in the oven for two hours at 135 °C for short-term ageing. The obtained materials were split to obtain 1500 g and 4500 g specimens. Whilst, the first one was used to determine the maximum gravity density (G_{mm}) using the EN 12697-5, the other one was collected to obtain the

cylindrical Superpave specimens.

After these operations, materials were compacted by using the gyratory compactor

Table 3.4 Details of the 14 combination obtained by using the proposed materials.

Label	Asphalt binder	Aggregates	Filler
ML	SBS Modified	Limestone	Limestone
MA	SBS Modified	Limestone	Limestone + Hydrated lime*
MF	SBS Modified	Limestone	Limestone + Hydrated lime**
MSNH	SBS Modified	Limestone	LFS not hydrated
MSH	SBS Modified	Limestone	LFS Hydrated***
MR50	SBS Modified	Limestone + 50% RAP	Limestone + 50% RAP
MR20	SBS Modified	Limestone + 20% RAP	Limestone + 20% RAP
NL	Neat	Limestone	Limestone
NA	Neat	Limestone	Limestone + Hydrated lime*
NF	Neat	Limestone	Limestone + Hydrated lime**
NSNH	Neat	Limestone	LFS not hydrated
NSH	Neat	Limestone	LFS Hydrated***
NR50	Neat	Limestone + 50% RAP	Limestone + 50% RAP
NR20	Neat	Limestone + 20% RAP	Limestone + 20% RAP

* 20% of SSA hydrated lime.

** 20% of standard hydrated lime.

*** LFS hydrated for 48 hours into a water bath.

Table 3.5 Virgin grading curve expressed as holding percentage of the total amount of aggregates (6000 g) for both 100% virgin and RAP HMAs at each sieve used.

	Virgin grading		
Sieve (mm)	100% Virgin (%) (%)	50% RAP (%)	20% RAP (%)
12.5	7.00	2.61	5.24
10	8.00	2.77	5.91
5	32.00	16.30	25.72
2	16.00	3.52	11.01
1	12.00	6.66	9.86
0.5	8.00	3.95	6.38
0.2	4.00	1.88	3.15
0.106	3.00	2.55	2.82
0.075	2.00	1.87	1.95
<0.075	8.00	7.88	7.95

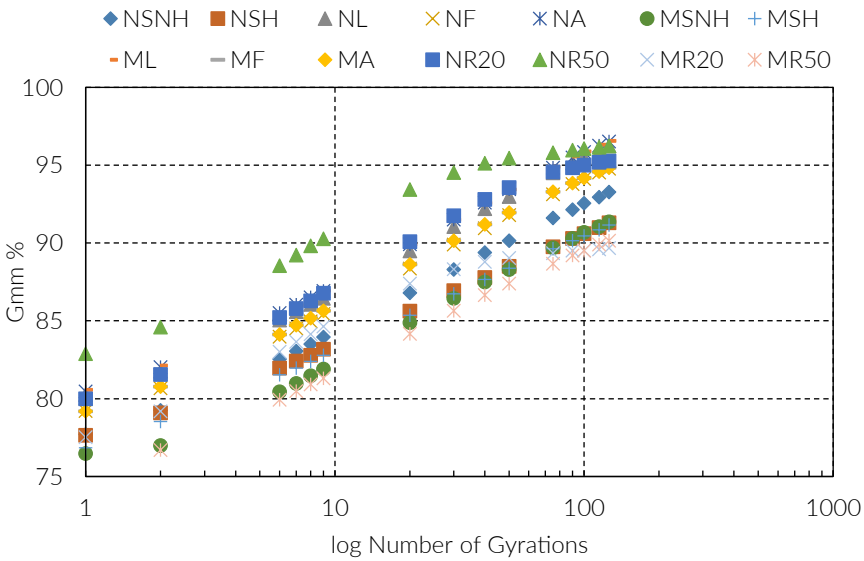

Figure 3.11 Compaction curves for the analysed HMA materials.

to obtain the 152 mm diameter cylindrical specimens. The machine was set to apply 600 kPa pressure and a number of gyrations equal to 126, which corresponds to high level of traffic. In order to understand how the mastics influence the workability and the compaction level of the mixtures, the same number of gyrations was applied. The compaction level of the specimens was evaluated recording the number of gyrations and the specimens' height.

Figure 3.11 shows the density curves of the mixtures . As expected, the compaction level of the mixtures containing LFS was lower then the others, this was due to the problems highlighted in § 2.5.1. Important consideration have to be done on the compacting behaviour of the mixture containing both limestone and limestone-based fillers. As noticeable, both L and A fillers behave similarly when are combined with both the bitumens used. The F-mixture showed the same bitumen-filler interaction for both the used bitumen (the mixtures achieved quite the same compaction level, as shown in 3.11), but the AVC% achieved was below the expected target (about 4%). Probably, in this case, the standard hydrated lime reacted with bitumen assembling a mastic material which was stiffer than the other limestone-based filler (A).

Considering the RAP-mixtures is possible to highlight that the NR50s and NR20s have quite the same compaction level (Figure 3.11). Both of them achieved quite the targeted AVC%. However, it have to be noticed that the NR50s quickly achieved the maximum Gmm% due to the selected number of gyrations (126) (Figure 3.11). The some behaviour was observed also for the MR20s, if compared to the MR50s (Figure 3.11). Conversely, their compacting level was lower than the mixtures prepared with the

Table 3.6 Summary of the volumetric characteristics of the analysed materials.

Material	G_{mm} (g/cm^3)	G_{mb} (g/cm^3)	AVC (%)*
ML	2.426	2.343	3.43
MA	2.423	2.337	3.57
MF	2.434	2.308	5.17
MNSH	2.445	2.400	8.63
MR20	2.676	2.337	10.33
MR50	2.592	2.265	9.85
MSH	2.485	2.263	8.85
NL	2.430	2.339	3.76
NA	2.438	2.353	3.48
NF	2.457	2.328	5.23
NR20	2.558	2.437	5.00
NR50	2.507	2.413	3.76
NSH	2.477	2.261	7.88
NSNH	2.477	2.310	6.73

* Determined at 126 gyrations.

neat bitumen.

The obtained specimens were then sawn to obtain two effective plates, each 30-40 mm thick, discarding the top and the bottom plates for reducing density gradient effect. For each mixture, four-cylindrical-shaped specimens were obtained and used to perform the SuperPave IDT test at 10 °C [5, 116].

The obtained IDT specimens were subjected to the bulk (G_{mb}) calculation by using the EN 12697-6 following the SSD procedure. The summary of the volumetric characteristics of the specimens were collected in Table 3.6. The obtained results confirmed the scarceness compacting capacity of the materials containing LFS, highlighting workability problems.

3.4. SuperPave IDT results

This section is focussed on introducing and discussing the results obtained by performing the SuperPave IDT protocol. The collected data can be split in two categories. The first one is focused on the mechanical characterization, while the second one inspects the energetic capability of the analysed mixtures.

The collected raw-data have been all analysed by designing a Matlab script for the SuperPave analysis, which has been shared in Appendix A. In the following paragraphs the results are discussed by grouping the data by the filler type. Therefore, three categories were defined: By-product, Conventional, Reclaimed. The first one represents the LFS

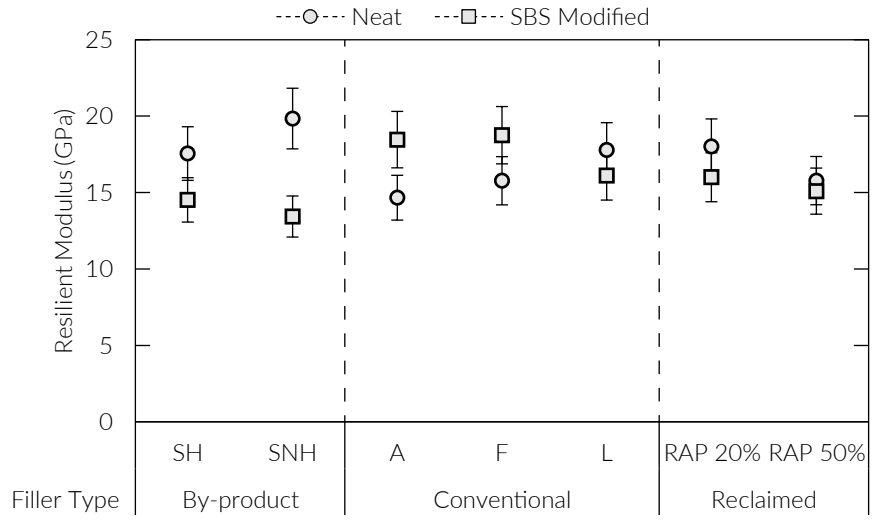

Figure 3.12 SuperPave IDT (at 10 °C) resilient modulus showing the differences between neat and SBS modified based mixtures.

hydrated and not hydrated materials, the second is the category of the conventional filler, and the third one is the RAP group.

3.4.1. Mechanical characterization

As mentioned above, the first test of the mechanical characterization is the resilient modulus (M_R) test which is performed to obtain the elastic stiffness of the material.

Firstly, considering the By-product group, the stiffness of the mixtures decreases when the alternative material is combined with the SBS modified bitumen (Figure 3.12). This, trend is likely due to the AVC% (Table 3.6). While, conversely, the M_R seems to increase when LFSs are mixed with the neat bitumen. In fact, both the mixtures containing LFS, either hydrated or not, achieved high elasticity level despite the high AVC% (Table 3.6). This may probably due to the different filler-bitumen phisico-chemical reaction. Those interactions are based on the heterogeneous chemical composition and grain topography of LFSs [59, 64, 128].

The Conventional group was not characterised by huge differences between the two analysed bitumen-based series, SBS modified and neat, respectively (Figure 3.12). This is likely due to the same grading curve, which firstly reacts when the HMAs are stressed by impulsive loads (this is also observed for the other analysed materials, excepting for the SNHs). However, the presence of the hydrated lime, either standard or SSA, increases the stiffness when it is combined with the SBS modified bitumen (Figure 3.12), conversely, when they are mixed with the neat bitumen the HMAs' stiffness decreases (Figure 3.12). This may be due to the stiffening effect described by Romeo et al. [129].

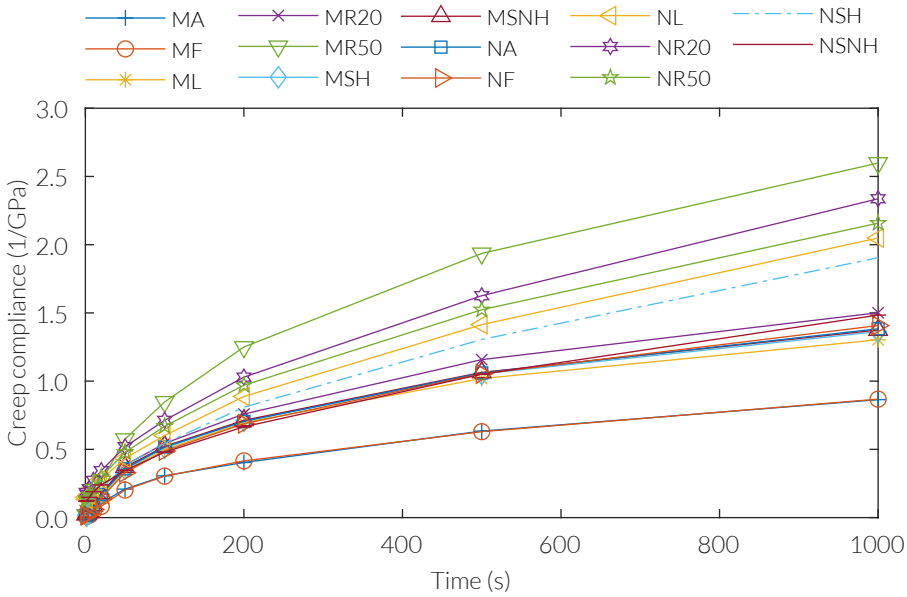

Figure 3.13 SuperPave IDT (at 10 °C) creep curve showing the differences between neat and SBS modified based mixtures.

The Reclaimed group does not show significant differences among the analysed materials. Nevertheless, the combination made using SBS modified bitumen could be affected by the partial softening effect of the WCO, which decreased the stiffness capability of the blended bitumen. However, both the RAP mixtures exhibited quite the same M_R of the MLs. This confirms that the used mix-design, for both WCO dosage and RVB% described in §3.3.2, is able to keep the best trade off for RAP-using. Analysing the neat series, both the materials showed good stiffness as the series prepared with SBS modified. This aspect confirmed the effectiveness of the proposed mix-design methods.

The second test performed aimed to evaluate the creep compliance (D(t)) which represents the susceptibility of the material to accumulate permanent deformation. The results of the creep compliance test are basically two: D(t) and m-value. The first one describes the accumulation of the deformation, while the m-value describes the accumulation rate.

The D(t) results were reported in Figure 3.13 and Figure 3.14. The curves have to be interpret as follow: the higher the curve and its values, the higher the susceptibility to accumulate deformation. As not expected [86, 94], analysing Figure 3.13, the higher D(t) curves are referred to the RAP mixtures. This is linked to the presence of the WCO which allows to reduce the viscosity of the used binders [103, 107]. The expected results was an increased level of permanent deformation resistance as well described by West et al. [94] and Sabouri et al. [86].

Analysing the results of the blends containing the by-products LFS (Figure 3.14a, and

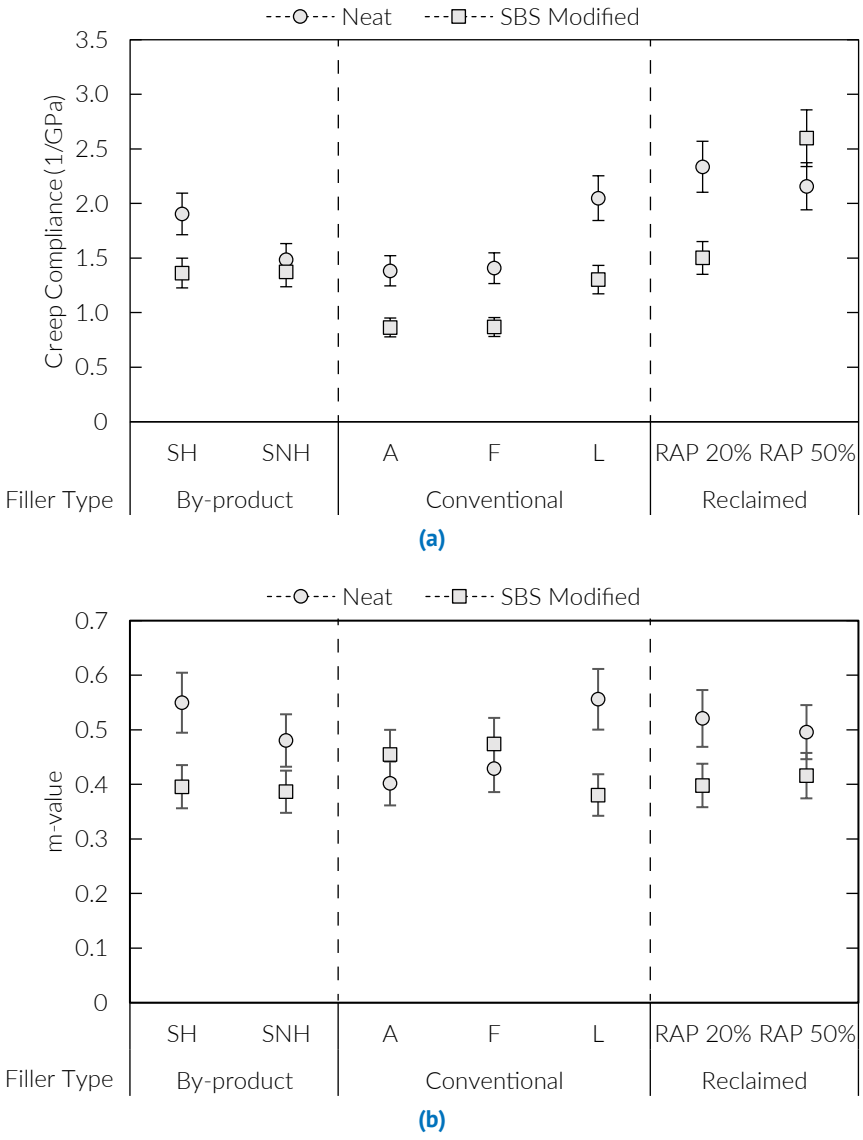

Figure 3.14 SuperPave IDT (at 10 °C) creep results showing the differences between neat and SBS modified based mixtures in terms of creep compliance ***(a)*** and m-value ***(b)***.

Figure 3.14b), it can be noticed that the asphalt binder type assumes a main role in the accumulation of deformations since the SBS modified mixtures show lower D(t)s and m-values. The presence of hydrated lime in the neat mixtures, has the ability to decrease the D(t) values, while it does not provide differences when SBS bitumen is present.

The results obtained for the conventional group confirm what observed before(Figure

3.14a, and Figure 3.14b). Bitumen type plays a fundamental role in D(t) definition: SBS modified mixes show lower values than neat mixes and, once again, the presence of hydrated lime provides benefits in terms of rate of permanent deformation. No significant differences were found between traditional and SSA hydrated lime.

The materials categorised in the Reclaimed group showed the highest D(t)s (Figure 3.14a). This might be linked to the WCO effects. In fact, the blended bitumen contained in the materials containing SBS bitumen and 50% RAP was highly affected by the WCO reactivating and softening actions. Those effects increased the deformation rate (Figure 3.13 and Figure 3.14b). On the other hand, the neat series showed quite the same behaviour. Nevertheless, the lower susceptibility to accumulate deformation was exhibited by the combination obtained mixing neat bitumen and 20%, if compared to the other RAP-mixtures.

The last test performed for the mechanical characterization was the tensile strength test which leads specimens to the failure points. Particularly, the tensile strength and the failure strain, which are shown in Figure 3.15, are both referred at the first fracture point, as discussed in §3.1.2. The results have to be interpret as follow: the higher the failure strain, the higher the deformability of materials; the higher the tensile strength, the higher the stiffness of the material. In order to have a good behaviour of materials, both the parameters have to be high. For example, if the tensile strength is high and the failure strain is low, this condition indicates that the material is brittle.

Discussing the Figure 3.15a, the high tensile strength of the material containing LFS (By-product group) was recognised despite the higher AVC% (Table 3.6). These results combined with the failure strain results (Figure 3.15b) highlight the stiffening effects of the LFS. This was observed for both the analysed condition (hydrated or not). The stiffening effect of the hydrated condition is lower (Figure 3.15b). Observing the SBS modified series that condition was not realised. This might linked to the elastic contribution of the SBS modified bitumen.

Considering the RAP-mixtures (Reclaimed group), it is possible to recognise the same brittleness problem as previously described. In this case, this is exhibited by both neat- and SBS modified-based materials (Figure 3.15b). This is likely due to the WCO effects (for the mixtures containing 50% of RAP) which is able to soften and reactivate the RAb, and to the stiffer RAb (for the mixtures containing 20% of RAP), which improve the brittleness of the blended asphalt binder.

On the other hand, considering the neat series, the Conventional group was distinguished by quite the same failure strain trend (Figure 3.15b), which indicates that the presence of the hydrated lime does not affect the deformability of the material. Differently, the SBS modified materials had a similar tensile strength (Figure 3.15). But, considering the failure strain results (Figure 3.15b), no significant differences were recognised.

Generally, the failure strain isinfluenced by the mastic behavior than the tensile strength. In fact, considering Figure 3.15b, it is possible to observe the same failure strain trend from

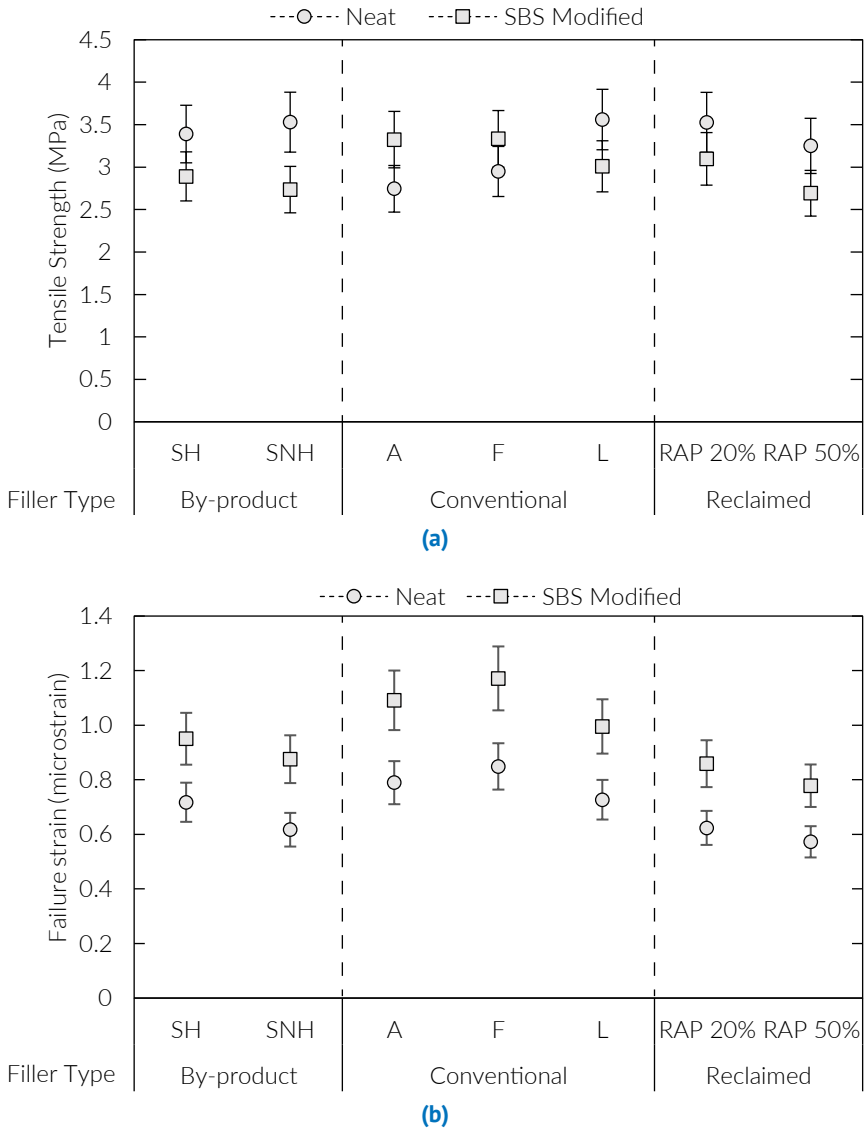

Figure 3.15 SuperPave IDT tensile strength ***(a)*** and failure strain ***(b)*** results showing the differences between neat and SBS modified based mixtures.

both the series of each group.

3.4.2. HMA fracture mechanic results

The energetic analysis proposed is based on the stress-strain curves of the materials at first fracture, as discussed in §3.1.2. The main parameters of the HMA fracture mechanic

framework [6, 7, 117] are discussed: fracture energy (FE), the dissipated creep strain energy (DCSE), and the elastic energy (EE).

The FE is calculated as the area below the stress and strain curves. This parameter represents the upper energetic threshold, which is the energy needed to break the material with a single heavy load.

The FE is composed by two components the DCSE and EE, which represent the energy dissipated due to the accumulation of the deformation (creep behaviour) and the energy accumulated in the material which allows to recover the deformation, respectively. The results obtained for the FE and its components were reported in Figure 3.16.

Figure 3.16a shows the FE results. As expected, the FE is higher for the mixtures prepared using the SBS-modified bitumen. On the other hand, the FE is quite constant for the neat bitumen-based materials.

By focussing on the SBS-modified series of both Reclaimed and By-product groups is possible to notice that the energy required to break the mixtures is lower than the other mixtures (Figure 3.16a).

Considering the RAP-mixtures (Reclaimed group) (Figure 3.16a), the mixture containing 50% of RAP showed low level of energy. Nevertheless, the data collected did not state differences among the materials made with either the Neat or the SBS Modified asphalt binders.

The FE capacity of the By-product group might depend by the AVC% (Table 3.6). This condition allows the modification of the internal structure of the materials during the test. In fact, the aggregates are not well interlocked. Nevertheless, the neat- and SBS modified-based materials similarly behave (Figure 3.16a) (the hydrated and not hydrated conditions).

Considering the Conventional group, the SBS modified series was characterised by the highest FE (Figure 3.16a). This proof that the action of the hydrated lime increased the capability of dissipating energy. It is worth highlight the lower FE of the HMAs containing A-filler than the F-filler materials. This might be due to the highest bitumen absorption capacity due to the SSA of the filler, which steals asphalt binder to the entire mixture, decreasing its dissipative capacity. Conversely, as already mentioned, materials prepared with the neat bitumen did not exhibited high FE level (Figure 3.16a).

Considering the FE components, DCSE (Figure 3.16b) and EE (Figure 3.16c), is possible to notice that the DCSE follows the same trend of the FE, while the EE is quite constant. This indicates that the prevalent component is DCSE.

The predominant role of the DCSE indicates that the analysed materials are able to dissipate a lot of energy before cracking. This dissipation is linked to the capacity of the material to accumulate permanent deformation. Consequently, the higher the DCSE, the higher the dissipating capability of materials.

Focussing on the Conventional group, the results of the study herein showed that SBS modified bitumen combined with both the active fillers (A and F) is able to achieve

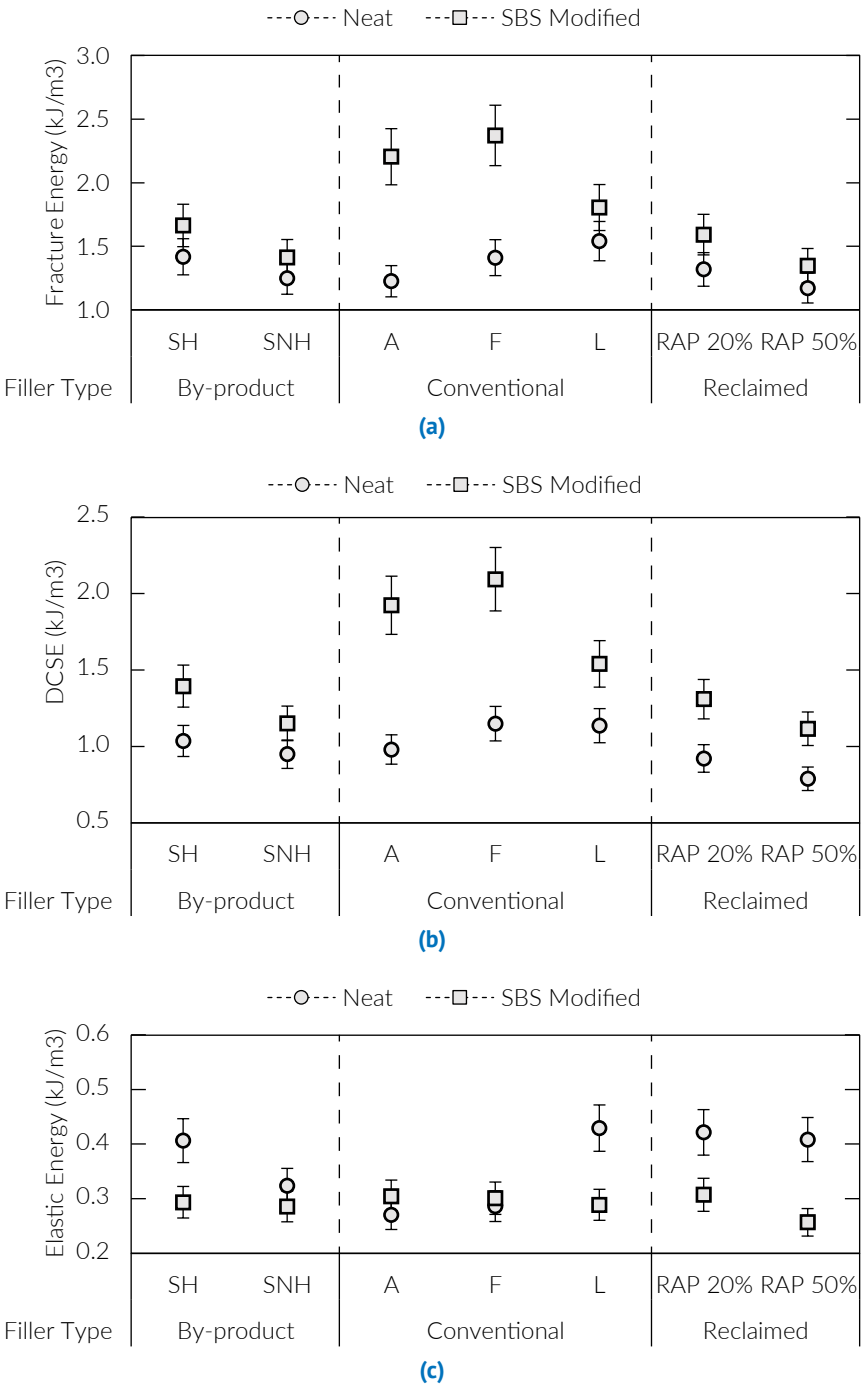

Figure 3.16 Fracture energy ***(a)*** and its components (dissipated creep strain energy ***(b)*** and elastic energy ***(c)***) results.

high level of dissipating capability before cracking (Figure 3.16b). This condition falls when the limestone substituted the A and F fillers. Conversely, the material made with neat bitumen, the DCSE is lower (Figure 3.16b). This highlights the possible differences among the chemical reaction filler-bitumen which can occur during the mixing and the ageing simulation.

Considering the Reclaimed group, the dissipative capacity of the materials made with neat bitumen is lower than the SBS modified-based materials(Figure 3.16b). Probably, considering 50% RAP content, the WCO content might highly soften the blended bitumen decreasing the capacity to accumulate the permanent deformation. While, 20% RAP materials' behaviour is likely linked to the presence of the not rejuvenated RAb.

Considering the By-product group is possible to notice that, despite the high AVC%, the dissipative capability is higher for the hydrated condition (Figure 3.16b), when it is combined with both the used bitumens. This could be due to the structural change of the LFS-filler. By focussing on the neat series of the group, it showed quite the same DCSE (Figure 3.16b).

Figure 3.16c shows the EE results. The materials obtained using the SBS modified bitumen exhibited the quite same EE, while the neat-bitumen-based materials showed a different energetic behaviour. Focussing on the HMAs made with neat bitumen, the EE increases for both the By-product and Reclaimed groups, but also when the L filler is used (Figure 3.16c). Probably, the neat bitumen differently reacts with those fillers slightly increasing the EE.

3.5. MSCR results

The analysed materials were investigated by using the DSR MCR-702 by Anton Paar, which is able to perform the MSCR data analysis excluding the measurements which exceed over the 10%-accuracy error weighted on the mean of the series. Therefore, the proposed bar-charts do not show error-bars. In order to better understand the MSCR data and to interpret them correctly, the neat and SBS modified combination results were separately explained. The testing configuration was the 25-mm plate-plate, and the temperature was the standard 64 °C.

As expected, the materials made with neat bitumen exhibited low elastic capacity for both the standard MSCR shear stress, as shown in Figure 3.17a. This was not confirmed for the materials NR50 and NSH which show an increased capacity to recover the deformation. For the NR50, this increase was likely due to the re-activation of the RAb, which is stiffer than the virgin bitumen. On the other hand, the NSHs were influenced by the LFS behaviour which is similar to an active filler. This was probably due to the fineness of the LFS which can cause an increasing of material viscosity.

Nevertheless, the material analysed had an elastic capacity lower the 60% elastic limit imposed by the Federal Highway Administration.

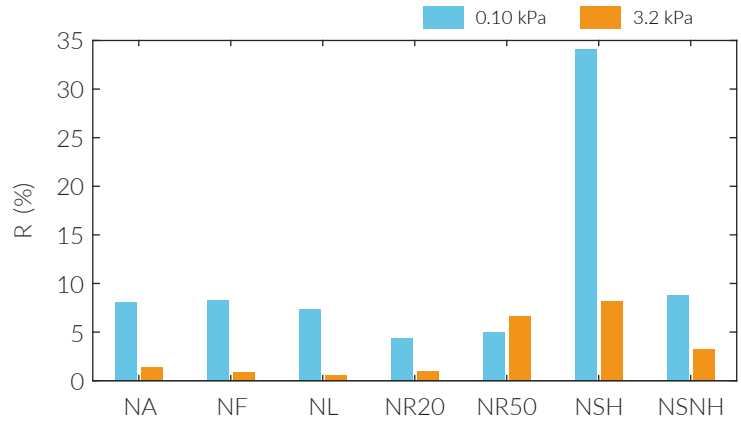

(a) *Elastic recovery results.*

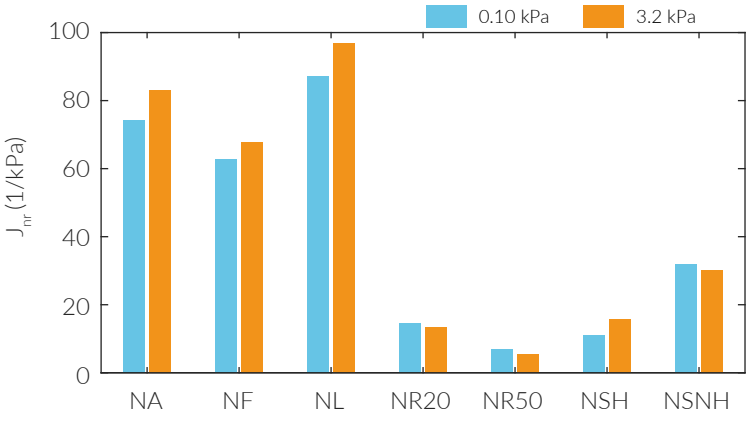

(b) *Non-recoverable creep compliance results.*

Figure 3.17 MSCR results for the materials prepared with the neat binder.

In terms of J_{nr}, which describes how prone the materials are to accumulate deformation, the results confirmed the analysis done for E_R, referring to NLs, NFs, and NAs (Figure 3.17b).

The material containing RAP (NR20 and NR50) showed lower aptitude to accumulate deformation. Thus, this equilibrium is likely due to the mix-design procedure used.

NSHs and NSNHs behave quite differently (Figure 3.17b). In fact, the differences should be due to the hydration process effects. Therefore, the presence of H_2O in the chemical interstitial of the Zeolite ($CaAl_2Si_7O_{18} \cdot 6\,H_2O$) could cause a partial moisture damage of the mastic.

The results of SBS modified-based mastics are shown in Figure 3.18. Considering the E_R data, it is quite clear that the elastic properties of the modified bitumen are not dependent by either the filler type or their nature (Figure 3.18a). However, the J_{nr} exhib-

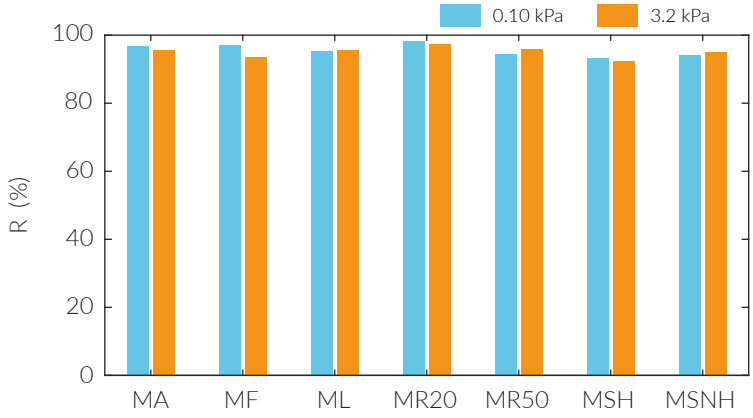

(a) *Elastic recovery results.*

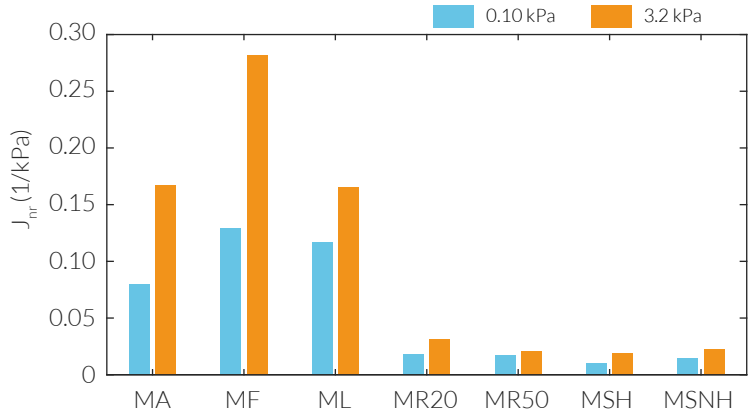

(b) *Non-recoverable creep compliance results.*

Figure 3.18 MSCR results for the materials prepared with the SBS modified binder.

ited a connection with filler characteristics. Thus, mastics made with both limestone and limestone-based fillers (MA, ML and MF) showed high level of J_{nr}, if compared to the others (Figure 3.18b). The materials containing RAP (MR20 and MR50) and LFS (MSH and MSNH) were characterised by low proneness to accumulate deformation which could be affected by the increased stiffness and viscosity (Figure 3.18b).

4

The new tensile creep test

As explained in the Chapter 1, in the last few years, several studies have proposed different tests and models to analyse the mechanical behaviour of the different phases which compose HMAs.

By focussing on the creep behaviour, not much attention has been given to the accumulation of the permanent deformation at different HMA scales. Currently, the increasing traffic level and climatic change are exacerbating the premature distress of pavement infrastructures. Therefore, introducing a multi-scale approach to interpret the role of the different HMA scales is important for either evaluating the mechanical behaviour or analysing the dissipative energy capacity of the materials.

In order to achieve this important aim, a proper testing protocol for mastics was developed. The main task was to establish the correct testing duration, load and temperature. The main assumption of the proposed study was: the analysed materials have to keep the linear visco-elastic (LVE) behaviour in the small strain domain, observing the HMA fracture mechanic framework principles (§3.1.2). A material is defined to behave linear-viscoelastically if the stress is proportional to the deformation at a given time and, furthermore, if the principle of linear superposition applies. [10, 41]. The mathematical statement of the linear requirements can be described by the following two equations:

$$\varepsilon\left[c \cdot \sigma(t)\right] = c \cdot \varepsilon\left[\sigma(t)\right] \qquad [10] \tag{4.1}$$

$$\varepsilon\left[\sigma_1(t) + \sigma_2(t - t_1)\right] = \varepsilon\left[\sigma_1(t)\right] + \varepsilon\left[\sigma_2(t - t_1)\right] \qquad [10] \tag{4.2}$$

where c is an arbitrary constant, σ is the stress input, and ε is the strain output. The square brackets represent that the response is a function of the input history [41].

$$\varepsilon = \varepsilon^e + \varepsilon^c \tag{4.3}$$

Considering both the creep, which is a slow continuous deformation under a constant stress σ, and the linearity definition (Equation 4.1, and 4.2), the strain ε (Equation 4.3)

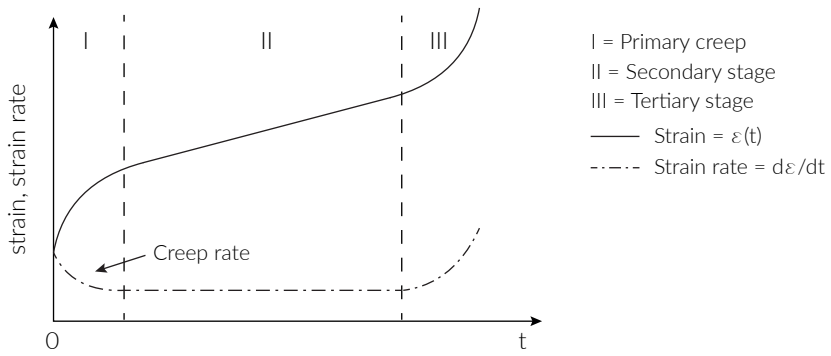

Figure 4.1 Three stages of Creep [10].

at time t is the sum of the instantaneous elastic strain ε^e and creep strain ε^c. It is worth to remark that, for linear materials in the small strain domain, the constant load and constant stress experiments are the same [10]. This assumption is true if the cross-sectional area of the specimens remains constant (without significant change) over time [10].

Under those conditions, the creep of a linear material can be divided in three stages, as shown in Figure 4.1. Visco-elasticity is concerned with the materials which exhibit strain rate ($d\varepsilon/dt$) effects in response to applied stresses [10].

Considering the Equation 4.3 and the three stages drawn in Figure 4.1, the ε^e is constant in the time domain. Consequently, the following mathematical definitions of both the strain rate ($d\varepsilon/dt$) and $\varepsilon(t)$ can be expressed:

$$\frac{d\varepsilon^c}{dt} = \frac{d\varepsilon}{dt} \tag{4.4}$$

$$\varepsilon(t) = \int_{t_1}^{t_2} J(t-\xi)\frac{\partial\sigma(\xi)}{\partial\xi}d\xi \tag{4.5}$$

The model used to interpret the LVE behaviour [41, 130–132] of mastics was the Kelvin-Voigt model (Figure 4.2a). This is characterised by a spring element and a dashpot element connected in parallel.

For the Kelvin-Voigt model, the material response, specifically considered under a uniaxial constant load in the herein study, can be split in two parts, creep and recovery as shown in (Figure 4.2a). The first one describes the material aptitude to accumulate deformation (loading condition), while, the second allows to understand the material capacity to recover the deformation (un-loading condition). The proposed study bases on the creep behaviour evaluation, thus it focussed on the loading condition.

By considering the definition given above, during a creep test the $\varepsilon(t)$ can be represented by:

$$\varepsilon(t) = J(t) \cdot \sigma \tag{4.6}$$

or

$$J(t) = \frac{\varepsilon(t)}{\sigma} \tag{4.7}$$

where $J(t)$ is the creep compliance, t is the time in seconds, $\varepsilon(t)$ is the measured deformation expressed in microstrain at time t, $\sigma = P/A = const$ is the stress due to the applied load P, and A is the specimen cross section area (200 mm^2).

The $J(t)$ is the creep strain per unit of applied stress. Creep compliance is a material property [10].

The creep behaviour has been analysed considering the Power model shown in Figure 4.2b. This model is based on three parameters: D_0, D_1, and m-value. Where, D_0 is strictly linked to the non-time-dependent behaviour of the materials (ε^e). D_1 and the m-value are related each other. Nevertheless, D_1 is much more linked to the first part

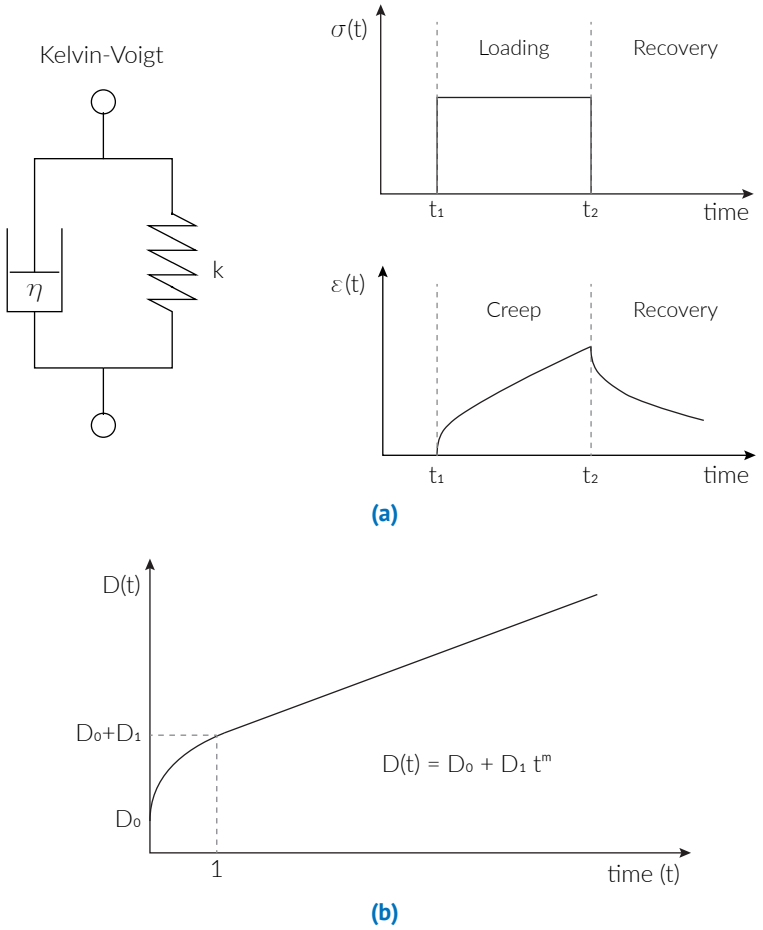

Figure 4.2 ***(a)*** Kelvin-Voigt model and the visco-elastic material behaviours under a constant load. ***(b)*** Power model of the creep compliance.

of the creep compliance curve, while the m-value is related to the long-term part of the curve.

Focussing on the m-value, it represents the accumulation rate of the deformation, which means that the higher the m-value, the faster is the accumulation of the deformation. Therefore, materials distinguished by high m-value typically have limited DCSE (§3.1.2). Reporting those concepts to the mastic phase, the m-value could be interpret as an indicator of the energy dissipating capacity.

The following paragraphs aim at explaining the statistical characterization framework used, the new testing procedure, the developed machine specifically designed for the creep behaviour evaluation of mastics.

4.1. Statistical analysis framework

Before starting explaining the overall laboratory campaign, the statistical approaches used for validating the test are shown in terms of accuracy, trueness and precision (repeatability and reproducibility). These parameters define the quality of the test. The concept of quality is not simple to define, but it can be considered inversely proportional to the variability of the test: the higher the quality, the lower the variability [11].

Before starting explaining the statistical framework, it is worth defining the *accuracy*, *trueness*, *repeatability* and *reproducibility* concepts.

Accuracy refers to the ability of the instrument to measure the true value correctly on average [11].

The *trueness* of a measurement is referred to the closeness between the mean of a large number of results and the true of an accepted reference value [133].

Repeatability is the variation caused by the instrumentation or the variation observed when the same operator measures the same part more times with the same instrumentation [134].

Reproducibility is the variation caused by the measurement system or the variation observed when different operators measure the same part with the same instrumentation [134].

Summarizing, the repeatability is good represented when the variability of measurements is low, while the reproducibility is linked to the stability of a measurement process [11, 134, 135].

The visual summary of both the accuracy and precision concepts were reported into Figure 4.3.

The analyses were focussed on taking into account the m-value, the creep compliance (J) and the maximum deformation (ε_{max}), which are usually used for understanding the creep behaviour also by standard tests, as reported into Chapter 3.

The analyses were performed by designing a MATLAB script, which is shown in Appendix A.

4.1.1. Trueness and accuracy of the test

In order to evaluate the accuracy and trueness of the designed method, the performed test replication were statistically analysed. The selected test is the t-test by Student, which allows to understand whether the mean of the measurements is representative of the paired sample or not. For that purpose, the bilateral option was selected.

Framework for the m-value analysis

By assuming the **T** and **Y** as the time and the deformation matrices, respectively, and considering a generic data series, the m-value of the i-th group of both **T** and **Y**, which represents the slope of the straight line passing at the considered points, can be calculated

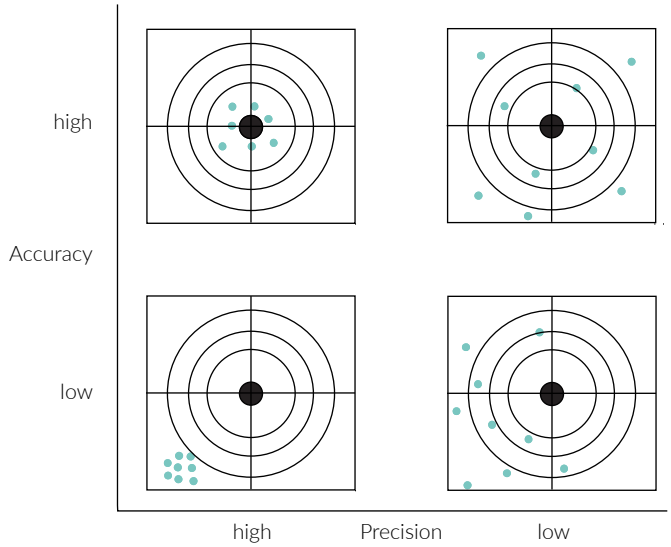

Figure 4.3 Summary of accuracy and precision [11].

by using the Equation 4.8.

$$\mathbf{T} = \begin{bmatrix} t_{11} & \cdots & t_{1j} & \cdots & t_{1m} \\ \vdots & \cdots & \vdots & \cdots & \vdots \\ t_{i1} & \cdots & t_{ij} & \cdots & t_{im} \\ \vdots & \cdots & \vdots & \cdots & \vdots \\ t_{n1} & \cdots & t_{nj} & \cdots & t_{nm} \end{bmatrix} \qquad \mathbf{Y} = \begin{bmatrix} y_{11} & \cdots & y_{1j} & \cdots & y_{1m} \\ \vdots & \cdots & \vdots & \cdots & \vdots \\ y_{i1} & \cdots & y_{ij} & \cdots & y_{im} \\ \vdots & \cdots & \vdots & \cdots & \vdots \\ y_{n1} & \cdots & y_{nj} & \cdots & y_{nm} \end{bmatrix}$$

$$m - value_{ij} = \frac{\mathrm{d}y}{\mathrm{d}t}|_{t_{ij}} = \frac{y_{ij} - y_{ij-1}}{t_{ij} - t_{ij-1}} \tag{4.8}$$

where:

- $m - value_{ij}$ is the m-value of the i-th group;
- $t_{ij} \neq 0$, and $i = 1, \ldots, n$ indicates the number of observation;
- $j = 1, \ldots, m$ indicates the number of performed tests;
- y_{ij} is the deformation measured at time t_{ij}.

As understandable, due to the dispersion of the data, the calculation of the differential point by point (Eq. 4.8) gives back three possible eventualities, as shown in Figure 4.4. This conditions imply that the calculation of the average m-value is difficult and often could be not consistent.

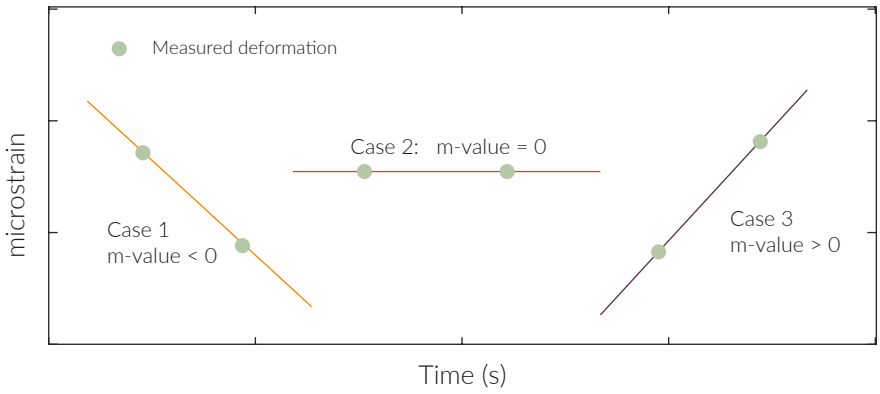

Figure 4.4 Possible eventualities during the calculation of the m-value point by point.

The designed MATLAB script allows to go beyond this problem by considering a least square fitting procedure of the analysed curves. The considered fitting method were essentially two: linear and non-linear. The first model needs to analyse only the linear part of the $\varepsilon(t)$, while the second one allows to directly fit the whole measured $\varepsilon(t)$.

The linear is based on finding abrupt points of the data series, using the function *findchangepts* and its results are showed by plotting a figure.

Consequently, the linear range is selected by using the function *selectdata*, and its data are least square fitted running *polyfit*. Since the range is linear, the used fitting model is also linear ($y = ax + b$). Through this operation both a and b are computed. The slope of the fitting model is represented by its first derivative. Therefore, the function *polyder* is used for evaluating it, which represents the *m-value* which this study is looking for.

On the other hand, the non-linear fitting model is based on the Power model. Therefore, the Matlab curve fitting app (included into the toolbox called Statistic and Machine Learning) was used, allowing to fit data series through a custom equation $D(t) = D_0 + D_1 t^m$. This model is based on three parameters D_0, D_1 and m. The third parameter m is linked to the strain rate of materials, and it represents the m-value.

Considering both the fitting models, the above described sequences were repeated for each test. Due to this, for each material a column array named $m\text{-}value_{fit}$ is generated. Successively, it was compared to the m-value of the average curve ($m\text{-}value_{avg}$). The average curve was calculated considering each row of $\mathbf{Y}$ as a subgroup of measurements taken at the same time.

For this study, the chosen confidence interval (CI) was 95%, which implies a significant level equal to 5% ($\alpha = 0.05$). The null hypothesis H_0 (Eq. 4.10) is not rejected if the *p-value* of the test, which represents the probability to exceed CI, is higher than α, otherwise, the H_0 is rejected. In this case, if H_0 is not rejected, it means that the $m\text{-}value_{avg}$ is representative of the group $m\text{-}value_{fit}$. These operations were performed for each analysed

material.

$$m-value_{fit} = \begin{bmatrix} m-value_1 \\ \vdots \\ m-value_j \\ \vdots \\ m-value_n \end{bmatrix}$$

$$\mu = \frac{\sum_{j=1}^{n} m-value_j}{n} \qquad \mu_0 = m-value_{avg} \tag{4.9}$$

$$H_0 : \mu = \mu_0 \qquad H_1 : \mu \neq \mu_0 \qquad (bilateral\ case) \tag{4.10}$$

where:

- H_0 is the null hypothesis of the t-test;
- H_1 is the alternative hypothesis of the t-test;
- μ is the mean of the paired samples ($m\text{-}value_{fit}$);
- μ_0 is the $m\text{-}value_{avg}$;
- $j = 1, \dots, n$ indicates the generic performed test;
- n is the number of tests performed.

The *t-test by Student* was performed by using also the MATLAB script (*ttest* function), which gives back also other important information such as the standard deviation, and both the lower and upper control limits of the 95% CI, indicated as UCL and LCL, respectively. Since the 95% CI was selected, the error of the measured data was calculated as 2 times the standard deviation of the data (Equation 4.11).

$$\delta = \pm 2 \cdot StD, \qquad StD = \sqrt{\frac{\sum_{i=1}^{n}(x_i - \overline{x})^2}{n-1}} \tag{4.11}$$

where δ is the error of the paired sample, StD is the standard deviation, x_i is the value of the i-th point in the data set, $\overline{x}$ is the mean value of the data set, and n is the number of the observation. The calculated δ has been used to draw the errorbars in the proposed m-value chart.

Figure 4.5 shows the accuracy and repeatability of both the analysed fitting models. As it is possible to recognise, the non-linear model and the linear one are able to evaluate the same value for the parameter *m-value*. The main difference is noticeable in terms of errorbars. This remarks quite the same accuracy for both the used models, but the repeatability of the non-linear results is higher. For that reason, the non-linear model was used for evaluating the m-value of the analysed material.

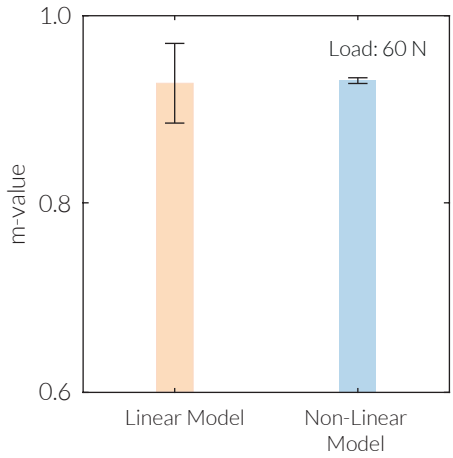

Figure 4.5 Comparison between the non linear and linear fitting model.

Framework for the maximum deformation analysis

The evaluation of the trueness and accuracy of the ε_{max} was based on considering $\mathbf{Y}$ the array of the ε measurements for each performed test (taking into account one material at time).

Also this procedure is based on fitting the linear range of the measurements by using a least square non-linear model ($D(t) = D_0 + D_1 t^m$), as previously described. After computing both the model's parameters, ε_i was evaluated for each column of the $\mathbf{T}$ array, which is the duration of each test, by calculating the ε_i at time t. The maximum fitted deformation was collected into a vertical array $\mathbf{E}$ for each sample. The mean of $\mathbf{E}$ is compared to the ε_{avg}, which is the maximum deformation of the mean curve obtained as described for the *m-value* case.

$$\mathbf{Y} = \begin{bmatrix} y_{11} & \cdots & y_{1j} & \cdots & y_{1m} \\ \vdots & \cdots & \vdots & \cdots & \vdots \\ y_{i1} & \cdots & y_{ij} & \cdots & y_{im} \\ \vdots & \cdots & \vdots & \cdots & \vdots \\ y_{n1} & \cdots & y_{nj} & \cdots & y_{nm} \end{bmatrix} \qquad \mathbf{E} = \begin{bmatrix} \varepsilon_1 \\ \vdots \\ \varepsilon_i \\ \vdots \\ \varepsilon_m \end{bmatrix}$$

$$\mu_\varepsilon = \frac{\sum_{i=1}^{n} \varepsilon_i}{m} \qquad \mu_0 = \varepsilon_{avg} \tag{4.12}$$

$$H_0 : \mu_\varepsilon = \mu_0 \qquad H_1 : \mu_\varepsilon \neq \mu_0 \qquad (\textit{bilateral case}) \tag{4.13}$$

where:

- H_0 is the null hypothesis of the t-test;
- H_1 is the alternative hypothesis of the t-test;

- μ is the mean of the paired samples (**E**);
- μ_0 is the ε_{avg};
- $i = 1, \dots, n$ indicates the generic performed test;
- n is the number of tests performed.

As above, the chosen confidence interval (CI) is 95%, which implies a significant level equal to 5% ($\alpha = 0.05$). The null hypothesis H_0 (Eq. 4.13) is not rejected if the *p-value* of the test is higher than α, otherwise, the H_0 is rejected. In this case, if H_0 is not rejected, it means that the ε_{avg} is representative of the group **E**. These operations were performed for each analysed material.

Also for this part of the statistical framework both UCL and LCL were computed by using the *ttest* MATLAB function considering a 95% CI.

Since the 95% CI was selected, the error of the measured data was calculated as 2 times the standard deviation of the data (Equation 4.11). The calculated δ has been used to draw the errorbars in the proposed ε chart.

Framework for the creep compliance evaluation

The evaluation of the creep compliance of the analysed materials starts from the collected ε measurements, which are all collected in the matrix **Y**. The columns of **Y** indicate the repetition of tests performed. For each analysed material the **Y** matrix was set.

Considering the hypotheses given at the beginning of this Chapter 4, the creep compliance $J(t)$ is evaluated as follow:

$$\mathbf{J} = \mathbf{Y} \cdot \frac{1}{\sigma} \tag{4.14}$$

where **J** is the matrix containing the creep curve for each analysed sample, **Y** is the matrix containing the measured ϵ, and σ is the stress due to the applied load.

The Equation 4.14 can be also expressed as function of the creep curve of the i-th sample as follow:

$$J_i(t) = \frac{\varepsilon_i(t)}{\sigma} \tag{4.15}$$

where $J_i(t)$ is the creep curve of the i-th analysed sample, $\varepsilon_i(t)$ is the array containing the measured deformation of the i-th group during the test, and σ is the stress due to the applied load.

In order to obtain the $\mathbf{J}_{avg}$, which represents the average creep curve of the collected data, the $J_i(t)$s were fitted with the non-linear Power model ($D(t) = D_0 + D_1 t^m$). The fitted values were all collected in the $\mathbf{J}_{fit}$ matrix.

As for the mixtures, the creep compliance for mastics has been calculated at the end of the test (the duration of the test will be further introduced in §4.3.5). Due to this

assumption, the mean of the last row of $\mathbf{J}$ (j_avg) has been statistically compared with the last row of the $\mathbf{J}_{fit}$ through the *t-test by Student* considering the following equations and hypotheses:

$$\mu_j = \frac{\sum_{i=1}^{n} j_i}{m} \qquad \mu_0 = j_{avg} \tag{4.16}$$

$$H_0 : \mu_j = \mu_0 \qquad H_1 : \mu_j \neq \mu_0 \qquad (\textit{bilateral case}) \tag{4.17}$$

where:

- H_0 is the null hypothesis of the t-test;
- H_1 is the alternative hypothesis of the t-test;
- μ is the mean of the paired samples (last row of $\mathbf{J}_{fit}$);
- μ_0 is the j_{avg};
- $i = 1, \dots, n$ indicates the generic performed test;
- n is the number of tests performed.

As above, the chosen confidence interval (CI) is 95%, which implies a significant level equal to 5% ($\alpha = 0.05$). The null hypothesis H_0 (Eq. 4.17) is not rejected if the *p-value* of the test is higher than α, otherwise, the H_0 is rejected. In this case, if H_0 is not rejected, it means that the j_{avg} is representative of the last row of $\mathbf{J}_{fit}$. These operations were performed for each analysed material.

Also for this part of the statistical framework both UCL and LCL were computed by using the *ttest* MATLAB function considering a 95% CI.

Since the 95% CI was selected, the error of the measured data was calculated as 2 times the standard deviation of the data (Equation 4.11). The calculated δ has been used to draw the errorbars in the proposed $\mathbf{J}$ chart.

4.1.2. Repeatability and reproducibility

Different frameworks are able to interpret and analyse the repeatability and reproducibility of the engineering experiments [11, 134, 135]. The study herein proposes to achieve accurate interpretation of the repeatability of the new test procedure by using the one-way ANOVA method.

The reproducibility and repeatability errors are generally linked to random variations of the properties and the fluctuation of some factors (such as operators, equipment and environmental properties), which are generally indicated as treatments. This errors can be divided in two different categories called *within laboratory variability* (s_r^2) and *inter-laboratory variability* (s_L^2) [136]. Their sum represents the reproducibility variability.

In this study, the s_r^2 was taken in consideration. In order to evaluate the effects of these error, the variation due to the treatment was considered as measurement variability.

The mathematical ANOVA framework was originated from the inferential statistic theory, which is able to analyse the variability of the collected data. The analytical model which describes the variability of *i-th* random observation due to *j-th* treatment can be described as follow:

$$y_{ij} = \mu_i + \epsilon_{ij} \qquad \begin{cases} i = 1, 2, ..., a \\ j = 1, 2, ..., a \\ \mu_i = \mu + \tau_j \end{cases} \tag{4.18}$$

where n is the number of observation, μ_i is the mean of the *i-th* group of measurements, τ_j is the effect due to the treatment, and ϵ_{ij} is the random error of the *j-th* observation.

Since the one-way ANOVA is based on the analysis of variance, the following hypothesis can be accepted:

$$H_0 = \mu_1 = \mu_2 = \cdots = \mu_a = 0 \qquad H_1 = \mu_i \neq 0 \tag{4.19}$$

where H_0 and H_1 represent the null hypothesis and the alternative hypothesis, respectively.

By solving the equality of the means, it is possible to re-write H_0 and H_1 as function of the effects due to the treatment. Considering that the following relationship are valid:

$$y_i = \sum_{j=1}^{n} y_{ij}; \qquad \overline{y_i} = \frac{y_i}{n}; \qquad y = \sum_{i=1}^{a}\sum_{j=1}^{n} y_{ij}; \qquad \overline{y} = \frac{y}{N}; \tag{4.20}$$

where $N = a, \cdots, n$ and $i = 1, \cdots, n$.

By doing this observation, the variability can be described as sums of the squares of the deviations of the average values [134]:

$$\sum_{i=1}^{a}\sum_{j=1}^{n}(y_{ij} - \overline{y})^2 = n\sum_{i=1}^{a}(\overline{y_i} - \overline{y})^2 + \sum_{i=1}^{a}\sum_{j=1}^{n}(y_{ij} - \overline{y_i})^2 \tag{4.21}$$

which represent the fundamental equation of ANOVA.

Considering the null hypothesis and the expected value for each term of the Equation 4.21, the mean of the squares of the treatment ($MS_{Treatment}$) and the sum of the square of errors (MS_{Error}) can be defined as follow:

$$MS_{Treatment} = \frac{n\sum_{i=1}^{a}(\overline{y_i} - \overline{y})^2}{a-1} \tag{4.22}$$

$$MS_{Errors} = \frac{\sum_{i=1}^{a}\sum_{j=1}^{n}(y_{ij} - \overline{y_i})^2}{a(n-1)} \tag{4.23}$$

$$F_0 = \frac{MS_{Treatment}}{MS_{Errors}} \tag{4.24}$$

The ratio between Equation 4.22 and Equation 4.23 defines the F_0 (Equation 4.24), which, if the a population is described by a normal distribution, and if the null hypothesis is true, has a Fisher distribution distinguished by $(a-1)$ and $(N-a)$ degree of freedom (DF).

By analysing the *p-value* of each F_0 value, and comparing it with the level of significance α (5%), it is possible to define whether the null hypothesis is accepted ($p-value > \alpha$) or not ($p-value < \alpha$). Refusing the H_0 means that among the observed data there may be significant differences. Vice versa, it means that the measurements differ by the effect of the random error.

The ANOVA was performed by using a Matlab script able to collect the data and to organise a a x N matrix. Consequently, the data are analysed by running the *anova1* (one-way ANOVA). The obtained statistical results are then analysed using the *multicompare* command able to highlight how distant are the observed population. The whole-script was shared in the Appendix A.

4.2. Measurement systems

In the last few years, several studies [13, 25, 129, 137–142] successfully used the DIC measuring system to evaluate the mechanical behaviour of high-deformable materials, such as mastics and ICs. Before starting to deeply explain the measurement system, it is worth to highlight that the proposed analysis involved only the mastic phase. Moreover, the measurement system calibration is based on the analysis of the NL material.

As widely discussed by Romeo [112], the DIC technique allows to evaluate the deformation field on the specimen surface without defining the area of interest before testing. Thus, it avoids to analyse localised information about the strain accumulation. Nevertheless, several problems, such as the rotation of the specimen during the test, the out of plane problems, changing in exposure time, roughness of the selected area, are linked to the DIC technique [13].

In order to avoid the mentioned problems, it was decided to study a proper fixing device able to look both rotation and translation of the specimen. Much more specification will be given in the following paragraphs.

In this study two different image-based acquisition systems were used: the digital image correlation (DIC) and a motion tracking procedure. The first one is based on a least-square fitting procedures of the images involved in the analysis, while the second one is based on tracking selected markers on the reference image. For both, the equipment used was composed by a 15W RGB LED system, a camera (aCA 2040-90 μm), and a pc.

The image analysis was performed using a proper designed software made at the University of Parma named DICe, while the motion tracking was carry out using an open

source software (Blender[1]) typically employed in the 3D video editing.

Using the definition given before, the DIC results have to be interpreted as the results of a digital strain gauges, while the motion tracking, in this study, simulates the LVDT system. The first one was used to analyse were the deformation is located on the specimen area, while the other one was used to measure the displacement during the test. The differences, in terms of results, are shown in Figure 4.6.

As noticeable, there are not consistent differences in between the two technologies (±4.57% weighted on the DIC measurement). For that reason during the tests both the measuring methods were employed. The ANOVA box-plot, obtained performing the framework explained above, show that the measurements made using the motion tracking fall in the 95% CI of the DIC measurements (Figure 4.6). This confirms that the differences between the used measurement systems are not significant. The results were obtained analysing 20 observation for each measuring system.

The sample preparation was done following five steps:

- The pre-heating operation of both the asphalt binder used (N) and the filler (L). The first one was placed in a draft oven at equiviscous temperature (160°C) up to becoming fluid (about 1 hour), while the filler needed to be recovered for 4 hours at mixing temperature 160°C to avoid the moisture damage of the mastic [127].

- The pre-heated asphalt binder was placed in a heated 500-ml pot. Successively, the filler was gradually added in the 500-ml pot, and mixed with asphalt binder by a

[1] Blender webpage updated in November 2020.

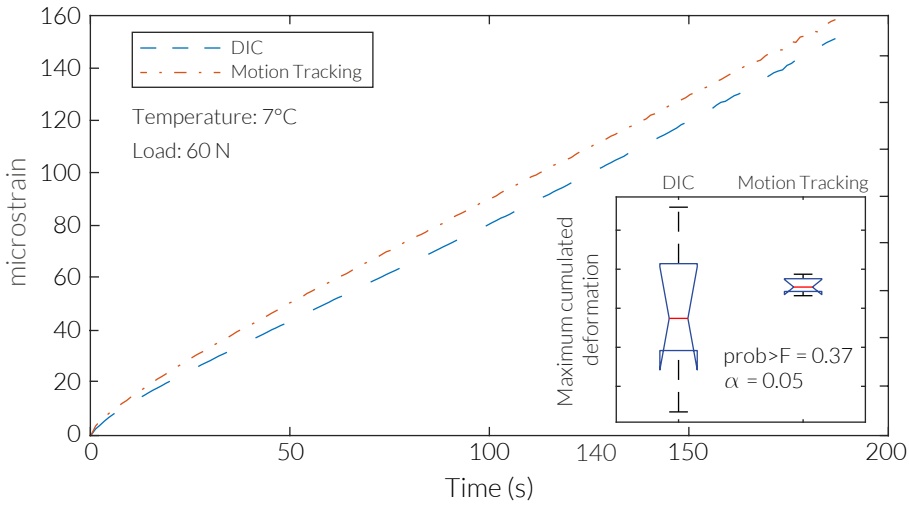

Figure 4.6 Comparison between the DIC and Motion Tracking system showing both the deformation curves and the ANOVA box-plot.

semi-mechanical procedure (it will be discussed further in the dissertation §4.3.1) to obtain the mastic.

- The mastic was then poured in the dog-bone shaped moulds, and allowed to cool down at room temperature for at least 12 hours.

- The application of the white-speckled pattern [12, 13, 40] across the middle of the dog-bone shaped specimens, while the motion tracking markers were placed along the vertical axes (parallel to the load direction). Much more information are discussed in §4.3.5.

- The speckled specimens were successively placed in the testing machine climatic chamber at 7 °C (the testing temperature will be further introduced at §4.3.5) at least for 4 hours (the conditioning time will be discussed at §4.3.2).

The proper distance from the centre to the single marker position was carried out using the DIC strain field. The borders of the strain accumulating area where then used as target of the tracking markers. The position of the target was established to be equal to 1 cm above and below the middle section of specimens, as shown Figure 4.7.

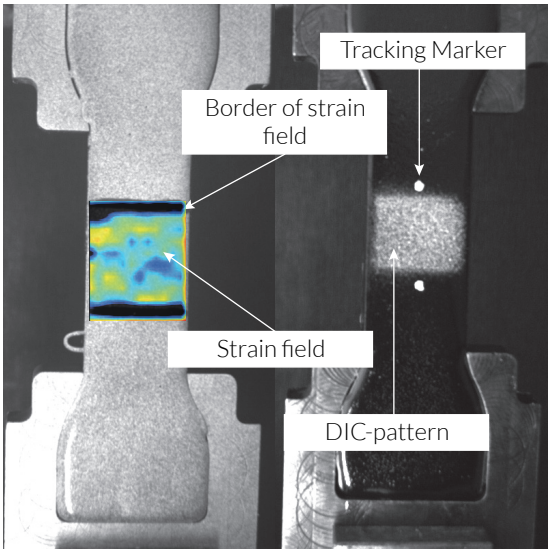

Figure 4.7 Definition marker position using the strain field obtained using the DIC technique. On the left, the specimen analysed using the DIC showing the accumulation of the strain in the middle section of the specimen [12]. On the right, the configuration used during the tensile creep analysis.

4.3. Preliminary analysis and parameters definition

As widely explained above, this research project aims to better understand the aptitude of mastics to accumulate permanent deformation (creep behaviour). As for the measurement system, it is worth to highlight that the proposed analysis involved only the mastic phase. Moreover, the whole preliminary analysis is based on testing the NL material.

In order to better understand the phenomena, it was decided to deeply analyse different variables such as testing machines, storage periods, mixing procedures, loading time, and etc..

Figure 4.8 shows the experimental program used for defining the parameters considered. The main assumption for the overall testing campaign is: performing the test in the linear viscoelastic (LVE) range of the mastic material. In order to accomplish it, as explained in the following paragraphs, the testing temperature was identified considering a wide range from 5 to 10°C, at which the HMA behaves in visco-elastic conditions. Moreover, the cross-section was continuously monitored to guarantee the proper stress distribution and to keep it constant without significant changes with time. In order to better understand the proposed analysis, both the specimen preparation and storage procedures were firstly introduced.

4.3.1. Mixing procedure of mastic specimens

Defining the best preparation method of the samples is important because the homogeneity of the material is fundamental for obtaining good stress and strain distribution during tests. For this reason two different procedures, hand [12, 25, 129] and semi-mechanical mixing (based on the procedure suggested by Gundla and Underwood [83]), were considered.

For both the mixing procedures considered, fillers were heated for 4 hours, while asphalt binders were placed into the oven until they become fluid (about 1 hour). The equiviscous temperature of the asphalt binder used are 160°C and 170°C, for neat and SBS modified binders, respectively. Thus, they were selected as mixing temperatures. During the mixing operation, the temperature was kept by using a calibrated heater plate, and the materials were mixed into a 500-ml pot.

Mixing was performed by using the high shear mixer Silverson L5M-A (max power 750 W), able to achieve 7000 rpm, for the semi-mechanical procedure, while for the other one a rigid-spoon was used.

The semi-mechanical mixing establishes to firstly place the asphalt binder into the small pot. Consequently, the amount of filler is added into the pot, and roughly mixed by using a spoon (few seconds). When the filler is fully absorbed by the asphalt binder, a 90 s mixing time at maximum speed was selected [83] on the Silverson L5M-A.

The hand procedure is fundamentally based on adding the filler into the pot containing the asphalt binder, which is contemporarily stirred [12, 25, 129]. The material

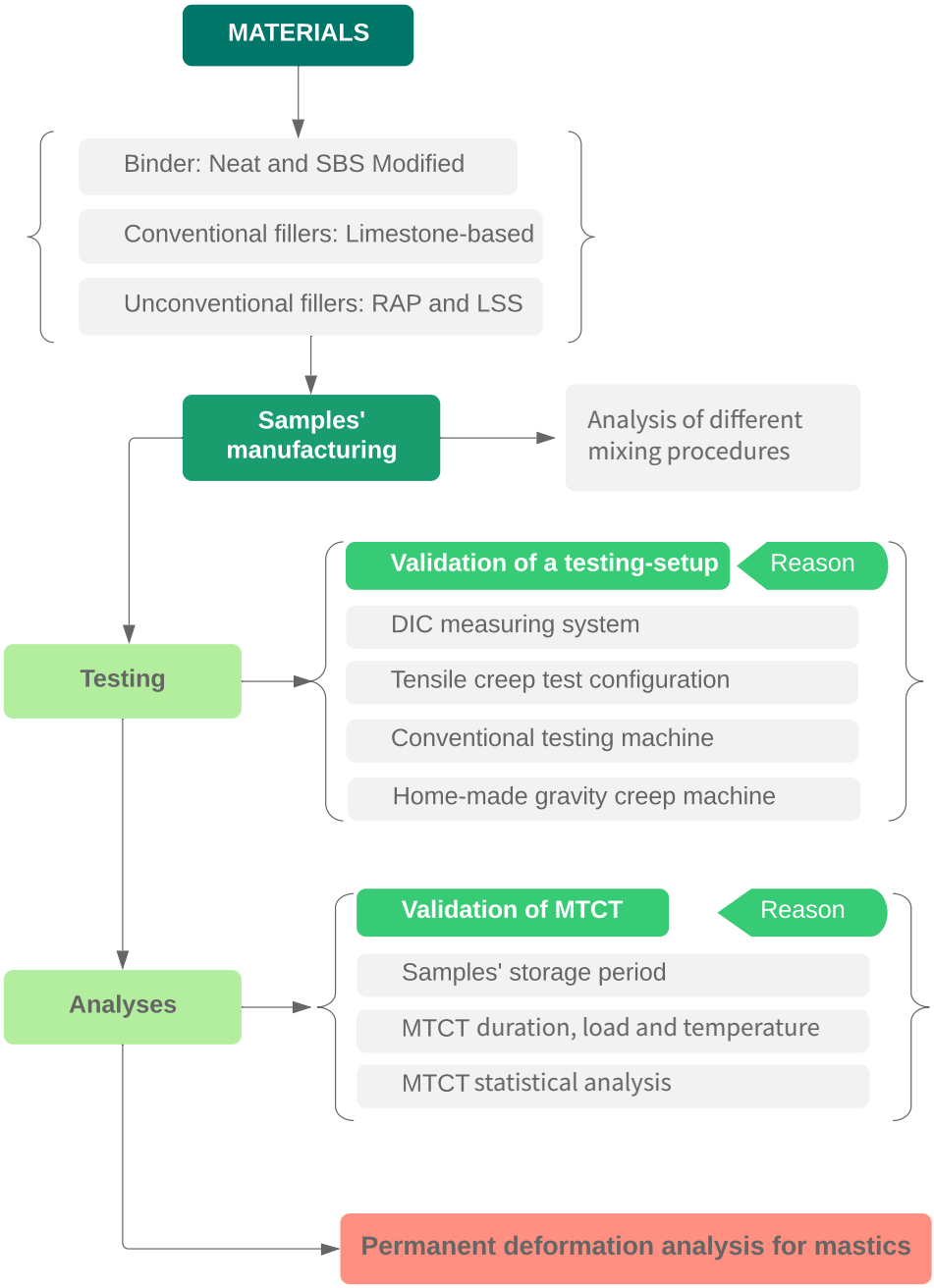

Figure 4.8 Flowchart of the experimental approach.

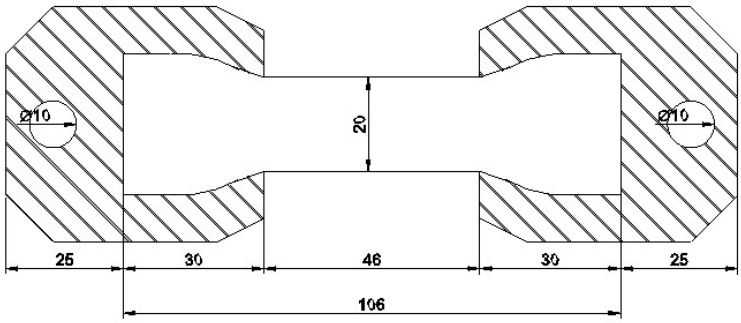

Figure 4.9 Dog bone shaped sample geometry [12], which is 10 mm thick.

obtained was poured into proper dog-bone shaped moulds [12] (Figure 4.9), and, in order to keep the material fluid enough during the pouring operation, mastic samples were manufactured 5 at a time mixing 210 g of fillers with 140 g of asphalt binder. The amount of materials to mix is based on obtaining the same filler/bitumen (F/B) ratio of the HMA used as references (§3.3.3), which was obtained by a SuperPave volumetric approach [111]. Therefore, the F/B ratio used is equal to 1.5.

Successively, samples were allowed to cooling at least 4 hours before placing them into a cabinet set at 7°C for 4 hours before testing.

Figure 4.10 shows the results obtained by performing the new tension test, using the gravity machine described into §4.3.4 (loading 60 N), and by running the statistical approach shown into §4.1.

By analysing the Figure 4.10a is possible to recognise that the semi-mechanical approach guarantees more precision (small error bar length) if compared to the hand procedure. This trend is also confirmed by the m-value results (Fig. 4.10b).

Figure 4.10c shows how the materials accumulate the deformation. The analysis of the strain curves and their range of error, it is possible to better understand the accuracy and the reproducibility of the semi-mechanical procedure. In fact, the error range of the measurements, which is represented by the orange (semi-mechanical) and blue (hand mixing) areas, is really close for the semi-mechanical case. For that reason, the adopted mixing procedure was the semi-mechanical one.

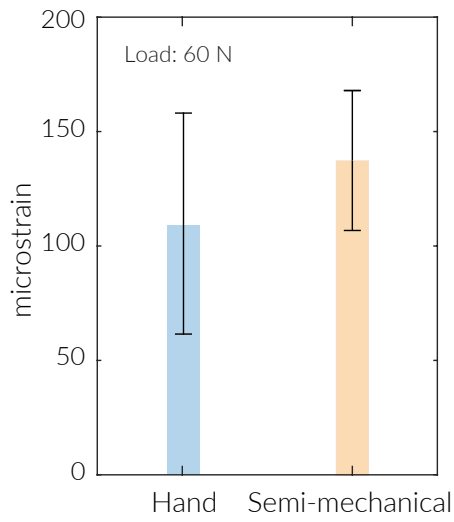

(a) *Maximum deformation.*

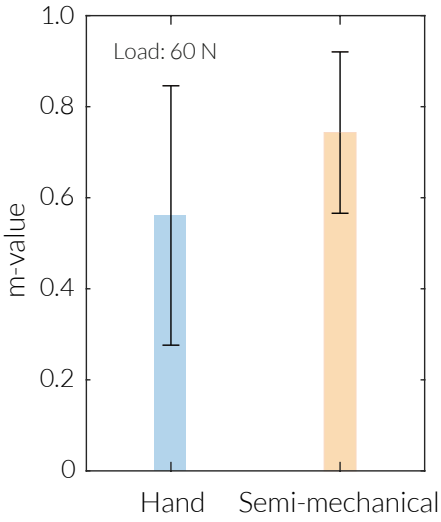

(b) *m-value.*

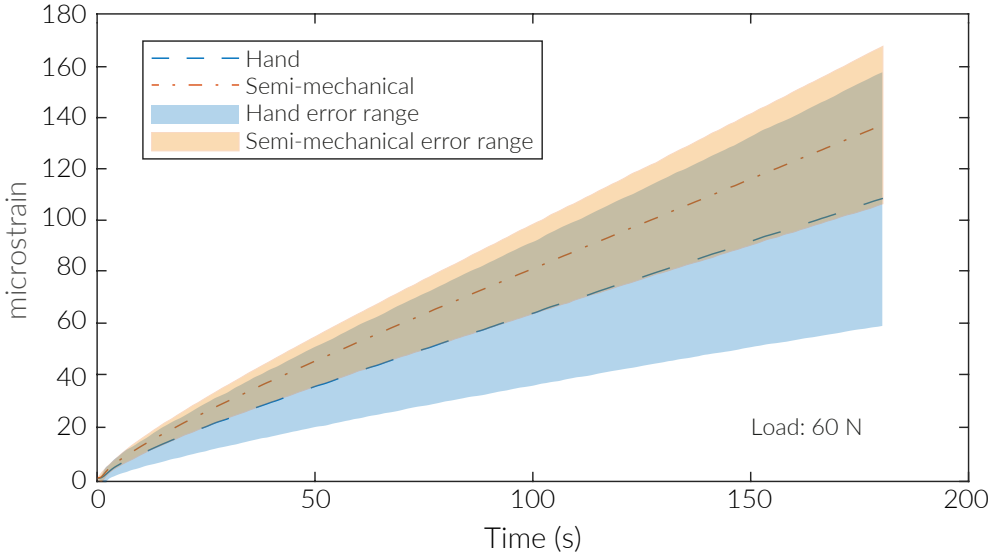

(c) *Deformation curves with measuring error.*

Figure 4.10 Comparison between hand and semi-mechanical mixing methods at 7°C.

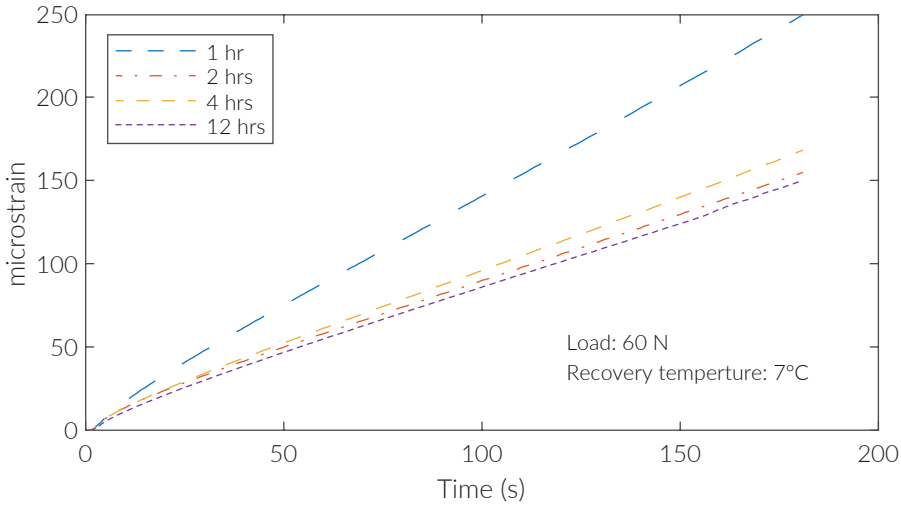

Figure 4.11 Comparison between different storage-periods.

4.3.2. Storage period

After defining the proper mixing procedure, the attention was moved on the storage period. This variable is important because the materials, which are not properly recovered and conditioned, can behave differently during tests.

The approach used in this phase is not based on measurements of thermal properties of the analysed material, but it is based on empirical observation.

As described above (§4.3.1), after the mixing procedure the obtained samples need to be recovered for achieving the selected testing temperature. This analysis was done considering the four different recovery periods: 1, 2, 4, and 12 hours. 10 samples for each period were placed into a cabinet set at 7°C. After the conditioning period, the samples were tested by using the gravity machine (it is explained in the following paragraph), applying 60 N at 7 °C.

Figure 4.11 shows the results of the tensile tests. Its analysis clearly highlights that the materials need at least 2 hours for achieving the desired temperature. The reported curves also show that the analysed material behaves similarly after 2, 4, and 12 hours. Considering the reported results, 4 hours represent the best recovery time before testing the specimens.

The ANOVA analysis (Figure 4.12) of the collected results shows that a storage time of 1 hour gives back a not consistent series of data, if compared to the others, as shown in (Figure 4.12a). By focussing on the maximum deformation achieved at the end of the test, a multi comparative analysis was proposed. This comparison was made using the *multicompare* Matlab function. This methodology is based on the Tukey's Honestly Significant Difference Procedure. This method is able to compare the mean of the ANOVA

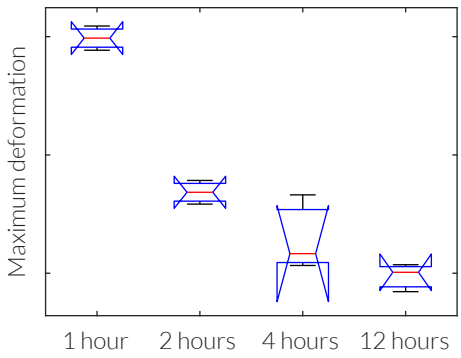

(a) *Box-plot.*

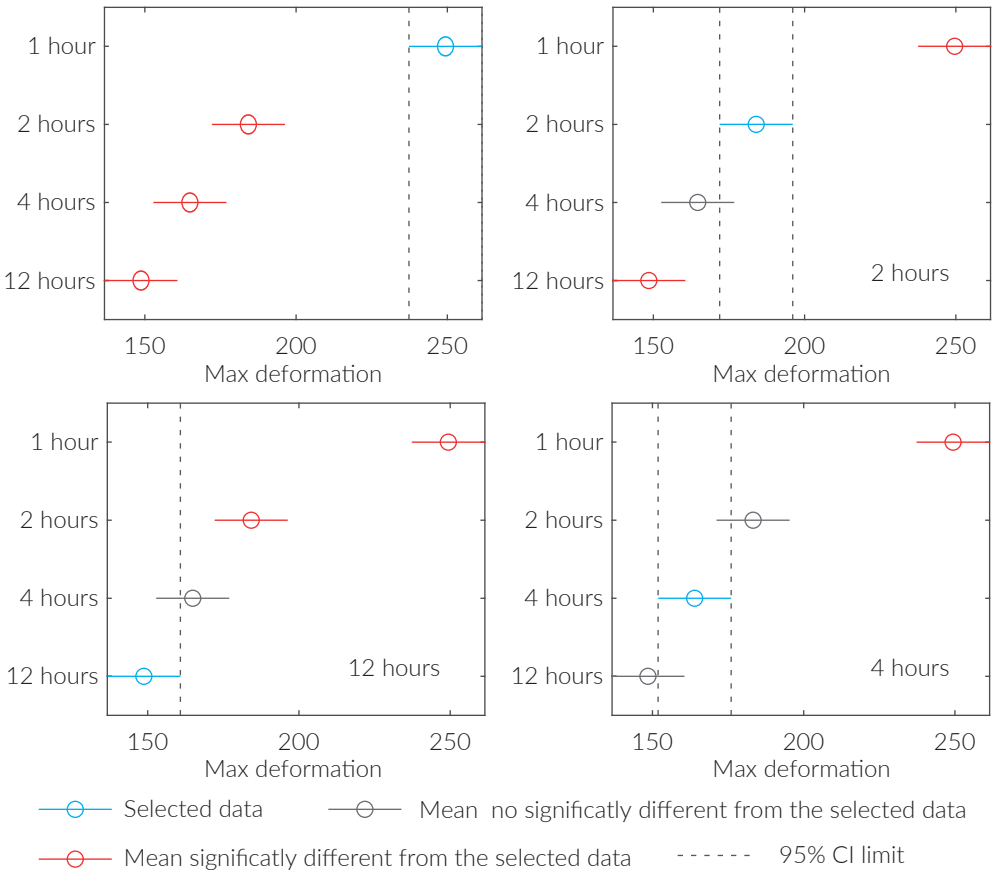

(b) *Multicompare box.*

Figure 4.12 ANOVA analysis (95% CI) showing the box plot of the maximum deformation at the end of the test ***(a)***, and the multicomapare box which highlights the significant difference between the considered period ***(b)***.

analysed data understanding what treatment differs from the others.

The results of the analysis were reported in Figure 4.12b. This methodology confirmed that the results of the 1 hour storage period are not consistent. Moreover, significant differences between the 2 hours and 12 hours of recovery time (Figure 4.12b) were also highlighted. Thus, it means that after 2 hours the thermal steady state condition was not guaranteed. This equilibrium is achieved after 4 hours as showed in Figure 4.12b. Consequently, this duration was selected to be the proper storage period before testing the recovered samples.

4.3.3. Mastic sample preparation

The mix design of the mastics started by selecting the proper bitumen-filler (B/F) ratio which is linked to HMA B/F ratio obtained through a volumetric mix design. In this study, the targeted B/F was 40/60 for both the used bitumens.

The considered phase, which did not involve using RAP, were obtained just changing the type of filler, while, the material containing RAP were prepared considering the RVB% and WCO% described in §3.3.2.

Before mixing, the used fillers were placed in a draft-oven, which was pre-heated at the bitumen equiviscous temperatures, 170 °C (SBS modified bitumen) and 160 °C (Neat bitumen), at least for four hours. The bitumen was also recovered in the oven up to becoming fluid (about 1 hour).

Successively, the materials were placed in the pre-heated pot and mixed using the mechanical mixer Silverson L5M-A. As explained above (§4.3.1), the mixing operation was divided in two steps. During the first one the material is roughly mixed, while during the other it is full mixed at 6000 rmp for 90 seconds. The number of rpm was selected to avoid air-bubbles development on the specimen surface (§4.2). On the other hand, mastics were poured in the dog-bone shaped moulds, which were allowed to cool down for at least 12 hours, and consequently placed in the climate chamber for 4 hours before testing (§4.3.2).

After cooling, the motion tracking markers and the DIC pattern were placed, and the samples were recovered for 4 hours at the testing temperature. For each investigated materials 10 specimens were prepared and tested.

4.3.4. Testing machines

The testing machine commonly used for the mechanical characterization of asphalt materials can be distinguished into two categories: servo-hydraulic and -electric. In this study, the used machine is a servo-hydraulic one equipped with a load cell of 25 kN.

The preliminary analysis was focussed on establish whether the testing machine is able to correctly perform the required loading condition (from 30 to 200 N) or not. This phase was developed by considering the NL (defined in Chapter 2 §2.3), and a 60-second-duration for the load application. The preparation of the samples was done by following

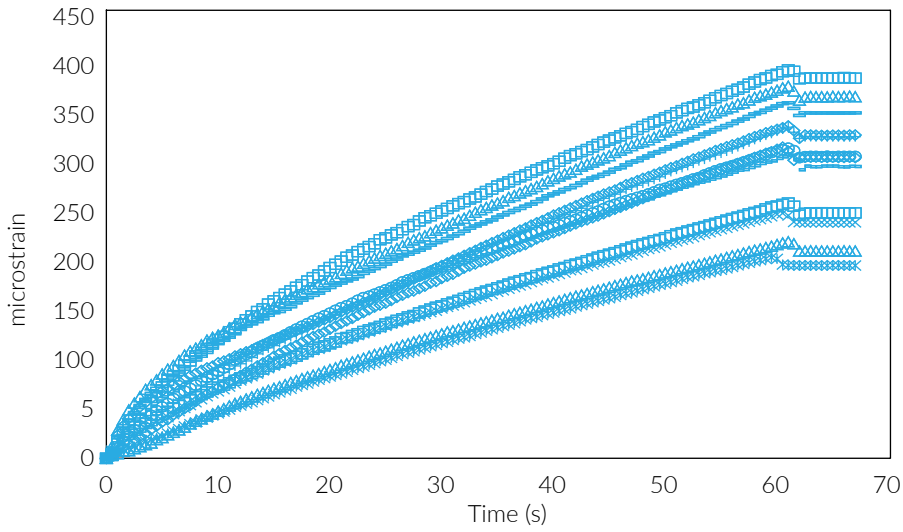

Figure 4.13 Example of results at 100 N obtained by using the servo-hydraulic system and testing the NL mastic.

the procedure showed above.

As it is possible to recognise in Figure 4.13, the results obtained for the same material are not consistent due to the huge dispersion of results. In fact, the curves shown are significantly different. Analysing step by step the operation mode of the testing machine used, the dispersion of the data is linked to the fluctuation of the pressure into the hydraulic system due to the pump operation.

In order to solve this problem, a gravity machine system was designed, considering the axial and bending resistances which are standardised by the EN 1993-1-1:2014 [143], and developed.

The machine is composed by a linear motion system, a traction system, and 2 steel bases, as shown in Figure 4.14. Much more draws are reported into the Appendix B.

The linear motion system (LMS) is composed by 2 steel columns, an aluminium crossbeam, and, in order to ensure low friction between crossbeam and columns, 2 ball bushing (Fig. 4.14). The LMS was designed up to 800 N, considering the gravity acceleration equal to 9,80427 m/s^2(referred to Parma).

Loading is performed by hanging calibrated weights to the crossbeam, which is able to move along the 2 columns (the vertical axes). Consequently, the LMS was screwed to both the steel bases by inserting it into ad-hoc-designed supports (2 for each column), as shown in Figure 4.14.

After assembling the LMS, one of the specimen handles was screwed to the crossbeam, while the other one was fixed to the upper base, as shown in Figure 4.14. Both of the screwed handles are characterised by 10.05-mm-diameter-holes (Fig. 4.14), thereby

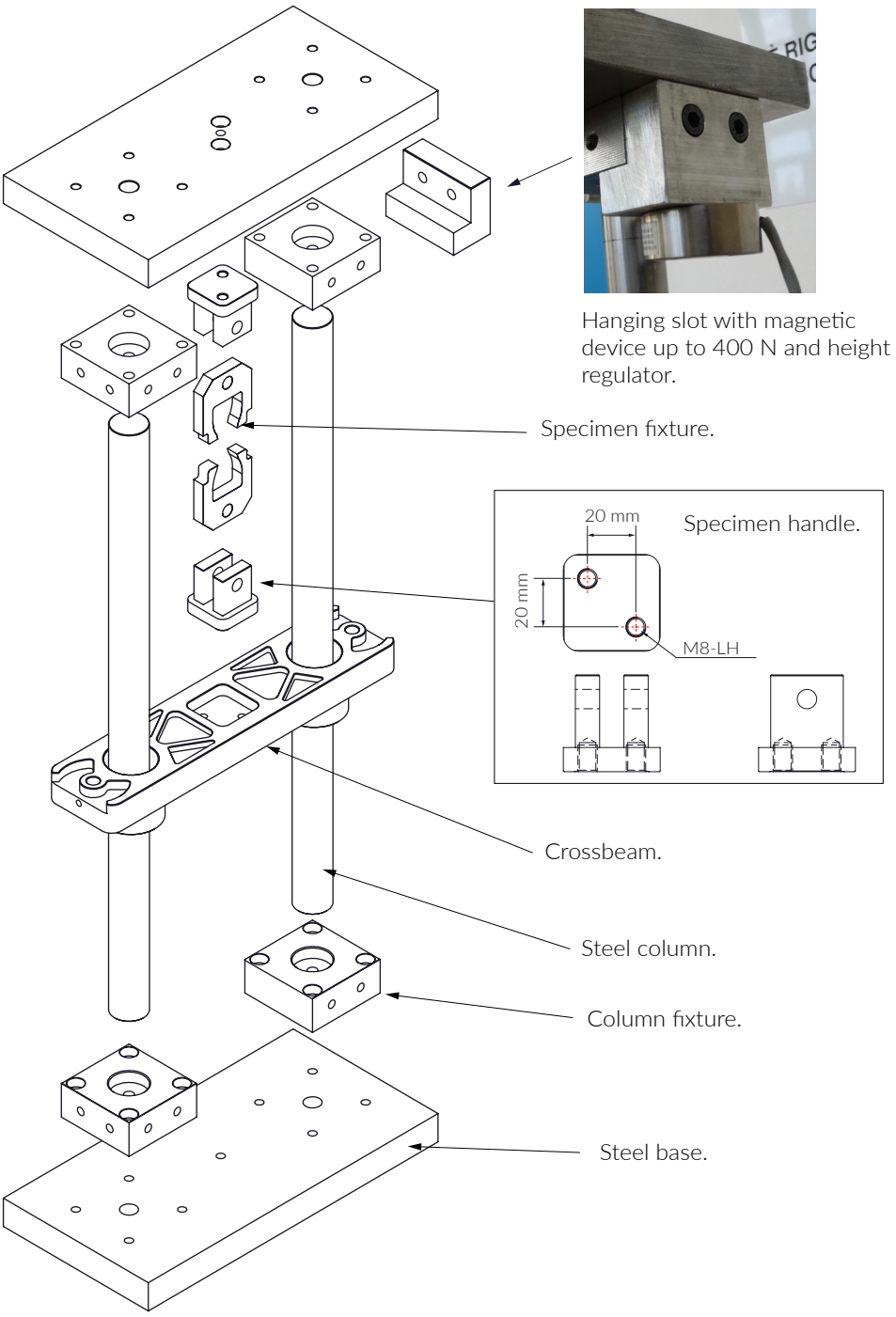

Figure 4.14 Exploded-view drawing of the tensile machine with construction details.

specimen fixtures can be vertically blocked by using linchpins, defining the traction system (TS). Consequently, the specimen is locked avoiding the problems described and discussed by Birgisson et al. [13], such as the rotation of the specimen during the test, the out of plane problems, changing in exposure time, roughness of the selected area.

A magnetic device, which is able to hang up to 400 N, was used to keep the right position before testing. Therefore, the TS was consequently connected to the hanging slot through a steel connector.

As it is well known, creep tests are performed in load control mode. Therefore the TS's weight was calibrated at 20 N, by lightening the crossbeam through both triangular and circular holes (Fig. 4.14), and also adjusting the connector weight.

For increasing the repeatability of tests, the tensile machine and cameras for both DIC and motion tracking were synchronized. This problem was solved by developing an in-house LabVIEW software, called gravity machine controller (GMC), able to trigger the cameras and to manage the machine by sending analog signals up to 10 Volts.

The control system is connected to a power relay and timer board, which can receive analog signals. Thus, when the input is received, the timer starts a countdown (5 minutes), allowing to recover the testing temperature. At the end of the countdown, the power relay switches off the magnetic hanging device, and, consequently, the test starts and also the trigger signal is sent to the camera starting the image acquisition.

4.3.5. Loading, duration and testing temperature

The calibration of the testing duration was firstly defined to identify the linear range of the creep behaviour. The analysis was performed using 10 samples (prepared with neat bitumen and limestone), 60 N as testing load, and 900 seconds as test duration.

The samples were prepared using the mix procedure explained in §4.3.1. After mixing, when the material has achieved the room temperature, the speckled-pattern was applied to the whole surface of the samples, and the motion tracking markers were place on the vertical axes, as discussed in §4.2.

The results obtained using the DIC technique differed from the data carried out by performing the motion tracking. The errors were linked to a significant change of the sample-light-exposure, as shown in Figure 4.15a. This problem was recognised just for the DIC results because the motion tracking software allows to normalise the exposure to the first frame of the dataset used as reference image. The exposure problems were observed after 180 seconds. Thus, this was used as reference time for testing mastic samples. These problems were partially due to either the light position or the speckled pattern which increase the brightness of pictures. Moreover, another criticism linked to the light exposure was the presence of micro-air-bubble holes on the surface of the specimens (Figure 4.15a). These holes were basically due to the air entrapped during the mixing operation. This criticism appeared after 450 seconds. This causes a roughness problem as widely described by Birgisson et al. [13],and [112]. This confirmed that the motion

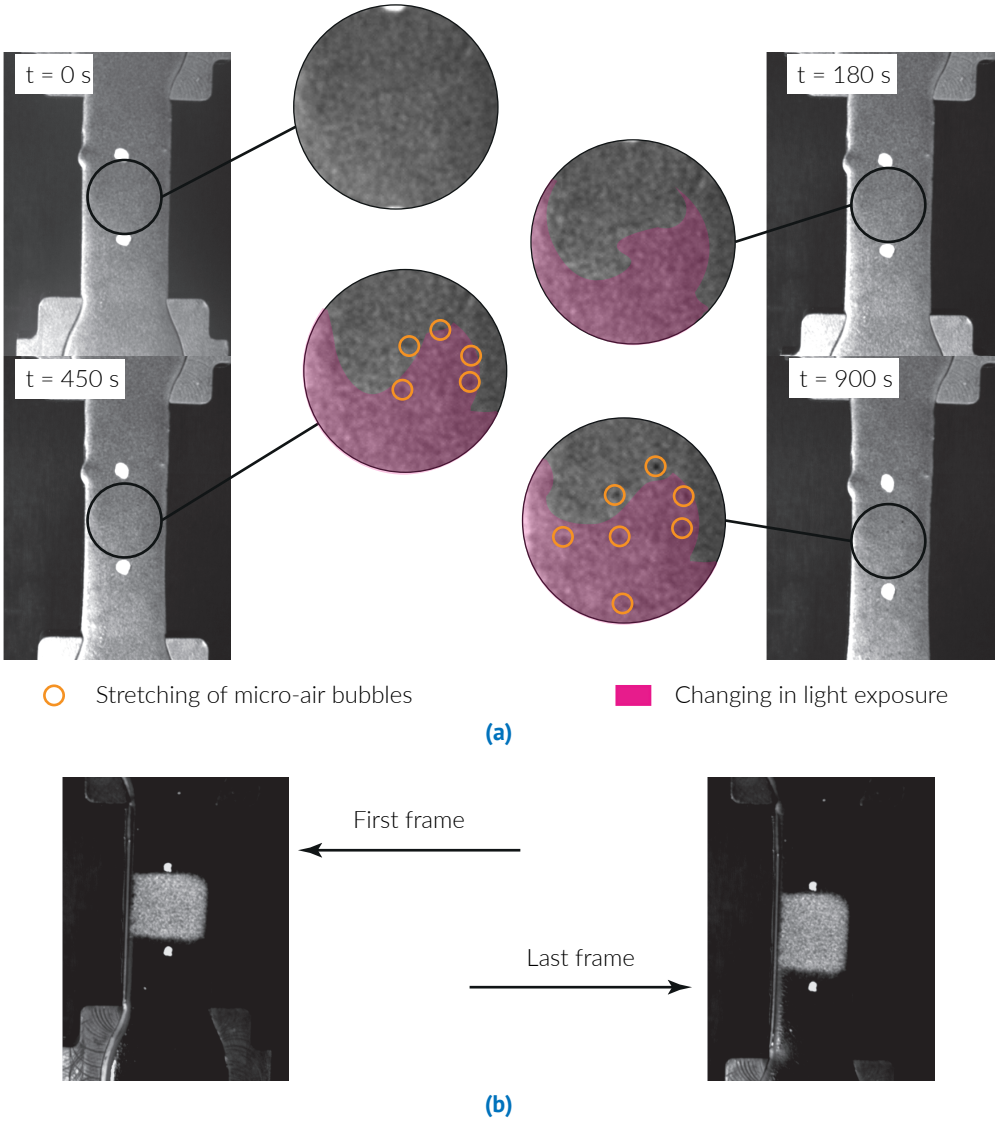

Figure 4.15 ***(a)*** Changing in light exposure during the test which compromise the DIC results [13]. The appearance of holes due to the extension of the micro-air bubbles which are on the specimen surface . ***(b)*** Final DIC and motion tracking markers set up. The configuration allows to avoid changing in light exposure.

tracking measuring system is distinguished by a lower light exposure susceptibility than the DIC one. For that reason both were used during the tests.

Considering the 180-second-duration, the speckled-DIC-pattern was corrected and the final solution is shown in Figure 4.15b. The final set up was selected to reduce the

light differences among the initial frame and the others. Figure 4.15b shows the reduced brightness problem between the first and the last frames of a tested sample.

Successively, after defining the duration of the test (180 s) and the DIC pattern size, the attention was focussed on defining the load to apply. This analysis involved four different loads (40, 60, 80, and 100 N), and 10 samples for each load made with neat bitumen and limestone. The analysed specimens were tested a 7 °C, which was a trial temperature chosen to be in the LVE region of the material. This analysis was carried out considering the creep compliance (J_{MTCT}), the accumulation rate of the deformation (*m-value*), and the deformation curves (Figure 4.16).

The *m-value* and the deformation curve were obtained by fitting the measured $\varepsilon(t)$. Their computation was done using the Power model ($D(t) = D_0 + D_1 t^m$), as already discussed in the §4.1.1. The J_{MTCT} parameter is defined as the creep strain per unit of applied stress calculated at 180 s. It is calculated as follow:

$$J_{MTCT} = \frac{\varepsilon_{180}}{\sigma} \tag{4.25}$$

where ε_{180} is the measured strain output at 180 s, $\sigma = P/A$ is the stress due to the applied load P, and $A = 200\ mm^2$ is the cross section area of the specimens.

Starting from the analysis of the deformation curves (Figure 4.16c), which describes the accumulation trend of the deformation, and considering that the creep is a slow continuous deformation of a material under a constant stress, it is quite clear that if the material is tested using 100 N the creep period is really short.

In terms of J_{MTCT} (Figure 4.16a), the 100 N load was not able to guarantee good accuracy. In fact, the error-bar for the load was quite wide. Thus, 100 N was not considered as correct load for this application. Referring to 80 N load, the deformation respects the expected trend (linear at least up to 180 s) (Figure 4.16c), while, in terms of J_{MTCT}, the data exhibited a wide error-bar highlighting a low precision and accuracy (Figure 4.16a). The same results were carried out also for the 40 N load. Consequently, 40 N and 80 N were not employed as testing load. Conversely, the 60 N load exhibited high J_{MTCT} accuracy (Figure 4.16a). Furthermore, the deformation trend follows the expected one (Figure 4.16c). Consequently, it was selected as proper load for the mastic investigation.

In terms of *m-value*, the analysed samples showed high accuracy level (Figure 4.16b). This could likely mean that when the load is lower than a certain value (in this case 60 N), the deformation of the material can be considered slow enough to follow the creep definition for linear materials which implies keeping the cross-section constant without significant changes with time [10] (no necking phenomenon). Vice versa, when the load is over the selected threshold, the strain-rate of the material is higher (100 N and 80 N), thus the necking phenomenon rapidly appears generating instability in the sample structure.

Consequently, as anticipated above, the cross-section was monitored measuring both

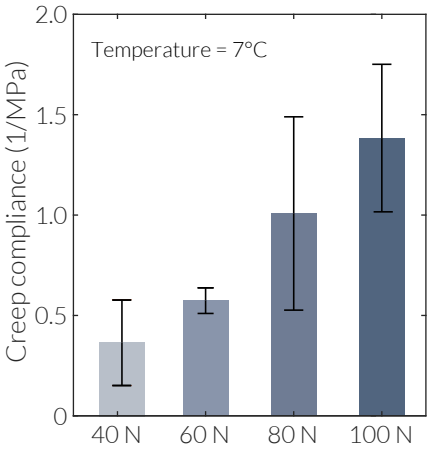

(a) *Creep compliance at 180 s.*

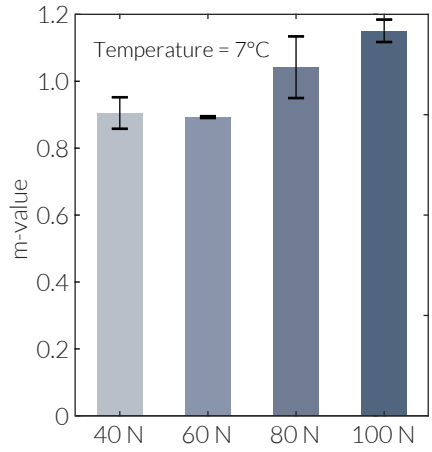

(b) *m-value.*

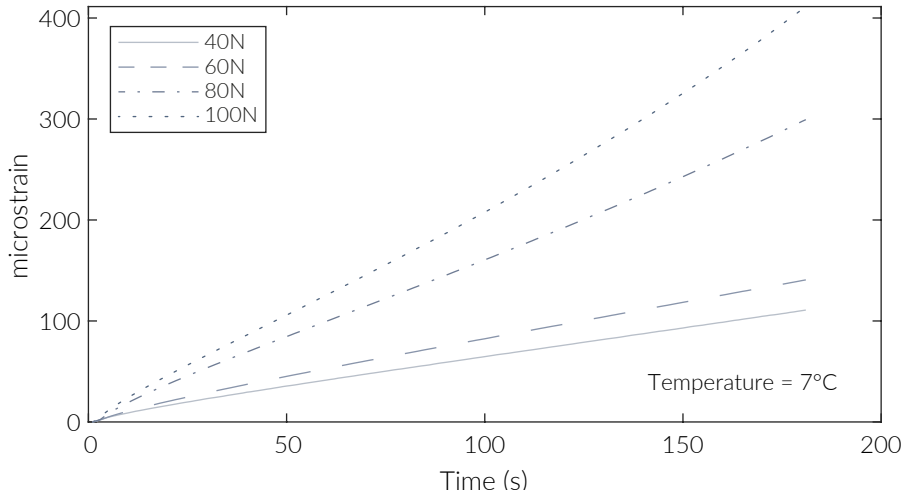

(c) *Deformation curves.*

Figure 4.16 Comparison between different loads.

the $\varepsilon_x(t)$ and $\varepsilon_y(t)$, which represent the deformation along the *x-axis* and *y-axis*, respectively. Particularly, their ratio (*X/Y* ratio) was analysed.

As shown in Figure 4.17a, the X/Y ratio slowly decreases which means that the higher the $\varepsilon_y(t)$, the lower the $\varepsilon_x(t)$. This can be interpreted as a slow necking rate. This trend is kept over the selected duration indicating that the 60 N load is able to keep the right structure of the sample.

Comparing Figure 4.17b and Figure 4.17a, important constrains can be recognised to validate the test. Focussing on the first 30 s of the test is possible to notice that the X/Y

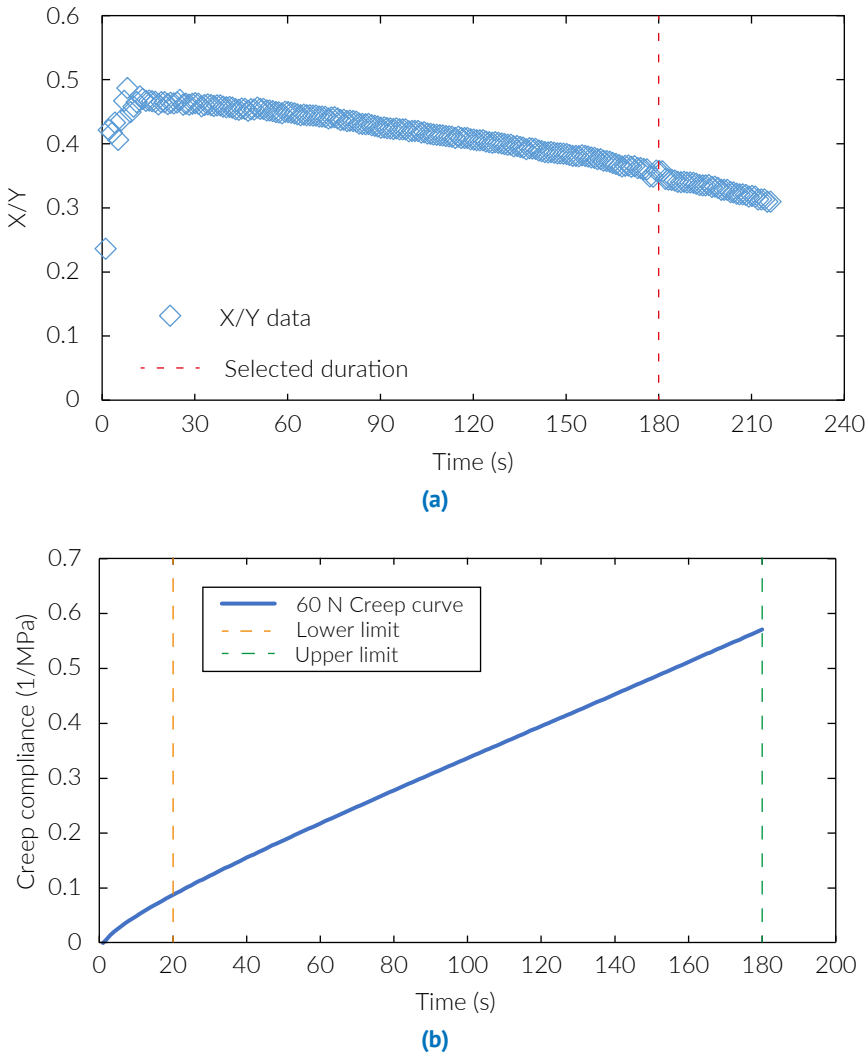

Figure 4.17 ***(a)*** X/Y ratio trend during the test performed applying 60 N at 7 °C. ***(b)*** Obtained 60 N creep curve showing the lower limit (20 s) and the upper limit (180 s).

ratio increases up to about 15 seconds, and, successively slowly decreases. This would indicate that the primary creep [10] finishes after few seconds. Therefore, it has been assumed that the analysed material must exhibit a linear trend after 20 s and J_{MTCT} has to be lower than 0.1 MPa^{-1}. The *J_{MTCT}-constrain is linked to the definition of the linear materials which requires the small-strain domain, indicating that if the J_{MTCT} is higher than the 0.1 MPa^{-1}, the load must be decreased because the measurement is over the small-strain domain.* Moreover, in between both the limits, the creep-curve have to be linear.

In order to properly define the testing temperature, the behaviour of the material

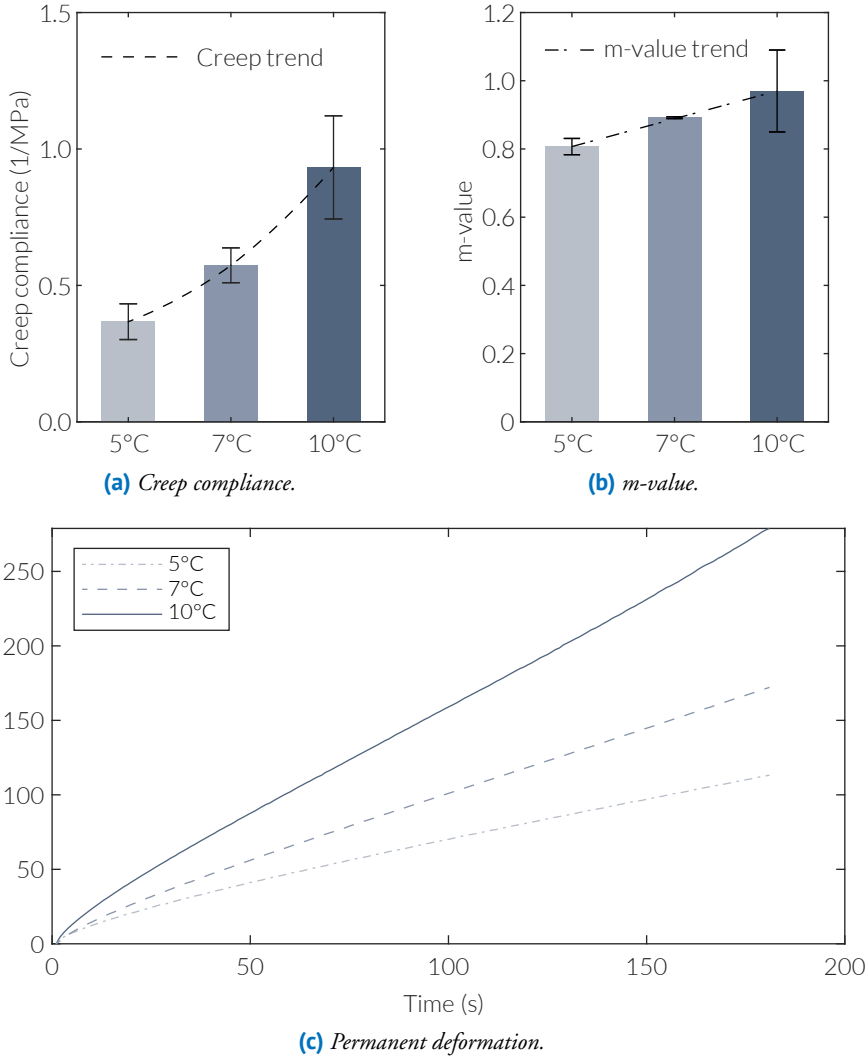

(a) *Creep compliance.* **(b)** *m-value.*

(c) *Permanent deformation.*

Figure 4.18 Comparison among three different temperatures based on the analysis of the J_{MTCT} ***(a)***, m-value ***(b)***, and the permanent deformation trend ***(c)***.

was analysed at three different temperatures considering the already discussed 60 N load. Therefore, 5 , 7 and 10 °C were considered, as shown in Figure 4.18. The choice of the three temperatures was linked to respect the LVE range to compare the data with the HMA fracture mechanic framework collected data, as mentioned above.

As noticeable in Figure 4.18a, the creep compliance was distinguished by a not linear trend. Conversely, the m-value trend is linear, as shown in Figure 4.18b. This means that the higher is temperature, the higher is the cumulated deformation. However, the strain

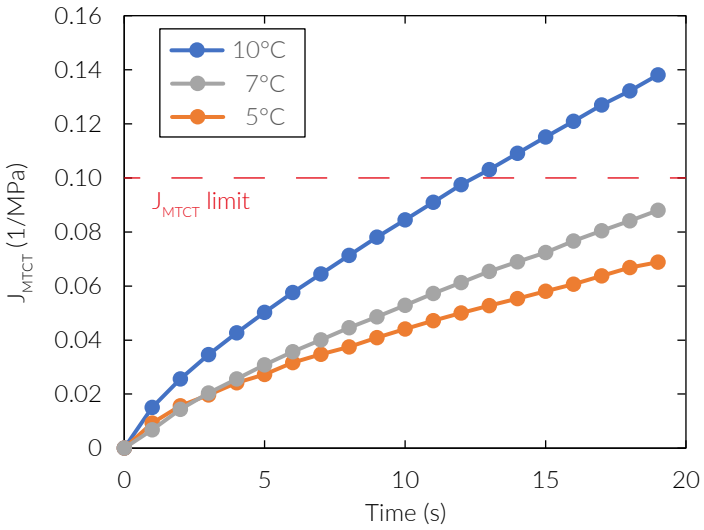

Figure 4.19 Comparison among the three different involved temperatures in terms of J_{MTCT} up to the defined lower limit of the proposed test (20 seconds).

accumulation rate does not highly differ considering the three used temperatures.

Therefore, the differences among the analysed condition have to be considered in terms of J_{MTCT} up to the defined lower limit of the test (20 seconds). Thus, analysing Figure 4.19 is possible to recognise that the J_{MTCT} at 10°C is higher than the others, as expectable. For that reason, the previously discussed 0.1 MPa^{-1}-limit is not satisfied.

Considering 5°C and 7°C, their $\varepsilon(t)$ are quite similar in the first part highlighting not significant differences (Figure 4.18c). Furthermore, looking at Figure 4.19, the J_{MTCT} values are below the J_{MTCT} limit previously introduced, which allow to stay within the small-strain domain.

After the defined 20-second-limit the material behaviours differ each other, but both the temperatures satisfied both the time limits above discussed (Figure 4.18c). This has given the possibility to use both the condition as testing temperature. Nevertheless, the precision, in terms of m-value, at 7 °C is higher than the measurements made at 5°C (Figure 4.18b). Consequently, the study herein considered 7 °C as suitable temperature for the new testing protocol.

4.4. Testing protocol

The preliminary results discussed above were used to define the new testing procedure for mastics.

Tension-compression tests are able to evaluate both creep compliance and relaxation behaviours. In this study the proposed test is focused on evaluating the strain-rate of

mastics and their creep behaviour.

The proposed test was performed at 7°C by applying a constant load (60 N) for 180 seconds. Usually, the aptitude of asphalt materials to accumulate permanent deformation is described by the maximum deformation (ε_{max}), the *m-value*, and the creep compliance (J_{MTCT}). Whilst, the first one describes the total deformation of specimens, the second one gives back information about the deformation rate. In fact, the higher the m-value, the higher the deformation rate.

In order to increase the accuracy of the measurements, an appropriate tensile machine was designed and developed.

The 7 °C temperature was selected to ensure a LVE response of the mastic. This temperature was calibrated after a high number of trials performed from 10°C (temperature at which the HMA behaves in visco-elastic conditions) up to 5°C. Although the previous direct tensile test (MDTT) Montepara et al. [12] guaranteed a proper behaviour at 10°C, it was observed that the load control test with longer duration allowed the sample to dissipate a certain energy and consequently to warm up during the test, going over the small strain domain loosing the LVE regime.

Before starting to explain and analyse the collected results of the testing campaign, it is worth to show the repeatability of the new testing protocol.

The repeatability was verified using the One-way ANOVA test, as explained in §4.1.2. This test allows to establish whether the measurements of a phenomenon differ or not due to a treatment. In this research activity, the repeatability study was performed considering three different operators (treatments), in order to establish whether the protocol is affected by the operator or not.

The statistical study establishes, for each operator, to perform the testing protocol, from the sample preparation to the sample testing operation. The material selected for the analysis was the combination neat bitumen-limestone filler, considering 20 samples for each operator. This choice was linked to the availability of the materials. Therefore, the three different operators were selected, one standard represented by the author of the study herein, and two randomly selected.

The results of the ANOVA analysis, summarised in the Table 4.1 and Figure 4.20, show that the repeatability of the test is high. This highlights that the testing protocol is not operator sensitive.

Table 4.1 Results of the One-way ANOVA test showing the high repeatability of the test.

Source	SS	df	MS	F	Prob>F
Columns	0.1631	2	0.0815	0.0097	0.9903
Error	478.30	57	8.3912		
Total	478.46	59			

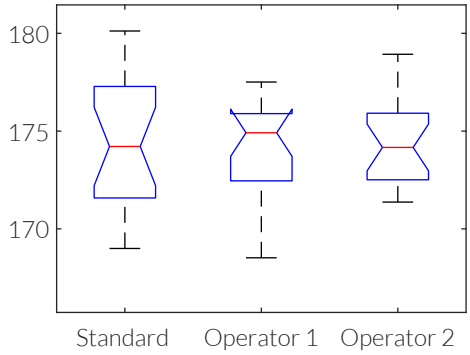

Figure 4.20 Results of the One-way ANOVA test, highlighting the differences in terms of measured maximum deformation

4.5. Results of the new testing protocol

This section aims to explain the results obtained performing the new testing procedure proposed. In order to correctly discuss the obtained results, the collected data for both the analysed phases were discussed separately distinguishing neat- and SBS modified-based materials. The parameters considered were the m-value and J_{MTCT}, which are both related to the ε_{max}.

As mentioned above, the collected results were separately discussed. Figure 4.21 and Figure 4.22 show the obtained results for neat- and SBS modified-based materials, respectively.

The N series analysis, which represents the materials made using neat bitumen, aims at explaining the differences, in terms of J_{MTCT}, among materials made with the reused fillers (NSH, NSNH, NR20, and NR50) and materials prepared with conventional fillers (NA,NF, and NL), as shown in Figure 4.21a

Considering the criticisms of using the LFS as filler in HMAs (§2.1), mastics made with LFS showed lower creep compliance, if compared to the other materials (Figure 4.21a). This condition may be due to the fineness of the filler aggregates and their surface area for the LFS, while it is due to the RAb hardness for the materials containing RAP.

Analysing only the NSH and NSNH is possible to notice that this condition is emphasised especially for the hydrated materials (SH).

Focussing on the mastics containing RAP, the NR20 exhibited lower J_{MTCT} than the NR50 (Figure 4.21a). This is likely due to the WCO effects, which was used only for the mixture containing 50% of RAP (NR50).

On the other hand, the materials prepared with the conventional fillers showed quite the same behaviour. However, NF exhibited a J_{MTCT} peak (Figure 4.21a), which could be due to the different chemical reaction occurring between bitumen and hydrated lime. This means that at level of mastic the presence of SSA hydrate lime decrease the inclination

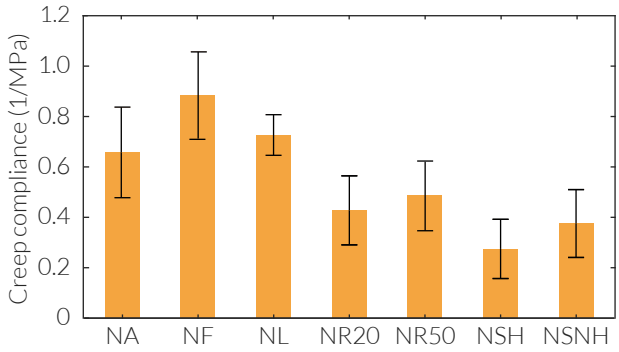

(a) *Creep compliance.*

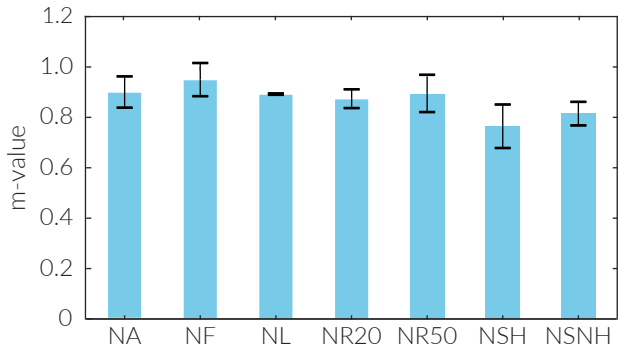

(b) *m-value.*

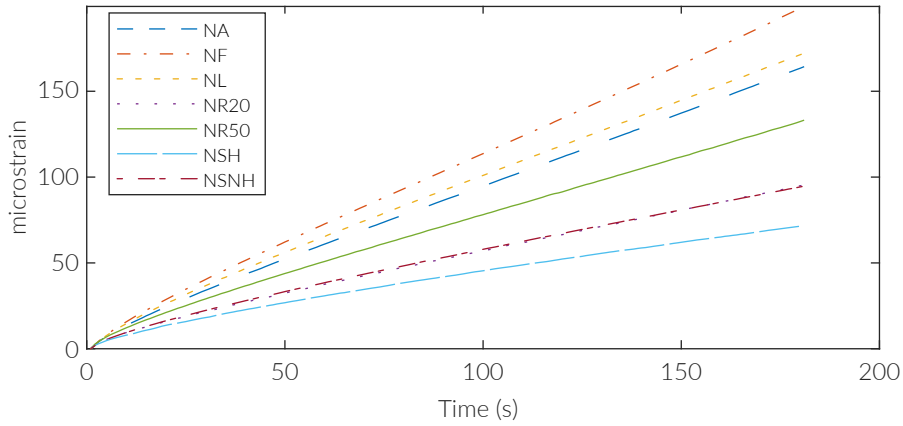

(c) *Deformation curves.*

Figure 4.21 Creep behaviour analysis of the materials made with the neat bitumen.

for accumulating deformation (Figure 4.21a).

In terms of m-value, which describes the aptitude of the materials to accumulate deformation, no significant differences were observed among the analysed materials, as shown in Figure 4.21.

Analysing Figure 4.21c, the permanent deformation trend confirms the analyses done for the m-value and J_{MTCT}. All the analysed materials respected the defined limitation discussed above , showing a linear trend between 20 and 180 seconds (Figure 4.21c).

The analysis of the materials made with SBS modified bitumen was reported in Figure 4.22. Starting from the analysis of the J_{MTCT}, it is possible to notice a reduction of creep values (Figure 4.22a). This may be due to the presence of the SBS polymers into the bitumen, but it is likely due to the different reaction occurring between fillers and SBS modified bitumen.

As expected, the materials containing LFSs exhibited the lower J_{MTCT}, which is quite similar for both MSNH and MSH (Figure 4.22a). MSNHs and MSHs showed the same permanent deformation trend (Figure 4.22c) and accumulation rate (Figure 4.22b). This indicates that the SBS modified bitumen reacts similarly for both hydrated and not hydrated condition.

The MR50 and MR20 confirmed the analysis made above (Figure 4.22b and Figure 4.22c). Therefore, this means that WCO action was only focussed on the re-activation of the RAb at mastic scale.

Conventional materials behaved differently (Figure 4.22a). In fact, the MF J_{MTCT} was lower than the ML and MA ones. Therefore, the cumulated deformation is higher for the A and L materials (Figure 4.22c). Nevertheless, the m-value (Figure 4.22b) highlighted that the accumulation rate is higher for the ML than the MAs and MFs.

4.5.1. Interpretative analysis of bitumen-filler reaction

In order to better understand the bitumen-filler reaction, an interpretative analysis of both the J_{MTCT} and the m-value, based on the filler type, was done, as shown in Figure 4.23. The interpretative analysis proposes to divide the data by the filler type and to compare the SBS modified series with the neat one. Figure 4.23a shows the J_{MTCT} analysis, while Figure 4.23b highlights the differences in terms of m-value.

Considering the conventional fillers is possible to highlight that A and L similarly react with both the used asphalt binders. This confirms the analysis proposed above. Nevertheless, the m-value (Figure 4.23b) is quite similar when the conventional fillers are combined with the neat bitumen. Conversely, it increases when A, F and L are mixed with the SBS modified asphalt binder used. By combining those results, the cumulated deformation is increased by the bitumen-filler reaction (Figure 4.23a). By interpreting the m-value as a damage rate parameter, the bitumen filler reaction and the filler type does not influence the damage rate when the materials are prepared with neat bitumen (Figure 4.23b). While, when the materials are prepared with SBS modified bitumen, the m-value

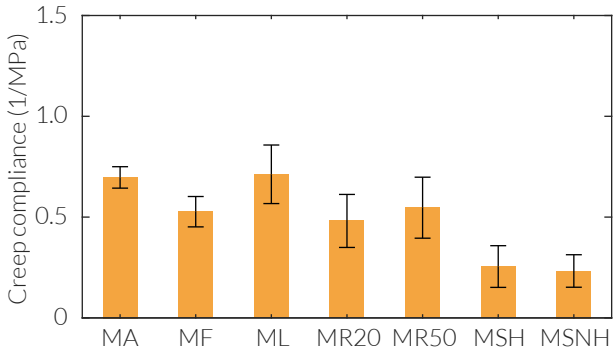

(a) *Creep compliance.*

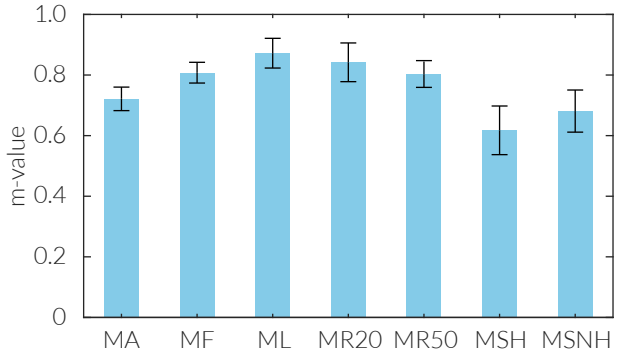

(b) *m-value.*

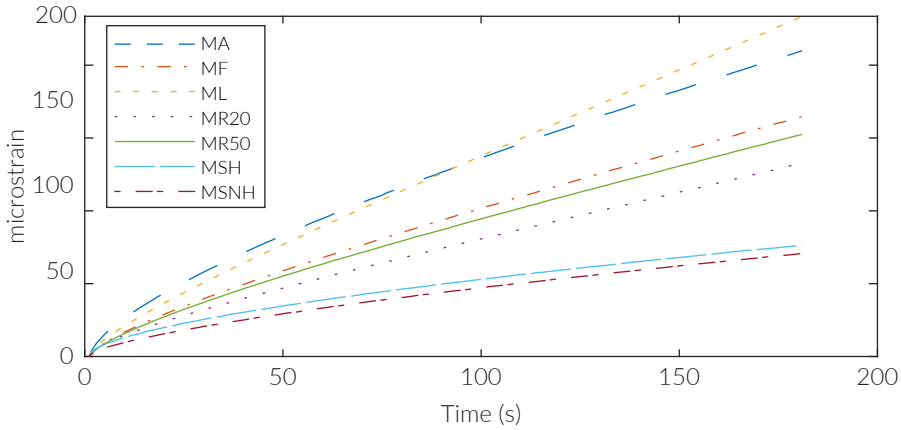

(c) *Deformation curves.*

Figure 4.22 Creep behaviour analysis of the materials made with the SBS modified bitumen.

would seem filler type dependent (Figure 4.23b). In fact, the presence of the hydrated lime and its SSA linearly decrease the damage rate of the materials.

The analysis of the mastics containing reclaimed material appeared not significantly affected by the virgin filler type (L filler in this case) (Figure 4.23) . Conversely, it is affected by the presence of the RAb and WCO. In fact, Considering Figure 4.23a, the creep behaviour of these materials depends on the percentage of RAP introduced as expected. Moreover, the RAb differently reacts with SBS modified bitumen, increasing the cumulated deformation (Figure 4.23a). On the other hand, the damage rate is higher for the neat series. Conversely, the damage rate is lowest for the SBS modified-based material containing 50% of RAP. This aspect can be interpreted as an optimised condition among WCO action, RVB computation, and DoB.

Materials containing LFSs showed quite similar behaviour in terms of J_{MTCT} combined with either neat bitumen or SBS modified bitumen (Figure 4.23a). The huge differences have to be highlighted in terms of damage rate (Figure 4.23b). The m-value also in this case is highly filler dependent. In fact, the hydration process influences, which characterises the physio-chemical structure of the LFSs, the accumulation rate of the mastics (Figure 4.23b).

In order to understand whether the proposed testing procedure is accurate, a statistical analysis was performed following the frameworks described in §4.1.1.

As described above (§4.1.1), the accuracy of the test was evaluated performing the t-test as statistical tool. This test allows to establish if the average of the considered parameter, calculated by using the Power model, is representative of the selected data sample. Particularly, in this study 20 measurements were considered for each material. The p-values referred to both the m-value and the J_{MTCT} are summarised in Table 4.2. The results collected represent the statistical probability to stay in the 95% CI ($\alpha = 0.05$).

Table 4.2 P-value of the t-test performed during the data analysis to evaluate the accuracy of the new testing procedure.

SBS modified bitumen			Neat bitumen		
Label	m-value	J_{MTCT}	Label	m-value	J_{MTCT}
MA	0.979	0.959	*NA*	0.992	0.970
MF	0.963	0.943	*NF*	0.980	0.960
ML	0.961	0.941	*NL*	0.989	0.969
MR20	0.967	0.947	*NR20*	0.974	0.956
MR50	0.986	0.966	*NR50*	0.952	0.974
MSH	0.967	0.979	*NSH*	0.940	0.961
MSNH	0.984	0.989	*NSNH*	0.966	0.979

The analysis of the results Table 4.2 indicate that the proposed testing protocol is

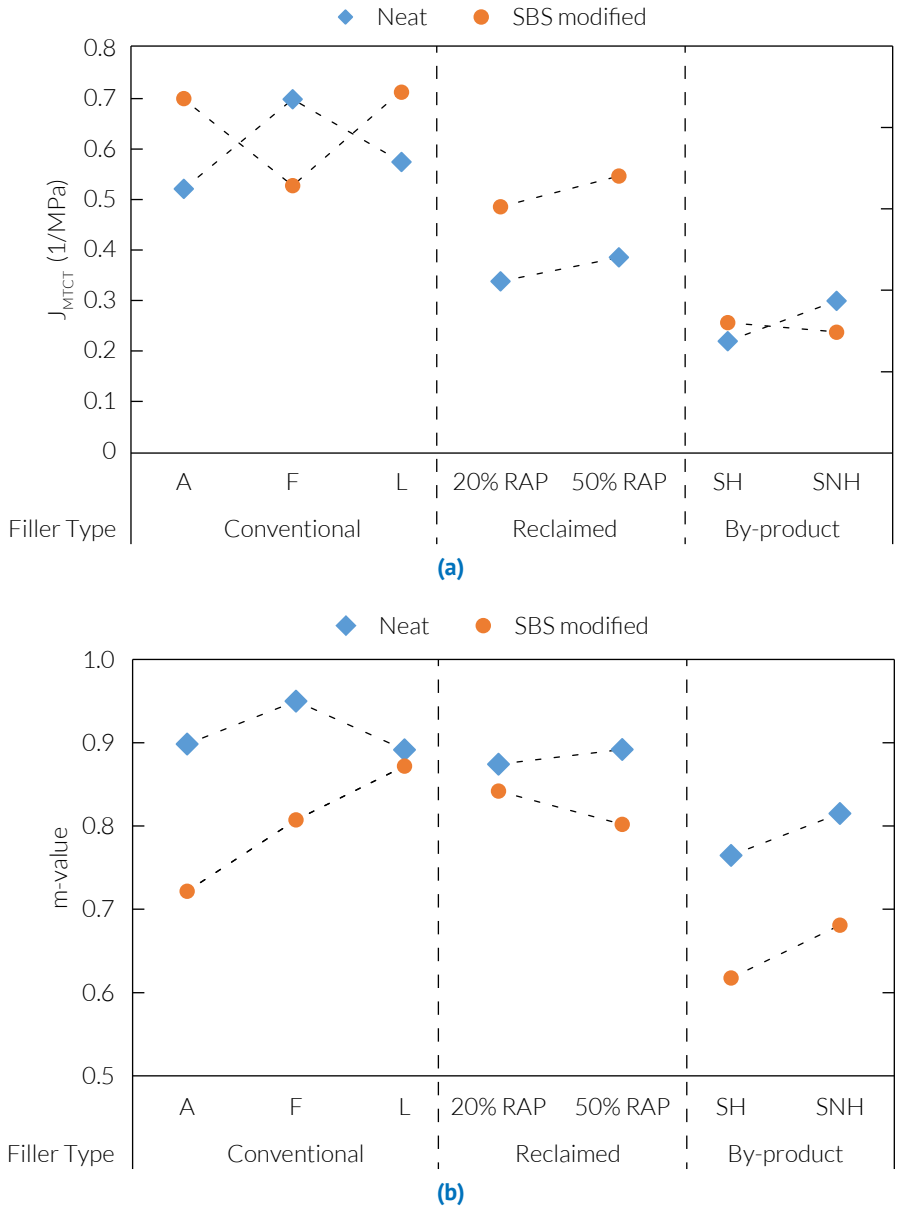

Figure 4.23 Interpretation of the bitumen-filler reaction, dividing the data series by filler types.

accurate, establishing that the probability to fall in the 95% CI is over 92% for the m-value and over 95% for the J_{MTCT}.

5

Results and discussion

This chapter introduces the results and their discussion, in order to better understand the influence of the mastic creep behavior on HMA response.

The pursuit of the proposed objective was obtained dividing the fillers by their nature: By-product, Conventional, and Reclaimed.

The analysis proposed collects the data about the creep behaviour of the investigated materials, both mastics and HMAs, and tries to interpret the correlation occurring between them.

Each paragraph starts comparing the MSCR data with the MTCT results. This was decided in order to understand whether the MTCT is able to correlate the direct tensile creep behaviour to the rutting predicting capacity of the MSCR considering the J_{nr} computed using 3200 Pa. This shear stress was used because it is involved for defining the MSCR curve (§3.2). It is worth indicating that the MSCR results were split using two axes due to the differences among the neat- and SBS modified-tested materials.

Secondly, the J_{MTCT} and m-value$_{MTCT}$ were compared with the creep compliance, m-value, DCSE, and FE of HMAs. This comparison aims at interpreting both the creep compliance and strain-rate of mastics. Thus, the MTCT parameter could help to better interpret the HMA mechanical and cracking behaviours.

5.1. Interpretation of results for conventional fillers

Figure 5.1 shows the possible relationship which may occur between the MSCR test and the new testing method MTCT proposed in the herein study. Comparing Figure 5.1a and Figure 5.1b is possible to highlight that when the J_{MTCT} increases the J_{nr} decrease for both the considered loads.

It is worth specifying that the differences among the J_{nr}s of the SBS modified-based materials are not significant, which implies that the elasticity of the bitumen is predominant when the mastic is share stressed. Conversely, the capability to rutting resistance of the neat materials measured by the J_{nr} showed significant differences among A-, L-, and F-filler using.

Before comparing both mastic and HMA creep parameters, it must be highlighted that the creep of mastics is not similar to the HMAs creep (Figure 5.2). This is due to the presence of different variables, such as AVC%, aggregate distribution, bitumen absorbed by the coarse aggregates, which affect the creep behaviour. This condition indicates that the accumulation of the deformation is dominated by the quantity of the free-virgin asphalt binder, which is not absorbed by either aggregates or filler particles. This mechanism is strictly dependent by the filler-bitumen reaction.

Analysing Figure 5.2c is possible to recognise that despite the same creep trend for both neat- and SBS modified-based materials, the different bitumen-filler reactions play a key role. In fact, considering Figure 5.2a, the phisico-chemical bitumen-filler reactions

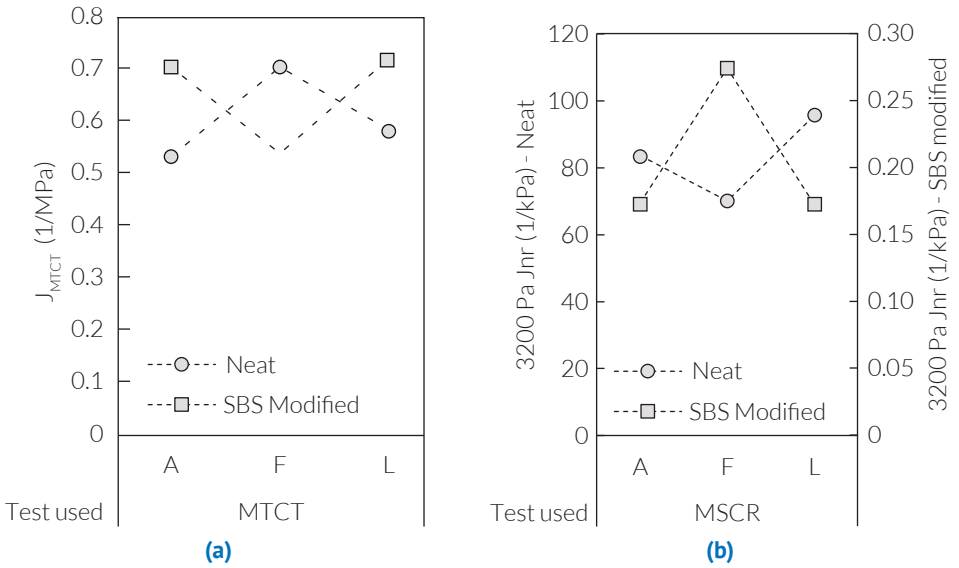

Figure 5.1 Comparison between MTCT results ***(a)*** interpreted using the Power model, and MSCR data ***(b)***.

of L-, F-, and A-filler radically change when they are mixed with SBS modified or neat bitumen.

As expected, the bitumen-filler reaction influences also the m-value. In fact, as noticeable in Figure 5.2b, the mastic m-value follows quite the same trend when the F- and A-filler are combined with both the used bitumens, while the L-filler exhibited the same m-value for both neat and SBS bitumens. It is worth noticing that, considering the A- and F-filler, the phisico-chemical reaction reduces the strain rate of the mastics. Those conditions guarantees quite the same m-value for the A- and F-filler, while the L does not allow keeping the same damage rate as for the mastic level. This may be linked to the different amount of free-bitumen in the mixtures, which influences the voids content (their distribution), and the aggregate interlock.

Considering the dissipating energy capability (Figure 5.3), the same analysis done for the creep behaviour can be confirmed. In fact, the previously noticed phisico-chemical reactions similarly affect the dissipative capacity of both mastics and HMAs. In this case, especially for the mixtures made using SBS modified, the DCSE and FE trend is flipped, if compared to the creep behaviour. Since the creep compliance represents the proneness of the material to accumulate the strain under a constant load, the higher is the HMA creep compliance, the lower is the DCSE.

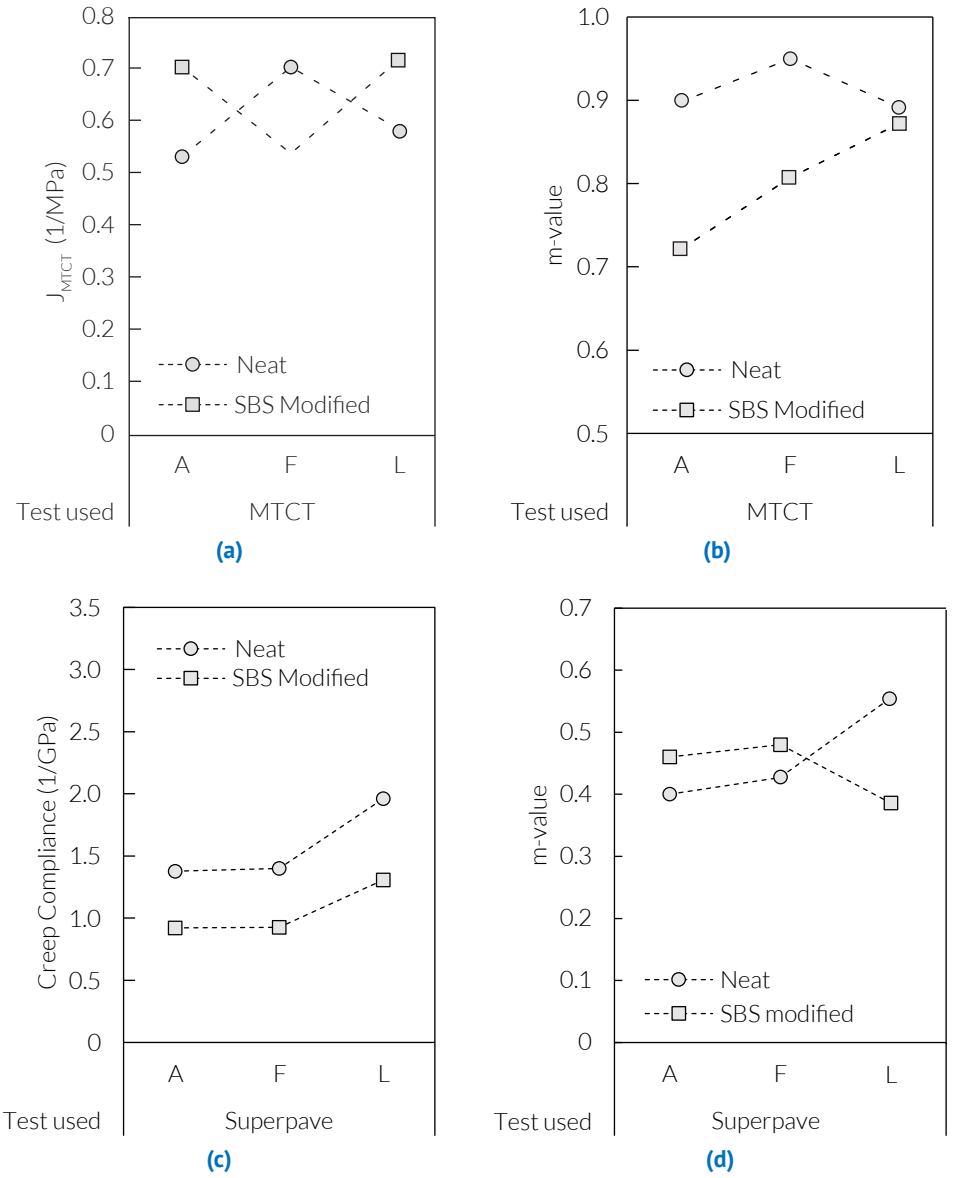

Figure 5.2 Comparison among MTCT parameters, J_{MTCT} ***(a)*** and m-value$_{MTCT}$ ***(b)***, and HMA creep parameters, creep compliance ***(c)*** and m-value ***(d)***.

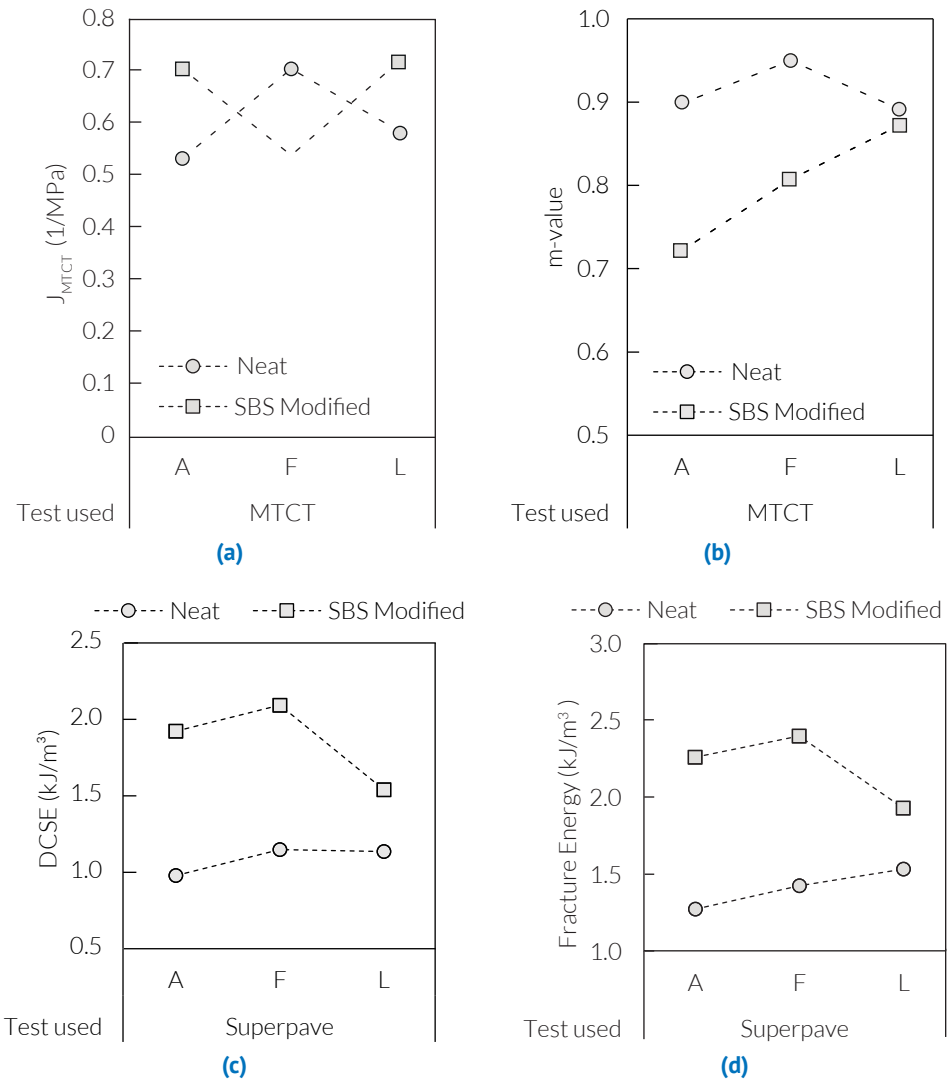

Figure 5.3 Interpretation of the dissipating capacity of the mastics through the MTCT parameters (***a***, and ***b***), and HMA creep behaviour parameters (***c***, and ***d***).

5.2. Interpretation of results for By-product fillers

The comparison between the MTCT and MSCR results shows that the creep behaviour exhibited have quite the same trend for both the analysed series, neat and SBS modified, respectively. This implies that filler effects dominate the mastic behaviour. However, as noticeable the MSCR results needed two axes to compare the materials Figure 5.4. This requirement is due to the testing temperature (64 °C), which allowed both the materials to behave in the visco-elasto-plastic range. Thus, the differences between neat- and SBS modified-based materials is widely different.

By analysing the results shown in Figure 5.5, it can be noticed that the higher is the J_{MTCT}, the lower is the HMA creep compliance. This condition is due to the AVC%, void distribution, and the amount of absorbed bitumen. Because the HMAs prepared with by product were distinguished by high AVC%, it can be supposed that if the J_{MTCT} is high the aggregates slowly move because the deformation is demanded to the mastic. Vice versa, the aggregates are able to fill the voids. Therefore, the first condition indicates low deformation level (low HMA creep compliance), while the second one gives back high deformation (Figure 5.5a and Figure 5.5c).

This effects are also recognised analysing the m-value of both mastics and HMAs. In fact, when MTCT m-value is high, this indicates that the mastic assimilates the deformation also in the HMAs. Therefore, the damage rate is lower for the HMAs (Figure 5.5d). Vice versa, the aggregates are able to fill the void. Thus,the damage rate of HMA is high.

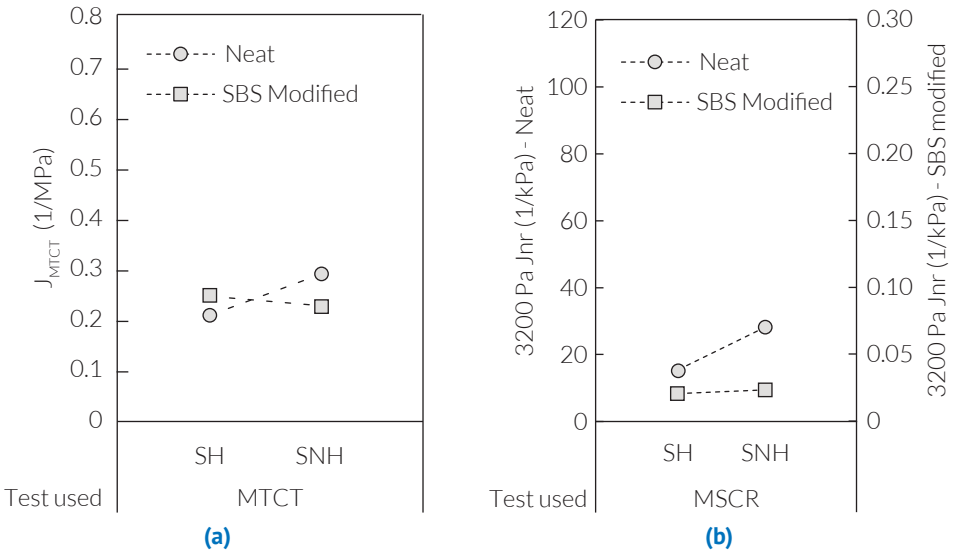

Figure 5.4 Comparison between MTCT results ***(a)*** interpreted using the Power model, and MSCR data ***(b)***.

The outcomes previously discussed have been also confirmed by the analysis of the dissipative aptitude of the HMAs and mastics made using LFS (Figure 5.6). In fact, the analysis proposed above is especially confirmed in terms of m-value. This confirms that when the mastic rapidly deforms, the ability of the HMA to dissipate energy is low. That condition might be due to the different load distribution. In fact, when the mastic firstly reacts to the material is distinguished by high strain-rate, corresponding low dissipative energy capability. Vice versa, when the mastic slowly reacts, the aggregates are able to move filling the voids and increasing the interlocking between them. Thus, the energy dissipated is higher for the second condition than the first one.

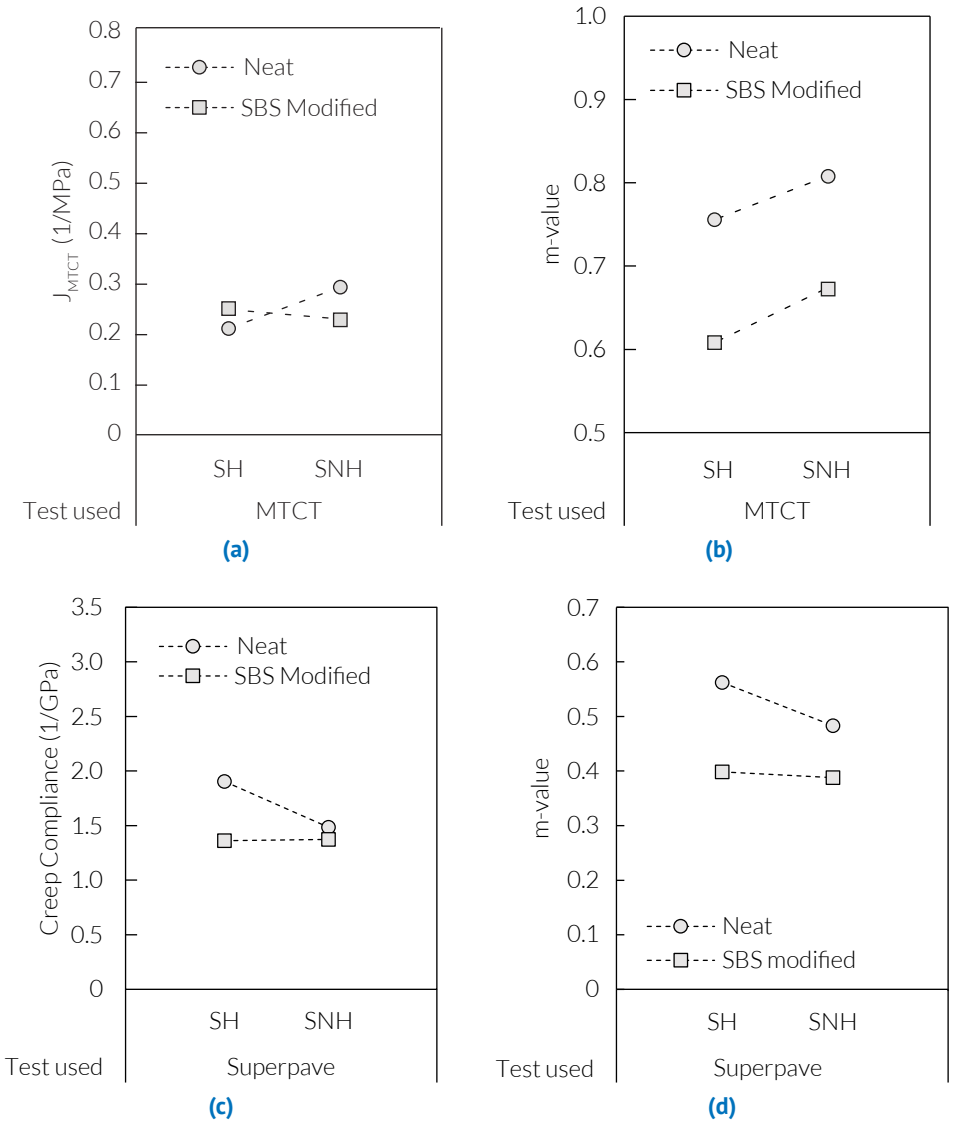

Figure 5.5 Comparison among MTCT parameters, J_{MTCT} ***(a)*** and m-value$_{MTCT}$ ***(b)***, and HMA creep parameters, creep compliance ***(c)*** and m-value ***(d)***.

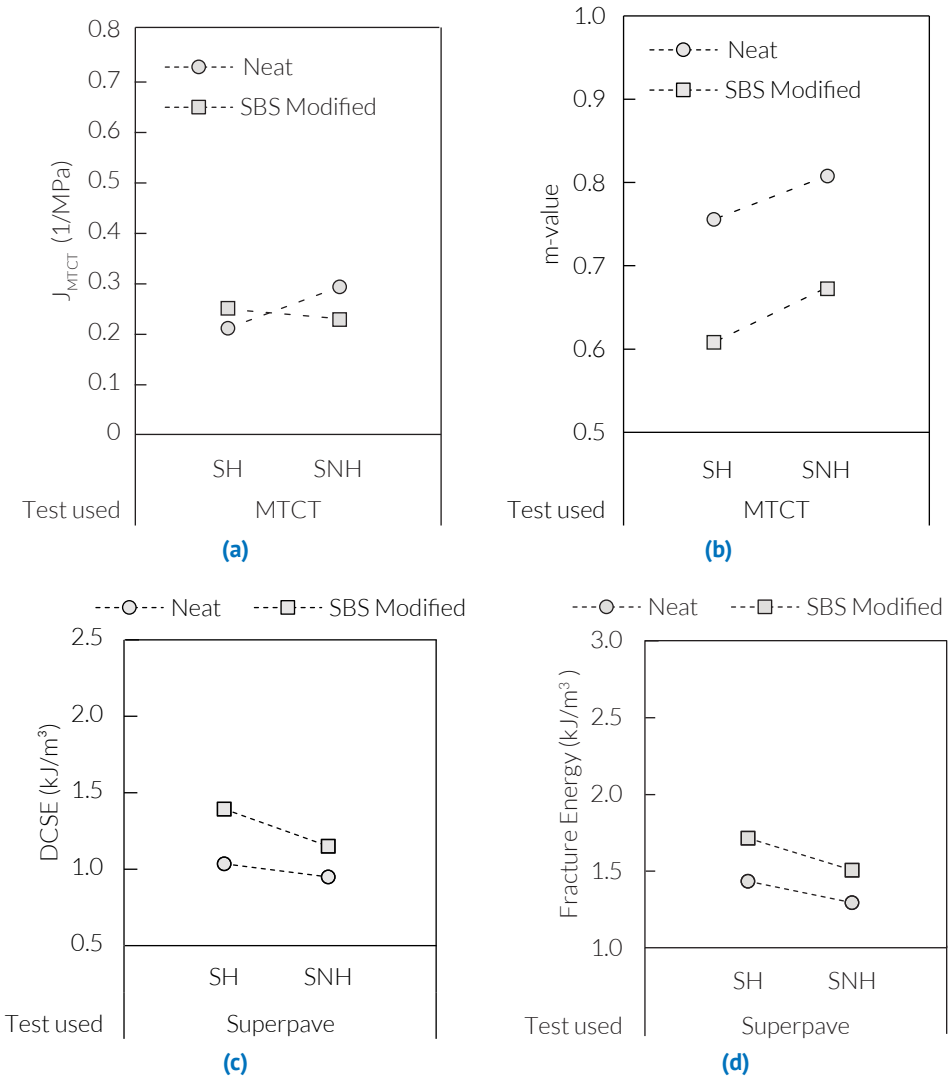

Figure 5.6 Interpretation of the dissipating capacity of the mastics through the MTCT parameters (***a***, and ***b***), and HMA creep behaviour parameters (***c***, and ***d***).

5.3. Interpretation of results for reclaimed fillers

The comparison between MTCT and MSCR results is also proposed for the reclaimed material, as shown in Figure 5.7. The proposed analysis starts from considering widely low the J_{MTCT} of the reclaimed materials. Probably, despite the mix design described in the previous Chapters, the amount of filler is not perfectly controlled. This condition is due to the presence of clusters also at micro-scale (d<0.075 mm), as reported by the SEM analysis (Chapter 2). Thus, the filler bitumen ratio may be not properly respected. Therefore, the interpretation considered only the effects of the WCO on the creep behaviour of mastics and HMAs.

Considering Figure 5.7, the effects of WCO are better described by the MTCT, which highlighted the differences between the used RAP% (50% and 20%). In fact, the materials containing 20% RAP exhibited lower J_{MTCT} than the other series. This is true for both the used binders. Consequently, both the 50% RAP series, which contain WCO, exhibited high propensity to accumulate deformation. Neverthelles, both blended bitumen and its reaction with the virgin filler could play a key role on the deformation of materials containing them. On the other hand, the increased amount of filler negatively influenced the results of the MSCR test, mitigating the effects of the WCO.

Passing to the creep behaviour of mastics and HMAs containing RAP (Figure 5.8), the interpretation of the WCO effects is quite difficult to capture at mastic level, while HMAs containing WCO treated RAP exhibited high creep, except for the combo SBS

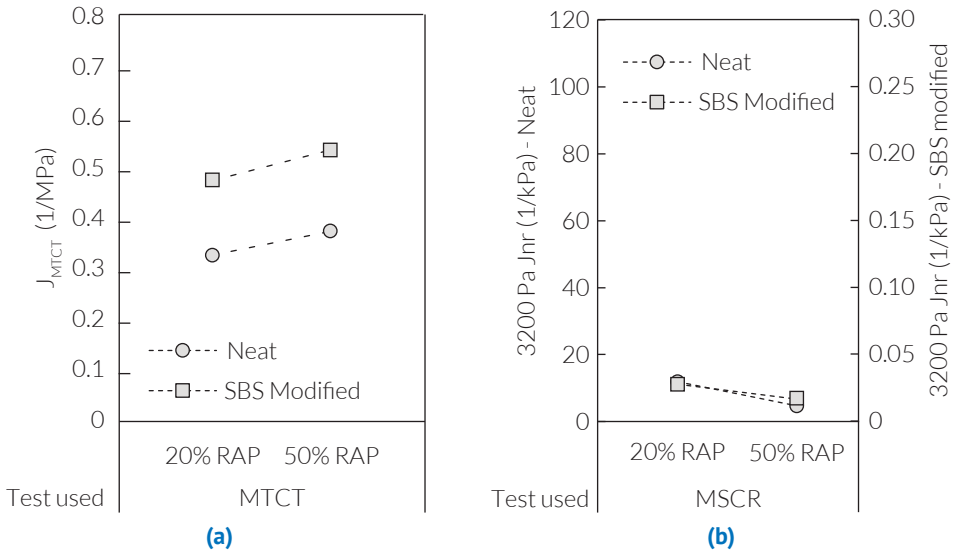

Figure 5.7 Comparison between MTCT results ***(a)*** interpreted using the Power model, and MSCR data ***(b)***.

modified + RAP 20%.

The analysis of the dissipative capacity of both the investigated phases (Figure 5.9) shows that the higher is the J_{MTCT}, the lower is DCSE of the HMAs. Therefore, this is linked to the stress propagation into the HMA structure. In fact, when the aggregates firstly reacts the dissipative capacity of the material is high. This is possible only if the mastic has a slow strain-rate. Conversely, when the J_{MTCT} is high, the HMA exhibited low capability to dissipate energy.

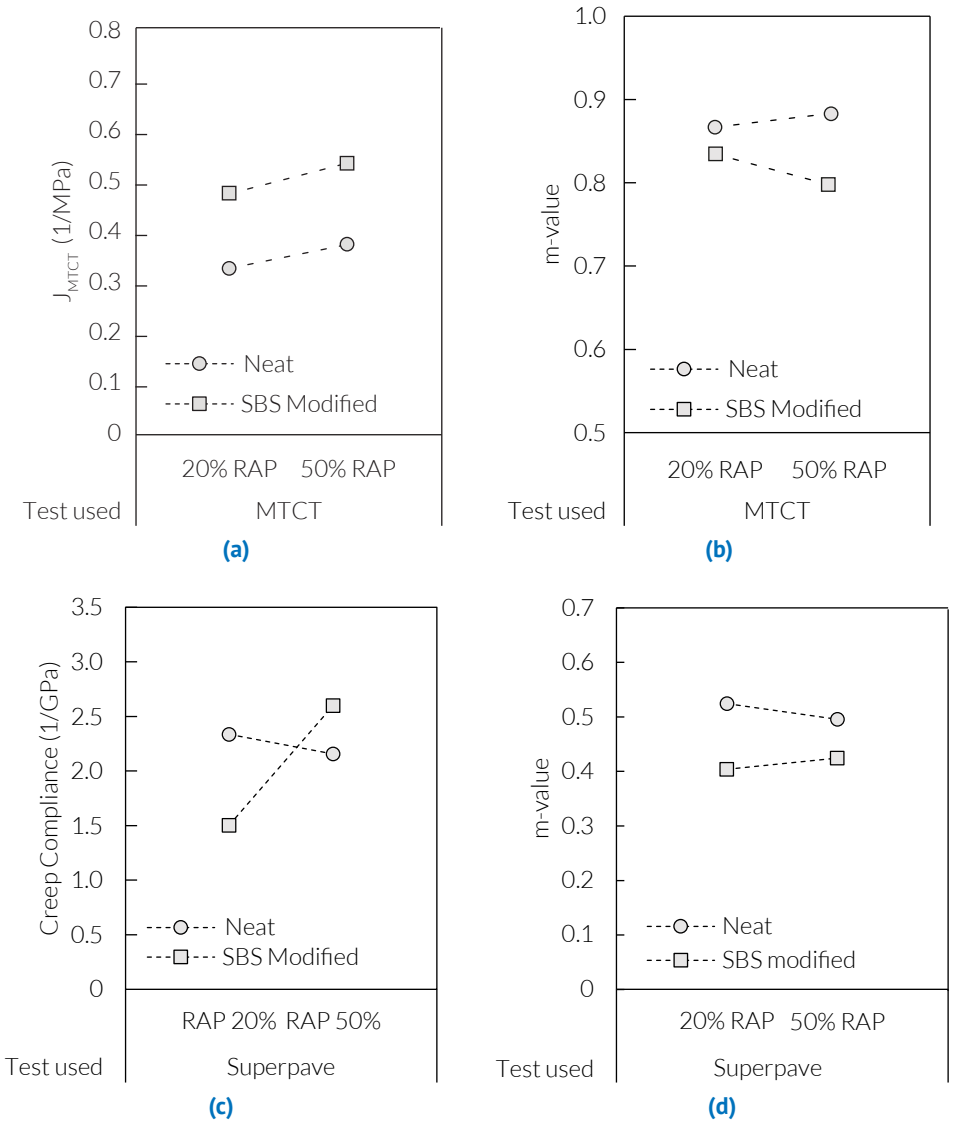

Figure 5.8 Comparison among MTCT parameters, J_{MTCT} ***(a)*** and m-$value_{MTCT}$ ***(b)***, and HMA creep parameters, creep compliance ***(c)*** and m-value ***(d)***.

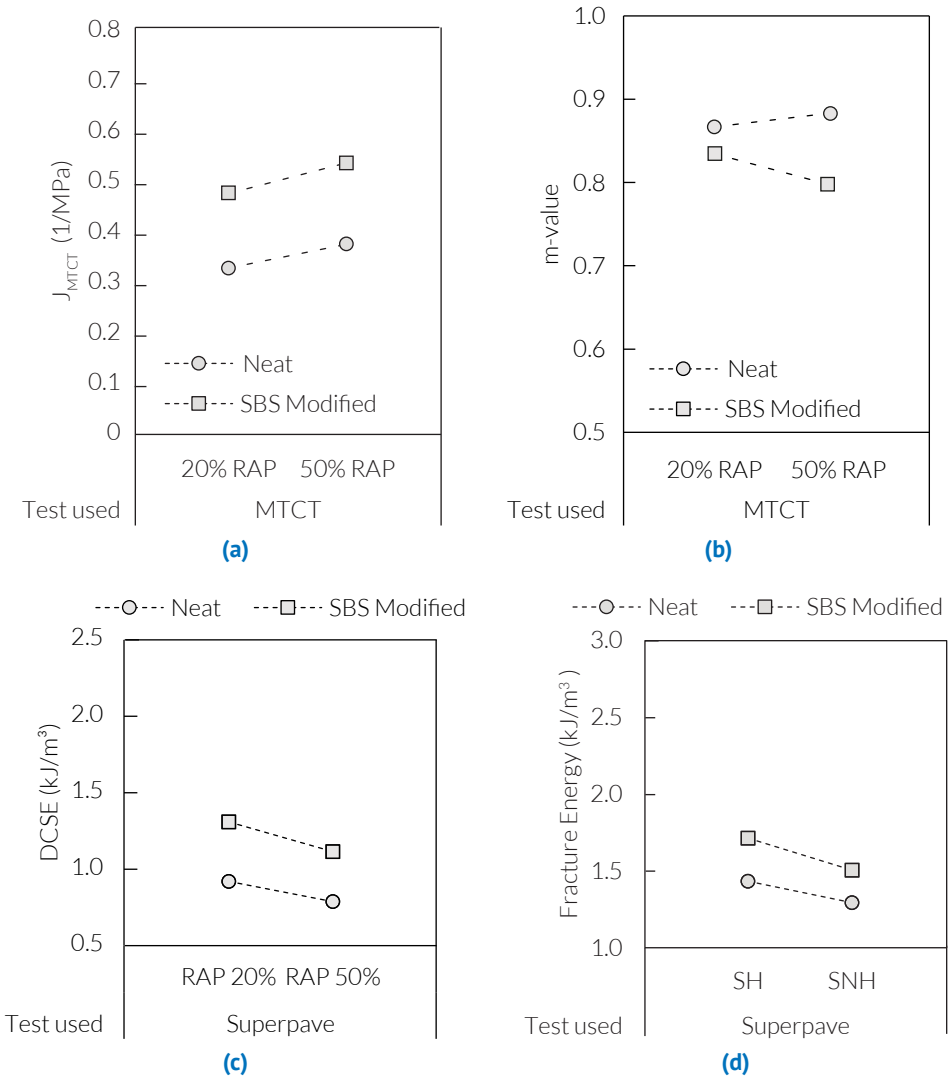

Figure 5.9 Interpretation of the dissipating capacity of the mastics through the MTCT parameters (***a***, and ***b***), and HMA creep behaviour parameters (***c***, and ***d***).

6

Summary and conclusions

6.1. Summary

The aim of this research project was to develop a multiscale approach to interpret the creep behaviour of HMAs. Therefore, two different phases of HMAs were investigate using standard tests, Superpave and MSCR tests, commonly used for characterising pavement materials, and an experimental approach based on the tensile configuration proposed by Montepara et al. [12] and validated by Romeo et al. [129] and Roberto et al. [25]. In order to achieve the proposed aim, a new testing method and tensile creep gravity machine were properly designed. Considering the deformability of the materials, a no-contact measurement system based on the DIC technique was used. The main outcomes can be summarised as follow:

- The accuracy and precision of both testing gravity machine and measurement system are statistically significant;
- The repeatability and reproducibility of the testing method is not operator dependent, indicating that it is suitable for other laboratories.
- The new testing method assures that the material keeps a linear visco-elastic behaviour.
- The results confirm that the adopted methodologies are able to efficiently highlight the dissipative capability of mastics underlining the differences occurring in terms of phisico-chemical filler-bitumen reactions.

The new methodology was developed considering the Kelvin-Voigt model and Power law to interpret the creep behaviour of both mastics and HMAs. To better understand the multi-scale behaviour of asphalt materials, three different filler categories, conventional, by-product, and reclaimed, were combined with two asphalt binders, SBS modified and Neat, respectively. The interpretative analysis was performed considering both the mechanical and cracking behaviour (dissipative capability) of the analysed phases.

The dissipative capability of the investigated materials followed the HMA fracture mechanic framework proposed by Zhang et al. [6], Roque et al. [7, 54], which is based on the Superpave IDT test. Thus, the Superpave protocol was used from the specimen preparation to the testing procedure and data analysis, to mechanically characterised the HMAs. The collected data were successively analysed and compared to the mastic results. Finally, the interpretative analysis was done.

6.2. Summary of findings

The main findings of the discussed research project may be summarised as follow:

- The use of servo-hydraulic machine gives back not significant results especially when not-heavy load are required. This was independent of the cell load used.

- The use of the designed gravity machine allows to obtain significant results passing from a not consistent series of data obtained using the servo-hydraulic machine to a consistent data collection generally distinguished by a p-value average over 0.9.
- The HMA exhibited a filler-dependent behaviour in terms of deformation, confirming the findings of previous studies [12, 25, 129].
- Basically, the alternative materials, by-product group, require high amount of virgin bitumen due to their absorption. This condition reduces also the workability of both mixtures and mastics.
- The MSCR might be not useful for mastic containing RAP. This is linked to the presence of clusters also at micro-scale, which do not allow to perfectly control the bitumen-filler ratio. Thus, when the filler particles increase the 1 mm gap is not suitable to accurately perform the MSCR test.

6.3. Conclusions

Based on the findings previously summarised, the following conclusion were achieved:

- The use of the same grading curve guaranteed quite the same elasticity stiffness for all the analysed materials. In fact, significant differences were not detected during the resilient modulus analysis. Therefore, using the same grading curve allows to accent the visco-elastic part of the HMAs. This condition confirms that the failure strain of materials is filler-dependent.
- The behaviour of the mixtures is filler-type related. But, generally, the higher is the creep obtained performing the new testing procedure, the lower is the creep compliance of the mixture. Particularly, this indicates two condition. The first one is realised when J_{MTCT} is higher. On that case, the mastic firstly reacts to the loading condition. Vice versa, the aggregate skeleton reacts modifying the HMA internal structure reducing the air voids.
- The DCSE of HMAs is much more related to the m-value of mastics than the creep parameter J_{MTCT}. In fact, when the m-value, which describe the damage rate of mastics, is high the DCSE of HMA is also high. This condition depends on the internal stress distribution during the Superpave IDT tests. Summarising, the lower are both the J_{MTCT} and the m-value of mastics, the higher are both DCSE and FE of HMAs.
- The behaviour of mixtures containing RAP is not completely clear because since the RAP is distinguished by low amount of particles below 0.075 mm, the mastic analysis is not completely related to HMAs' behaviour.

6.4. Further improvements and suggestions

During the laboratory activities to achieve the proposed aim, several criticisms were underline. Therefore, further improvements are underlined, which are following summarised:

- The accuracy of the new testing method can be increased by modifying the dog-bone mastic sample casting procedure. In fact, proper silicon moulds should be employed to reduce the differences in term of thickness of the samples, which actually is ± 0.15 mm.
- The same analysis, made for the creep behaviour, should be extended to the recovery stage of the linear material behaviour, in order to better understand and interpret also the recovery ability of mastic materials.
- The development of a creep approach for the IC phase is particularly suggested especially when using RAP materials. This approach could be based on the specification described by Yan et al. [138], Van den bergh [144], and Sánchez et al. [145] for elaborating a mix-design procedure. While, the tensile testing approach could be based on the specimens' shape indicated by Yan et al. [138]. Because the specimen are modelled to bring the material at failure point, this should be evaluated, and potentially modified to maximise the performance of the potential creep and recovery tensile test.

A

Appendix

A.1. Matlab Code for the motion tracking system

A.1.1. Strain calculation

```
clear all
clc
close all
%% Input data

% prompt = {'Width', 'Height', 'Frames per second'};
% tit = 'Input image dimension [pixels]';
% dims = [1 35];
% definput = {'400',  '800', '1'};
% s = inputdlg(prompt,tit,dims,definput); % Column where I save the input
% width = str2num(s{1});
% heigth = str2num(s{2});
% fps = str2num(s{3});
width = 400;
heigth = 800;
fps = 1;
%
%
ch = 'C:\Users\Antonio Roberto\Desktop\Programmi_Matlab_completi'; % Matlab-script-folder path
%% File to open and data extraction

selpath = uigetdir('C:Desktop'); % Select folder where you have saved your files
D = dir(fullfile(selpath,'*.csv'));
cd(selpath)
%
for ii = 1 : length(D)
    filename = D(ii).name; % Save only name's colum
    DAT = readtable(filename); % Import data from DIC elaboration files
    x(:, ii) = DAT.Var1;
    y(:, ii) = DAT.Var2;
end
%
X = array2table(x); % x coordinates
Y = array2table(y); % y coordinates
diX = (width * (X.x2 - X.x1)).^2;
diY = (heigth * (Y.y2 - Y.y1)).^2;
dist = sqrt(diX + diY);
%
ustrain = abs(((dist - dist(1,1))./ dist(1,1))) * 1000 % micro-strain * 10^3
%
[row, col] = find(ustrain > 0 & ustrain < 1, 1, 'last'); % find starting point
%
lr = length(row);
if length(row) == 0
    [row, ~] = find(ustrain > 0, 1, 'first'); % find starting point
    lr = length(row);
end
%
def(:,:) = ustrain(row - 1 : end, :);
```

```
def(1,1) = 0;
t = (0 : length(def)-1) ./ fps;
time = t';
%% Saving data

cd ..\
w = find(selpath == '\', 1, 'last');   %Find test label
s = selpath(w+1:end); % Test lable
xsc = strcat('Results_', s,'.xlsx');
A = [time, def];
B = ["Time [s]", "Strain"];
xlswrite(xsc, B,'Cumulated Def.','A1');
xlswrite(xsc, A,'Cumulated Def.','A2');
%
clc
```

A.1.2. Data analysis

```
clear all
clc
close all
%
load = 60;
ch = 'C:\Users\Antonio Roberto\Desktop\Programmi_Matlab_completi\Gravity
    machine'; % Matlab-script-folder path
cs = 'C:\Users\Antonio Roberto\Desktop\Programmi_Matlab_completi\Gravity
    machine\Motion tracking' % Path of the selectdata function
%% File to open
selpath = uigetdir('C:\Users\Antonio Roberto\Desktop'); % Select folder where
     you have saved your files
D = dir(fullfile(selpath,'*.xlsx'));
cd(selpath)
%
%% Data extracting procedure
%
d = 180;                % Duration of the test
k = 1;
%% Find the minimum length of the arrays analysed
%
cd(cs)
[~,ndx] = natsortfiles({D.name}); % file sorting operation
D = D(ndx);
cd(selpath)
for ii = 1 : length(D)
    filename = D(ii).name; % Save only name's column
    if exist(filename) == 2
        [DAT,txt,~] = xlsread(filename,'Cumulated Def.');   % Import data
            from DIC elaboration files
        T = array2table(DAT);
        rowd = find(T.DAT1 == d);
        stept0 = find(T.DAT1 == 0);
        stept1 = find(T.DAT1 == 1);
        nfps = stept1 - stept0;                          % Filtering fps
        [row , ~] = find(T.DAT2 > 1 , 1, 'first');       % Find starting point
        if nfps > 1
            def (:,ii) = T.DAT2(row - 1: nfps : rowd + row - 2);
            clear t
        else
```

```
37              def (:,ii) = T.DAT2(row - 1 : rowd + row - 2 );
38          end
39          num = num2str(k);
40          ntest =  strcat("Test ", num);                    % New file name
41          nt(:,k) = ntest;
42          k = k + 1;                                        % Counter
                upgrading operation
43      end
44  end
45  %
46  clear i
47  for i = 1 : size(def,2)
48      t(:,i) = 1: 1/nfps :size(def,1);
49  end
50  def(1 , :) = 0;
51  time = t(:,1)-1;
52  cd(cs)
53  % Check the deformation
54  [stats_def, ~] = controlchart(def,'display', 'off'); % mean, range and
        standard dev. into stats
55  [~,~,d2,~] = ttest(max(def), max(stats_def.mean));
56  def_avg = stats_def.mean;
57  if d == 1
58      msg = warndlg('Check the deformation data', 'No statistic validation of
            the data')
59      plot(t,def)
60      hold on
61      ylim([1 +inf])
62      plot(time , stats_def.mean, 'dr')
63  end
64  ud = find(def(end,:) > d2(1) & def(end,:)< d2(2)); % Trueness and accuracy of
         the test (m-values)
65  [stats_def, ~] = controlchart(def,'display', 'off'); % mean, range and
        standard dev. into stats
66  df = max(def(end,ud));       % Deformation after its check
67  per_err_def = abs(max(def_avg) - def(end,ud))*100 / max(def_avg); % Checking
        the percentage error of the deformation
68  %
69  J = def(:,ud)./1000;    % Creep after the deformation check, transformation
        from microstrain to strain
70  J = J./(load/200);          % Creep after the deformation check
71  %% Fitting with non-linear model A + B*x.^m
72
73  % Creep analysis
74  %
75  for iii = 1 : size(J,2)
76      a = J(:,iii);
77      [opt,gof] = createFit(time, a);
78      %  Output:
79      %      opt : a fit object representing the fit.
80      %      gof : structure with goodness-of fit info.
81      D0(iii,:) = opt.A;
82      D1(iii,:) = opt.B;
83      m(:,iii) = opt.m;
84      R_fit(iii,:) = gof.rsquare;
85  end
86  cd(selpath)
87  %
```

A

```
88  [stats_J, ~] = controlchart(J,'display', 'off')
89  j = stats_J.mean;
90  cd(cs)
91  [opt,gof] = createFit(time,j);
92  %  Output:
93  %      opt : a fit object representing the fit.
94  %      gof : structure with goodness-of fit info.
95  D0_avg = opt.A;
96  D1_avg = opt.B;
97  m_avg = opt.m;
98  R_fit_avg = gof.rsquare;
99  cd(selpath)
100 [a,a1,a2,a3] = ttest(m,m_avg); % t-test alpha = 5% ci = 95%
101 tab = [a1,a2(1),a2(2),a3.sd];
102 cr = max(J(end,:));
103 %
104 J_fit = D0_avg + D1_avg .* time.^m_avg
105 [aJ,aJ1,aJ2,aJ3] = ttest(max(J),max(J_fit)); % t-test alpha = 5% ci = 95%
106 tabd = [aJ1,aJ2(1),aJ2(2),aJ3.sd];
107 %% Save data
108
109 s = selpath(find(selpath == '\', 1 ,'last') + 1 : end)
110 xsc = strcat('Results_', s,'.xlsx');
111 E = ["Considered series", nt(:,ud:end)];
112 E1 = vertcat(["Fit mvalue", m],["Fit Creep", max(J)]);
113 C = vertcat(['Time [s]',nt(:,ud),'Avg.', 'Std. Dev.', 'Error'],[time , def(:,
        ud), stats_def.mean , stats_def.std , 2*stats_def.std]);
114 D = vertcat(vertcat(["Creep fitted (1/MPa)", "Err. Creep (1/MPa)"],[max(J_fit
        ) , (2*aJ3.sd)]) , vertcat(["Avg. m-value" , "Err. mvalue"],[m_avg, 2*a3.
        sd]));
115 F = vertcat(['Time [s]',nt(:,ud),'Avg.', 'Std. Dev.', 'Error'],[time , J,
        stats_J.mean , stats_J.std , 2*stats_J.std]);
116 xlswrite(xsc, C,'Cumulated Def.','A1');
117 xlswrite(xsc, D,'Analysis','A1');
118 xlswrite(xsc, E ,'Analysis','F1');
119 xlswrite(xsc, E1 ,'Analysis','F2');
120 xlswrite(xsc, F,'Creep Analysis.','A1');
121 % writetable(cell2table(tbl_m(2:end,:),'VariAbleNames',{'Source' 'SS' 'df'
            'MS' 'F' 'pvalue'}),'ANOVA.csv');
122 writetable(array2table(tab,'VariableNames',{'p','Lower_CI_limit','
        Upper_CI_limit','Standard_deviation'}),'t_test mvalue.csv');
123 writetable(array2table([tabd,D0_avg,D1_avg],'VariableNames',{'p','
        Lower_CI_limit','Upper_CI_limit','Standard_deviation', 'D0','D1'}),'
        t_test maxcreep.csv');
124 %
125 clc
126 close all
127 %% Plotting
128
129 cd(ch)
130 %
131 Chart(def(:,ud))
132 hold on
133 legend(nt', 'Location','northwest');
134 cd (selpath)
135 figname = s;
136 hfig = figure(1)
137 set( hfig , ...
```

```
    'Color',[1 1 1],...
    'PaperType','b5',...
    'PaperSize',[25.00 17.60 ],...
    'PaperUnits', 'centimeters',...
    'PaperPositionMode','manual',...
    'PaperPosition', [0 1 12.2 7],... %image dimension
    'InvertHardcopy','off');
set(gcf,'Name',figname)
print('-dpdf', '-painters', get(gcf,'Name'));
print( '-dpng' , '-r1200' , get(gcf,'Name'))
close (hfig)
%
clc
%
msgbox(nt(:,ud)','Considered series','help')
```

A.1.3. Results elaboration and comparison

```
clear all
clc
close all
%
ch = 'C:\Users\Antonio Roberto\Desktop\Programmi_Matlab_completi\Gravity
    machine'; % Matlab-script-folder path
%% File to open
selpath = uigetdir('C:Desktop'); % Select folder where you have saved your
    files
D = dir(fullfile(selpath,'*.xlsx'));
cd(selpath)
%
%% Data extracting procedure
%
k = 1;
%
for ii = 1 : length(D)
    filename = D(ii).name; % Save only name's column
    if exist(filename)== 2
        [DAT, txt,~] = xlsread(filename,'Cumulated Def.'); % Import data from
            DIC elaboration files
        [DAT1, ~ , ~] = xlsread(filename,'Analysis'); % Import data from DIC
            elaboration files
        [DAT2, ~ , ~] = xlsread(filename,'Creep Analysis.'); % Import data
            from DIC elaboration files
        qw = find(strcmp(txt, 'Avg.'));          %Find AVG column
        J(ii,1) = DAT2(size(DAT2,1),qw);
        errJ(ii,1) = 2 * DAT2(size(DAT2,1),qw + 2);
        w = find(filename == '_', 1, 'last');   %Find test label
        ntest = filename(w + 1 : end-5);  % New file name
        nt(:,k) = convertCharsToStrings(ntest);
        def_ma(ii,1) = DAT1(1,1);
        def_erbar(ii,1) = DAT1(1,2);
        mv (ii,1) = DAT1(3,1);
        mv_erb (ii,1) = DAT1(3,2);
        if ii == 1
            strainYY(:,ii) = DAT(:,qw);       %Avarage strainYY values
            l (ii , 1) = length(strainYY);
        else
            l (ii , 1) = length(DAT);
```

```
36              if l(ii , 1) < l(ii-1 , 1)
37                  us = strainYY(1 : l(ii) , :);
38
39                  clear strainYY
40
41                  strainYY = us;
42
43                  strainYY(:, ii) = DAT(:,qw);      %Avarage strainYY values
44
45              else
46                  m = min(l);
47                  strainYY(:, ii) = DAT(1 : m,qw);      %Avarage strainYY values
48              end
49
50          end
51          k = k + 1;                          %Counter upgrading operation
52      end
53
54  end
55  time = 1 : length(strainYY);
56  time = time';                       %Test duration
57  %
58  %
59  %% Save data
60  %
61  pr = {'Enter name of data-folder:'};
62  title = 'Input';
63  dims = [1 35];
64  answer = inputdlg(pr,title,dims); % Dialog window for adding the file name
65  s = answer{1};
66  %
67  G = 'Results';
68  status = mkdir(G);
69  dd = dir(G); % find path of new folder;
70  dd = dd.folder;
71  cd(dd)
72  xsc = strcat('Results_', s,'.xlsx');
73  A = vertcat(["Time [s]",nt],[time,strainYY]);
74  B = vertcat( ["Material", "mvalue", "Error"],[nt',mv, mv_erb]);
75  C = vertcat( ["Material", "Creep (1/MPa)", "Error"],[nt', J, errJ]);
76  xlswrite(xsc, A,'Cumulated Def.','A1');
77  xlswrite(xsc, B,'mvalue','A1');
78  xlswrite(xsc, C,'Creep','A1');
79  %
80  clc
81  %
82  %% Plotting
83  cd(ch)
84  %
85  Chart(strainYY)
86  hold on
87  legend(nt', 'Location','northwest');
88  cd (dd)
89  figname = s;
90  hfig=figure(1)
91  set( hfig , ...
92      'Color',[1 1 1],...
93      'PaperType','b5',...
```

```
94      'PaperSize',[25.00 17.60 ],...
95      'PaperUnits', 'centimeters',...
96      'PaperPositionMode','manual',...
97      'PaperPosition', [0 1 13.5 7],... %image dimention
98      'InvertHardcopy','off');
99  set(gcf,'Name',figname)
100 print(gcf, '-dpdf', '-painters', get(gcf,'Name'));
101 print( '-dpng' , '-r1200' , get(gcf,'Name'))
102 close (hfig)
103 %
104 clc
105
106 %
107 bar(categorical(nt),mv);
108 hold on
109 errorbar(mv , mv_erb)
110 ylabel('m-value');
111 hfig=figure(1)
112 set( hfig , ...
113     'Color',[1 1 1],...
114     'PaperType','b5',...
115     'PaperSize',[25.00 17.60 ],...
116     'PaperUnits', 'centimeters',...
117     'PaperPositionMode','manual',...
118     'PaperPosition', [0 1 5.5 6.5],... %image dimention
119     'InvertHardcopy','off');
120 set(gcf,'Name','m-value bar')
121 print(gcf, '-dpdf', '-painters', get(gcf,'Name'));
122 print( '-dpng' , '-r1200' , get(gcf,'Name'))
123 close (hfig)
124 %
125 clc
126 %
127 bar(categorical(nt),J)
128 hold on
129 errorbar(J,errJ)
130 ylabel('Creep compliance (1/MPa)');
131 hfig=figure(1)
132 set( hfig , ...
133     'Color',[1 1 1],...
134     'PaperType','b5',...
135     'PaperSize',[25.00 17.60 ],...
136     'PaperUnits', 'centimeters',...
137     'PaperPositionMode','manual',...
138     'PaperPosition', [0 1 5.5 6.5],... %image dimention
139     'InvertHardcopy','off');
140 set(gcf,'Name','J_bar')
141 print(gcf, '-dpdf', '-painters', get(gcf,'Name'));
142 print( '-dpng' , '-r1200' , get(gcf,'Name'))
143 close (hfig)
144 %
145 clc
146 %
147 cd ../
```

A

A.2. Superpave matlab code

A.2.1. Data selection

```
clear all
clc
close all
%% Import Directory and Save Path

%
cs = ('C:\Users\Antonio Roberto\Desktop\Programmi_Matlab_completi\SetUp IDT SuperPave\Definitive_Software');
selpath = uigetdir('C:\Users\Antonio Roberto\Desktop');    % Select folder where you have saved your files
D = dir(fullfile(selpath,'*.dat'));
cd(selpath)                          % Save the folder's directory
%
for ii = 1:length(D)
    filename = D(ii).name;                    % Save only name's column
    if exist(filename)==2
        name(ii,1) = erase(string(filename), ".dat");       % name sheets and column
        DAT = importdata(filename);
        tf = isstruct(DAT);                  % Determine if input is structure array
        if tf == 1
            filenamepath = horzcat(selpath,'\',filename);
            Data = readtable(filename);
            load = Data.DCIn2_Load_250_R25_KN_ * -1;
        else
            load = DAT(:,5) * -1;

        end
        cd(cs)
        figure('Name', erase(filename , '.dat'),'WindowState','maximized');
        plot(load)
        hold on
        [~,~,ys] = selectdata('selectionmode','rect');     % Select data on the figure by using rectagle
        hold off
        close()
        cd(selpath)
        if isempty(ys)
            clear DAT
            delete(filename)
        end
    end
end
```

A.2.2. Superpave analysis

```
clear all
clc
close all
cs = ('C:\Users\Antonio Roberto\Desktop\Programmi_Matlab_completi\SetUp IDT SuperPave\Definitive_Software');
```

```
ra = 0.5; %x/y
C_compl = 0.6354 * ra^-1 - 0.323;
Di = 150; % Diameter of the SuperPave spedimens
cr_point = [1, 2 , 5 , 10 , 20 , 50 , 100 , 200 , 500 , 1000];
D0 = 0.0483459;
%% Import load for Creep tests and Resilient moduls test

prompt = {'Thickness [mm]', 'Resilient Modulus Load [kN]', 'Creep Load [kN]'
    };
tit = 'Input image dimension [pixels]';
dims = [1 35];
definput = {'',  '', ''};
s = inputdlg(prompt,tit,dims,definput); % Column where I save the input
tic = str2num(s{1});
L_cr = str2num(s{3});
L_mr = str2num(s{2});
t_ra = tic/Di;
v = -0.1 + 1.480 * ra^2 - 0.778 * t_ra^2 * ra^2;    % Poisson's ratio
area = pi * tic * Di / 2;
Csx = 0.984 - (0.01114 * t_ra - 0.2693 * v)  + (1.436 * t_ra * v);
%% Resilent modulus

uiwait(msgbox('Start with the analysis of the Resilient modulus: Select the
    data foleder'))
[filename,selpath] = uigetfile('*.dat');    % Select folder where you have
    saved your files
cd(selpath)                          % Save the folder's directory
if exist(filename)==2
    A = array2table(importdata(filename));
    de = abs(A.Var2) - abs(A.Var2(1,1));
    cd(cs)
    figure('WindowState','maximized');
    plot(de)
    hold on
    [~,~,ysmr] = selectdata('selectionmode','rect');     % Select data on the
        figure by using rectagle
    hold off
    close()
    cd(selpath)
    de_m_mr =  min(ysmr);        % minimum point of the selected cycle
    de_ma_mr =  max(ysmr);       % Maximum point of the selected cycle
    de_mr = de_ma_mr - de_m_mr; % Between 150 and 350 microstrin
    if de_mr > 150 & de_mr < 350
        MR = L_mr / (de_mr * 10^-6 * Di * tic * C_compl); % Resilient Modulus
            calculation [GPa]
    else
        uiwait(msgbox('Data are not consistent'))
    end
end
%% Creep compliance

uiwait(msgbox('Start with the analysis of the Creep compliance: Select the
    data foleder'))
[filename,selpath] = uigetfile('*.dat');    % Select folder where you have
    saved your files
cd(selpath)                          % Save the folder's directory
if exist(filename)==2
    A = array2table(importdata(filename));
```

```
56      de_c = abs(A.Var2 - A.Var2(1,1));
57      po = find(de_c == max(de_c));
58      if po < 1000
59          m_po = find(de_c == max(de_c(1000:end)));
60          de_cr = de_c(m_po-1000:m_po,1);
61      else
62          de_cr = de_c(po-1000:po,1);
63      end
64      time = 0 : length(de_cr) - 1;
65      if size(de_cr,1) < cr_point(end)
66          cr_point(end) = size(de_cr,1) - 1;
67          CR =  (de_cr(cr_point + 1) * 10^-6 * Di * tic * C_compl) ./ L_cr; %
                Creep compliance calculation [GPa]
68          m_value = (log(de_cr(cr_point(end)))-log(de_cr(500)))/(log(time(
                cr_point(end)))-log(time(500)));
69          D1 = (CR(end)-D0)/(1000^m_value);
70      else
71          CR =  (de_cr(cr_point + 1) * 10^-6 * Di * tic * C_compl) ./ L_cr; %
                Creep compliance calculation [GPa]
72          m_value = (log(de_cr(1000))-log(de_cr(500)))/(log(time(1000))-log(
                time(500)));
73          D1 = (CR(end)-D0)/(1000^m_value);
74      end
75  end
76  plot(cr_point,CR, '-')
77  %% Tensile strength Import Directory and Save Path
78
79  answer = questdlg('Do you have the tensile strength MTS data?', ...
80      'Checking', ...
81      'Yes','No','Yes');
82  % Handle response
83  switch answer
84      %
85      case 'Yes'
86          uiwait(msgbox('Start with the analysis of the tensile strength:
                Select the MTS data foleder'))
87          %
88          [filename,selpath] = uigetfile('*.dat');    % Select folder where you
                 have saved your files
89          cd(selpath)                                 % Save the folder's directory
90          %
91          if exist(filename)==2
92              name = erase(string(filename), ".dat");        % name sheets and
                    column
93              DAT = importdata(filename);
94              tf = isstruct(DAT);                     % Determine if input is
                    structure array
95              if tf == 1
96                  filenamepath = horzcat(selpath,'\',filename);
97                  Data = readtable(filename);
98                  load = Data.DCIn2_Load_250_R25_KN_ * -1;
99                  load = load - load(1);
100                 t = Data.Tempo_s_;
101             else
102                 load = DAT(:,5) * -1;
103                 load = load - load(1);
104                 t = DAT(:,1);
105             end
```

```
106             cd(cs)
107             figure('WindowState','maximized');
108             plot(t,load)
109             hold on
110             uiwait(msgbox('Select the load curve'))
111             [~,ti,ys] = selectdata('selectionmode','rect');     % Select data
                    on the figure by using rectagle
112             hold off
113             close()
114             cd(selpath)
115             row = find(ys > 0.01, 1,'first');
116             tim = ti(row:end,1);
117             time = tim - tim(1,1);
118             fg = find(time == 1,1,'first');
119             nfps = numel(1 : fg-1);
120             row1 = find(ys > 0.01 & ys < 0.2, 1,'last');
121             if isempty(row1)
122                 row1 = row;
123             end
124             ld = ys(row1:end,1);
125             ld(1,1) = 0;
126             clear DAT
127             uiwait(msgbox('Select the folder containing the Strain gauges
                    data'))
128             [filename1,selpath1] = uigetfile('*.dat');    % Select folder
                    where you have saved your files
129             cd(selpath1)                          % Save the folder's
                    directory
130             %
131             if exist(filename1)==2
132                 A = array2table(importdata(filename1));
133                 d = abs(A.Var2 - A.Var2(1,1));
134                 md = find(d == max(d),1,'first');
135                 d = d(1:md,:);
136                 negdif = find(d < 0, 1, 'last');
137                 if isempty(negdif)
138                     negdif = find(d == 0, 1, "last");
139                 end
140                 d = d(negdif + 1 : end);
141                 d(1,1) = 0;
142             end
143         end
144         if ~isempty(row)
145             if size(ld,1) > size(d,1)
146                 ld = ld(1:size(d,1),1);
147                 time = time(1:size(d,1),1);
148             else
149                 d = d(1:size(ld,1),1);
150                 time = time(1:size(ld,1),1);
151             end
152 %% Find the first fracture point
153
154             [rma , ~] = find(ld == max(ld));
155             yma = 0*d + max(ld);
156             xma = d(1:length(yma));
157             % Find the line passing for the elastic reagion of the analysed
                    material arbitrary chosen between 5 and 10 kN
158             x15 = find(ld > 20, 1,'first');
```

```
159             xel = [d(1:60)];
160             yel = [ld(1:60)];
161             fel = polyfit(xel,yel,1);
162             pel = polyval(fel,d(1:rma));
163             tri = find(pel > max(ld));
164             ye = pel(1:tri);
165             xe = d(1:tri);
166             if isempty(xe)
167                 xel = [d(1:90)];
168                 yel = [ld(1:90)];
169                 fel = polyfit(xel,yel,1);
170                 pel = polyval(fel,d(1:rma));
171                 tri = find(pel > max(ld));
172                 ye = pel(1:tri);
173                 xe = d(1:tri);
174             end
175             %
176             uiwait(msgbox('Select the area where the first fracture point can
                    be considered'))
177             cd(cs)
178             figure('WindowState','maximized');
179             plot(d,ld)
180             hold on
181             plot(xe,ye)
182             plot(xma,yma)
183             ylabel('Load [kN]')
184             xlabel('Microstrain')
185             %
186             [xi,yi] = polyxpoly(xe,ye,xma,yma);       % Find the intersaction
                    between the line passing for the load peak and for the
                    elastic reagion respectively
187             mapshow(xi,yi,'DisplayType','point','Marker','o')
188             %
189             % First fracture point
190             %
191             d_max = d(1:rma);        % deformation up to the maximum load
                    condition
192             [~,djj,ljj] = selectdata('selectionmode','rect');     % Select
                    data on the figure by using rectagle
193             close()
194             dj = cell2mat(djj);
195             lj = cell2mat(ljj);
196             for ii = 1 : length(dj)
197                 fj = polyfit(dj,lj,1); % fitting equation of the selected
                        data
198                 fp = (yi - ld(ii))/(xi - d_max(ii));
199                 perp(ii) = fj(1) * fp (1) ;
200             end
201             hj = find(perp == min(perp));
202             first_frac_poit = [dj(hj),lj(hj)];
203             perp_p = find(ld == lj(hj));
204             plot(d,ld)
205             hold on
206             plot(xma , yma)
207             plot(xe,ye)
208             ylabel('Load [kN]')
209             xlabel('Microstrain')
210             mapshow(dj(hj),lj(hj),'DisplayType','point','Marker','+')
```

```
211             mapshow(xi,yi,'DisplayType','point','Marker','o')
212             cd(selpath1)
213             stress = ld(1:perp_p ) * 1000 ./ area; % Stress up to first
                    fracture point
214             strain = d(1:perp_p ) ./1000;
215 %% Energetic Analysis
216
217             area_und = cumtrapz(strain,stress); % Area under the stress and
                    strain curve up to the first fracture
218             FE = area_und(end);
219             TS = max(stress)*Csx;
220             ef = max(strain);
221             e0 = ef - (TS/MR);
222             EE = 0.5 * (ef-e0) * TS;
223             DCSE = FE - EE;
224             A = ((Di)^-2.96) * (-0.0154) * ((TS-6.36) + 0.246 * 10^-7);
225             D1_ts = D1 / 145037.7;
226             DCSE_min = (m_value^2.99) * D1_ts / A;
227             ER = DCSE / DCSE_min;
228 %% Save data
229
230             cd (selpath)
231             cd ../
232             P = vertcat(["Time","Starin_10^-3","Stress_MPa"],[time(1:length(
                    strain)),strain,stress]);
233             energy = horzcat(["Fracture Energy [kJ/m^3]"; "Elastic Energy [kJ
                    /m^3]";"DCSE [kJ/m^3]"; "DCSE_min [kJ/m^3]"; "Energy Ratio [
                    kJ/m^3]"; "A"; "D1"],[FE;EE;DCSE;DCSE_min;ER;A;D1_ts]);
234             tensile = horzcat(["Tensile Stregth [MPa]";
235                 "Failure strain";...
236                 "Strain 0"],[TS;ef;e0]);
237             resilient = horzcat(["Resilient Modulus [GPa]"],[MR])
238             Creep1 = vertcat(["Time [s]","Creep Compliance [1/GPa]"],[
                    cr_point',CR]);
239             Creep2 = horzcat(["Creep Compliance [1/GPa]"; "D1"; "D0"; "m-
                    value"],[CR(end);D1;D0;m_value]);
240             xsc =  strcat("Results_", name,".xlsx");
241             xlswrite(xsc, P,'Tensile strength','A1');
242             xlswrite(xsc, tensile,'Tensile strength','E1');
243             xlswrite(xsc, energy,'Energetic analysis','A1');
244             xlswrite(xsc, resilient,'Resilient Modulus','A1');
245             xlswrite(xsc, Creep1,'Creep Copliance','A1');
246             xlswrite(xsc, Creep2,'Creep Copliance','D1');
247             %
248         end
249     case 'No'
250         cd ../
251         name = erase(string(filename), ".dat");
252         name = convertStringsToChars(name);
253         nm = name(2 : 4);
254         clear name
255         name = nm;
256         resilient = horzcat(["Resilient Modulus [GPa]"],[MR])
257         Creep1 = vertcat(["Time [s]","Creep Compliance [1/GPa]"],[cr_point',
                CR]);
258         Creep2 = horzcat(["Creep Compliance [1/GPa]";...
259             "D1";...
260             "D0";...
```

```
            "m-value"],[CR(end);D1;D0;m_value]);
        xsc =  strcat("Results_CR_MR_", name,".xlsx");
        xlswrite(xsc, resilient,'Resilient Modulus','A1');
        xlswrite(xsc, Creep1,'Creep Copliance','A1');
        xlswrite(xsc, Creep2,'Creep Copliance','D1');
end
```

A.2.3. Comparison among the analysed materials

```
clear all
clc
close all
prompt = {'How many materials do you have to compare?'};
tit = 'Mandatory!!!';
dims = [1 35];
definput = {''};
s = inputdlg(prompt,tit,dims,definput); % Column where I save the input
num = str2num(s{1});
for i = 1 : num
%% Import Directory and Save Path

    if i == 1
        %
        cs = ('C:\Users\Antonio Roberto\Desktop\Programmi_Matlab_completi\
            SetUp IDT SuperPave\Definitive_Software');
        selpath = uigetdir('C:\Users\Antonio Roberto\Desktop');    % Select
            folder where you have saved your files
        D = dir(fullfile(selpath,'*.xlsx'));
        cd(selpath)
        pn = find(selpath == '\', 1, 'last');
        selpath1 = selpath(1 : pn-1);
        name(i) =  convertCharsToStrings(selpath(pn + 1 : end));
        for ii = 1:length(D)
            filename = D(ii).name;                    % Save only name's column
            if exist(filename)==2
                [~ , sheets] = xlsfinfo(filename);
                M = importdata(filename);
                if length(sheets) == 3
                    MR(ii) = M.data.ResilientModulus;
                    CR(ii) = M.data.CreepCopliance(1,5);
                    cr_curve(:,ii) = M.data.CreepCopliance(2:end,2);
                    cr_point = M.data.CreepCopliance(2:end,1);
                    D1(ii) = M.data.CreepCopliance(2,5);
                    m_value(ii) = M.data.CreepCopliance(4,5);
                else
                    MR(ii) = M.data.ResilientModulus;
                    CR(ii) = M.data.CreepCopliance(1,5);
                    cr_curve(:,ii) = M.data.CreepCopliance(2:end,2);
                    cr_point = M.data.CreepCopliance(2:end,1);
                    D1(ii) = M.data.CreepCopliance(2,5);
                    m_value(ii) = M.data.CreepCopliance(4,5);
                    TS(ii) = M.data.TensileStrength(1,6);
                    ef(ii) = M.data.TensileStrength(2,6);
                    FE(ii) = M.data.EnergeticAnalysis(1,1);
                    EE(ii) = M.data.EnergeticAnalysis(2,1);
                    DCSE(ii) = M.data.EnergeticAnalysis(3,1);
                    A(ii) = M.data.EnergeticAnalysis(6,1);
                    DCSE_min(ii) = M.data.EnergeticAnalysis(4,1);
```

```
                    ER(ii) = M.data.EnergeticAnalysis(5,1);
                end
            end
        end
%% Statistical analysis

        if TS(1,1) == 0
            TS = TS(2:end);
            ef = ef(2:end);
            FE = FE(2:end);
            EE = EE(2:end);
            DCSE = DCSE(2:end);
            A = A(2:end);
            DCSE_min = DCSE_min(2:end);
            ER = ER(2:end);
        end
        % Avarage values
        MR_a(i) = mean(MR);
        CR_a(i) = mean(CR);
        D1_a(i) = mean(D1);
        m_value_a(i) = mean(m_value);
        TS_a(i) = mean(TS);
        ef_a(i) = mean(ef);
        FE_a(i) = mean(FE);
        EE_a(i) = mean(EE);
        DCSE_a(i) = mean(DCSE);
        A_a(i) = mean(A);
        DCSE_min_a(i) = mean(DCSE_min);
        ER_a(i) = mean(ER);
        [stats_cr, ~] = controlchart(cr_curve,'display', 'off')
        cr_curve_a(:,i) = stats_cr.mean;
        cr_curve_er(:,i) = 2*stats_cr.std;
        % Error
        MR_er(i) = 2 * std(MR);
        CR_er(i) = 2 * std(CR);
        D1_er(i) = 2 * std(D1);
        m_value_er(i) = 2 * std(m_value);
        TS_er(i) = 2 * std(TS);
        ef_er(i) = 2 * std(ef);
        FE_er(i) = 2 * std(FE);
        EE_er(i) = 2 * std(EE);
        DCSE_er(i) = 2 * std(DCSE);
        A_er(i) = 2 * std(A);
        DCSE_min_er(i) = 2 * std(DCSE_min);
        ER_er(i) = 2 * std(ER);
    else
        selpath = uigetdir(selpath1);
        D = dir(fullfile(selpath,'*.xlsx'));
        cd(selpath)
        pn = find(selpath == '\', 1, 'last');
        selpath1 = selpath(1 : pn-1)
        name(i) =  convertCharsToStrings(selpath(pn + 1 : end));
        for ii = 1:length(D)
            filename = D(ii).name;                    % Save only name's column
            if exist(filename)==2
                [~ , sheets] = xlsfinfo(filename);
                M = importdata(filename);
                if length(sheets) == 3
```

```
                    MR(ii) = M.data.ResilientModulus;
                    CR(ii) = M.data.CreepCopliance(1,5);
                    cr_curve(:,ii) = M.data.CreepCopliance(2:end,2);
                    cr_point = M.data.CreepCopliance(2:end,1);
                    D1(ii) = M.data.CreepCopliance(2,5);
                    m_value(ii) = M.data.CreepCopliance(4,5);
                else
                    MR(ii) = M.data.ResilientModulus;
                    CR(ii) = M.data.CreepCopliance(1,5);
                    cr_curve(:,ii) = M.data.CreepCopliance(2:end,2);
                    cr_point = M.data.CreepCopliance(2:end,1);
                    D1(ii) = M.data.CreepCopliance(2,5);
                    m_value(ii) = M.data.CreepCopliance(4,5);
                    TS(ii) = M.data.TensileStrength(1,6);
                    ef(ii) = M.data.TensileStrength(2,6);
                    FE(ii) = M.data.EnergeticAnalysis(1,1);
                    EE(ii) = M.data.EnergeticAnalysis(2,1);
                    DCSE(ii) = M.data.EnergeticAnalysis(3,1);
                    A(ii) = M.data.EnergeticAnalysis(6,1);
                    DCSE_min(ii) = M.data.EnergeticAnalysis(4,1);
                    ER(ii) = M.data.EnergeticAnalysis(5,1);
                end
            end
        end
%% Statistical analysis

        if TS(1,1) == 0
            TS = TS(2:end);
            ef = ef(2:end);
            FE = FE(2:end);
            EE = EE(2:end);
            DCSE = DCSE(2:end);
            A = A(2:end);
            DCSE_min = DCSE_min(2:end);
            ER = ER(2:end);
        end
        % Avarage values
        MR_a(i) = mean(MR);
        CR_a(i) = mean(CR);
        D1_a(i) = mean(D1);
        m_value_a(i) = mean(m_value);
        TS_a(i) = mean(TS);
        ef_a(i) = mean(ef);
        FE_a(i) = mean(FE);
        EE_a(i) = mean(EE);
        DCSE_a(i) = mean(DCSE);
        A_a(i) = mean(A);
        DCSE_min_a(i) = mean(DCSE_min);
        ER_a(i) = mean(ER);
        [stats_cr, ~] = controlchart(cr_curve,'display', 'off')
        cr_curve_a(:,i) = stats_cr.mean;
        cr_curve_er(:,i) = 2*stats_cr.std;
        % Error
        MR_er(i) = 2 * std(MR);
        CR_er(i) = 2 * std(CR);
        D1_er(i) = 2 * std(D1);
        m_value_er(i) = 2 * std(m_value);
        TS_er(i) = 2 * std(TS);
```

```
            ef_er(i) = 2 * std(ef);
            FE_er(i) = 2 * std(FE);
            EE_er(i) = 2 * std(EE);
            DCSE_er(i) = 2 * std(DCSE);
            A_er(i) = 2 * std(A);
            DCSE_min_er(i) = 2 * std(DCSE_min);
            ER_er(i) = 2 * std(ER);
        end
    end
    cd ../
    %% Plot results

    % Resilient modulus Plot
    bar(categorical(name),MR_a);
    hold on
    errorbar(categorical(name), MR_a, MR_er)
    ylabel('Resilient Modulus (GPa)');
    hfig=figure(1)
    set( hfig , ...
        'Color',[1 1 1],...
        'PaperType','b5',...
        'PaperSize',[25.00 17.60 ],...
        'PaperUnits', 'centimeters',...
        'PaperPositionMode','manual',...
        'PaperPosition', [0 1 13.5 7],... %image dimention
        'InvertHardcopy','off');
    set(gcf,'Name','Resilient modulus bar')
    print(gcf, '-dpdf', '-painters', get(gcf,'Name'));
    close (hfig)
    % Tensile Strength
    bar(categorical(name),TS_a);
    hold on
    errorbar(categorical(name), TS_a , TS_er)
    ylabel('Tensile_Strength (MPa)');
    hfig=figure(1)
    set( hfig , ...
        'Color',[1 1 1],...
        'PaperType','b5',...
        'PaperSize',[25.00 17.60 ],...
        'PaperUnits', 'centimeters',...
        'PaperPositionMode','manual',...
        'PaperPosition', [0 1 13.5 7],... %image dimention
        'InvertHardcopy','off');
    set(gcf,'Name','Tensile_Strength_bar')
    print(gcf, '-dpdf', '-painters', get(gcf,'Name'));
    close (hfig)
    % Creep Compliance
    bar(categorical(name),CR_a);
    hold on
    errorbar(categorical(name), CR_a , CR_er)
    ylabel('Creep Compliance (1/GPa)');
    hfig=figure(1)
    set( hfig , ...
        'Color',[1 1 1],...
        'PaperType','b5',...
        'PaperSize',[25.00 17.60 ],...
        'PaperUnits', 'centimeters',...
        'PaperPositionMode','manual',...
```

```
222     'PaperPosition', [0 1 13.5 7],... %image dimention
223     'InvertHardcopy','off');
224 set(gcf,'Name','Creep_bar')
225 print(gcf, '-dpdf', '-painters', get(gcf,'Name'));
226 close (hfig)
227 % Creep Compliance D1
228 bar(categorical(name),D1_a);
229 hold on
230 errorbar(categorical(name),D1_a , D1_er)
231 ylabel('D1 (1/GPa)');
232 hfig=figure(1)
233 set( hfig , ...
234     'Color',[1 1 1],...
235     'PaperType','b5',...
236     'PaperSize',[25.00 17.60 ],...
237     'PaperUnits', 'centimeters',...
238     'PaperPositionMode','manual',...
239     'PaperPosition', [0 1 13.5 7],... %image dimention
240     'InvertHardcopy','off');
241 set(gcf,'Name','D1_bar')
242 print(gcf, '-dpdf', '-painters', get(gcf,'Name'));
243 close (hfig)
244 % m_value
245 bar(categorical(name),m_value_a);
246 hold on
247 errorbar(categorical(name), m_value_a , m_value_er)
248 ylabel('m value');
249 hfig=figure(1)
250 set( hfig , ...
251     'Color',[1 1 1],...
252     'PaperType','b5',...
253     'PaperSize',[25.00 17.60 ],...
254     'PaperUnits', 'centimeters',...
255     'PaperPositionMode','manual',...
256     'PaperPosition', [0 1 13.5 7],... %image dimention
257     'InvertHardcopy','off');
258 set(gcf,'Name','m_value_bar')
259 print(gcf, '-dpdf', '-painters', get(gcf,'Name'));
260 close (hfig)
261 % Fracture Energy
262 bar(categorical(name),FE_a);
263 hold on
264 errorbar(categorical(name), FE_a , FE_er)
265 ylabel('Fracture Energy (kJ/m^3)');
266 hfig=figure(1)
267 set( hfig , ...
268     'Color',[1 1 1],...
269     'PaperType','b5',...
270     'PaperSize',[25.00 17.60 ],...
271     'PaperUnits', 'centimeters',...
272     'PaperPositionMode','manual',...
273     'PaperPosition', [0 1 13.5 7],... %image dimention
274     'InvertHardcopy','off');
275 set(gcf,'Name','Fracture_Energy_bar')
276 print(gcf, '-dpdf', '-painters', get(gcf,'Name'));
277 close (hfig)
278 % Elastic Energy
279 bar(categorical(name),EE_a);
```

```
hold on
errorbar(categorical(name), EE_a , EE_er)
ylabel('Elastic Energy (kJ/m^3)');
hfig=figure(1)
set( hfig , ...
    'Color',[1 1 1],...
    'PaperType','b5',...
    'PaperSize',[25.00 17.60 ],...
    'PaperUnits', 'centimeters',...
    'PaperPositionMode','manual',...
    'PaperPosition', [0 1 13.5 7],... %image dimention
    'InvertHardcopy','off');
set(gcf,'Name','Elastic_Energy_bar')
print(gcf, '-dpdf', '-painters', get(gcf,'Name'));
close (hfig)
% Dissipated Creep Strain Energy
bar(categorical(name),DCSE_a);
hold on
errorbar(categorical(name), DCSE_a , DCSE_er)
ylabel('DCSE (kJ/m^3)');
hfig=figure(1)
set( hfig , ...
    'Color',[1 1 1],...
    'PaperType','b5',...
    'PaperSize',[25.00 17.60 ],...
    'PaperUnits', 'centimeters',...
    'PaperPositionMode','manual',...
    'PaperPosition', [0 1 13.5 7],... %image dimention
    'InvertHardcopy','off');
set(gcf,'Name','DCSE_bar')
print(gcf, '-dpdf', '-painters', get(gcf,'Name'));
close (hfig)
%% Creep compliance curves

Marker_Counter = 1;
Markers = {'+','o','*','x','v','d','^','s','>','<','h','p','.','_','|'};
for i = 1 : size(cr_curve_a,2)
plot(cr_point,cr_curve_a(:,i), strcat('-', Markers{Marker_Counter}))
Marker_Counter = Marker_Counter + 1;
hold on
end
legend(name', 'Location','northwest');
ylabel('Creep compliance (1/GPa)');
xlabel('Time (s)')
hfig=figure(1)
set( hfig , ...
    'Color',[1 1 1],...
    'PaperType','b5',...
    'PaperSize',[25.00 17.60 ],...
    'PaperUnits', 'centimeters',...
    'PaperPositionMode','manual',...
    'PaperPosition', [0 1 13.5 7],... %image dimention
    'InvertHardcopy','off');
set(gcf,'Name','Creep_compliance_curve')
print(gcf, '-dpdf', '-painters', get(gcf,'Name'));
close (hfig)
%% Save data

```

```
NA = ["Materials"; "Resilient Modulus (GPa)"; "Creep Compliance (1/GPA)"; "D1 (1/GPa)"; "m-value"; "Tensile Strength (MPa)"; "Failure Strain (microstrain)"; "Fracture Energy (kJ/m^3)";"Elastic Energy (kJ/m^3)"; "DCSE (kJ/m^3)"; "DCSE_min (kJ/m^3)"; "A"; "Energy Ratio"];
P = table(name',MR_a', CR_a', D1_a', m_value_a', TS_a', ef_a', FE_a', EE_a', DCSE_a', DCSE_min_a', A_a', ER_a');
P.Properties.VariableNames = NA';
    n = convertStringsToChars("Results_SuperPave_Analysis.csv");
    writetable(P,n);
```

A.3. Graphs and Charts

```
function createfigure(YMatrix1)
%CREATEFIGURE(YMatrix1)
%  YMATRIX1:  matrix of y data

%  Auto-generated by MATLAB on 18-Feb-2020 16:03:56

% Create figure
figure1 = figure;

% Create axes
axes1 = axes('Parent',figure1);
hold(axes1,'on');

% Create multiple lines using matrix input to plot
plot1 = plot(YMatrix1,'Parent',axes1);

% Create ylabel
ylabel('microstrain');

% Create xlabel
xlabel('Time (s)');

% Uncomment the following line to preserve the Y-limits of the axes
 ylim(axes1,[0 Inf]);
box(axes1,'on');
% Set the remaining axes properties
set(axes1,'FontName','Lato','FontSize',9);
% Create legend
legend1 = legend(axes1,'show');
set(legend1,'Location','northwest','FontSize',7);
```

B

Appendix

B.1. Gravity-machine draws

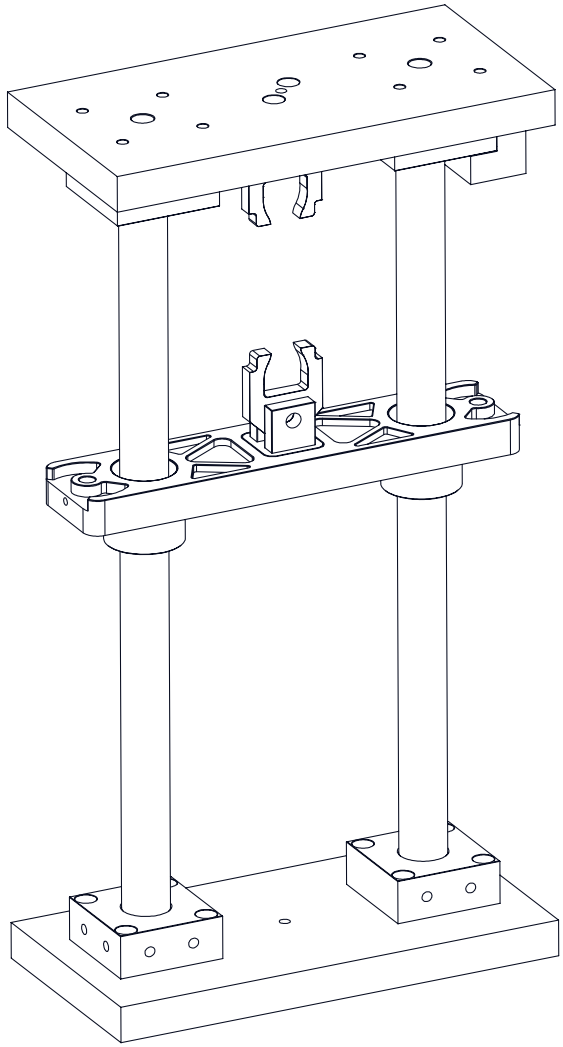

Figure B.1 Testing machine:technical draw.

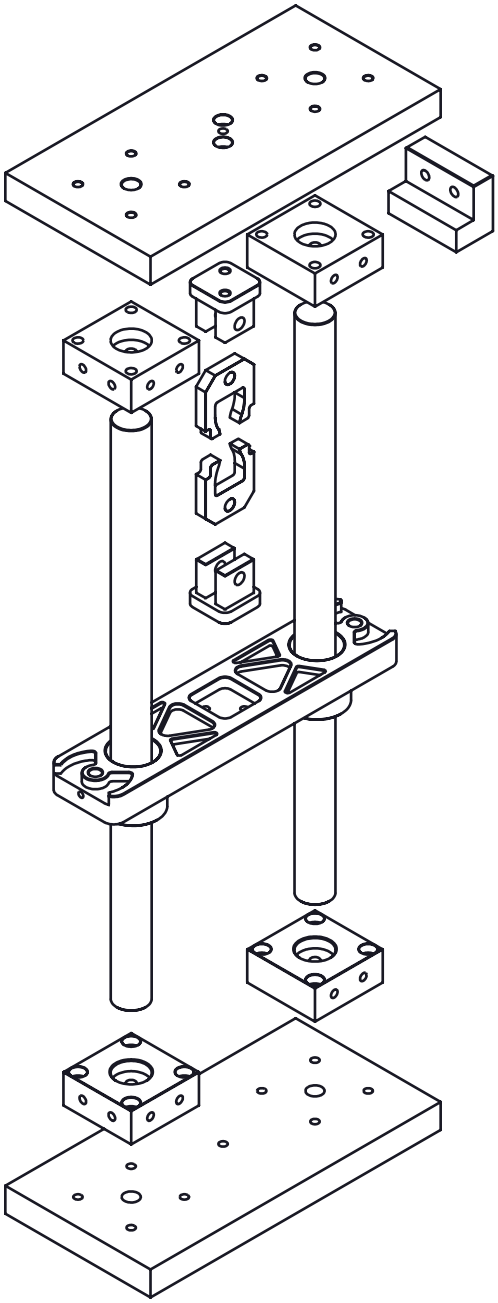

Figure B.2 Exploded-view drawing of the tensile testing machine.

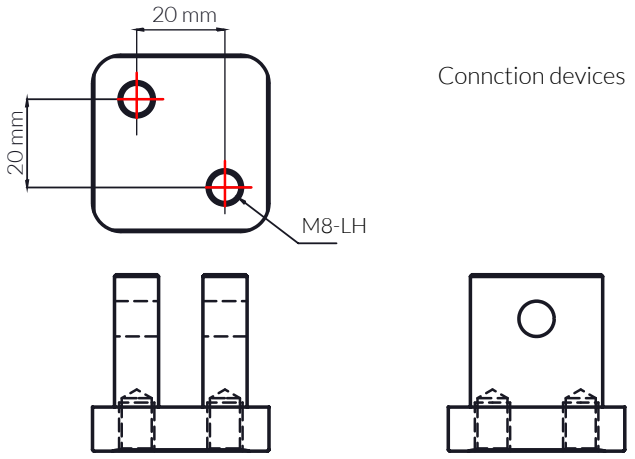

Figure B.3 Connection devices zoom

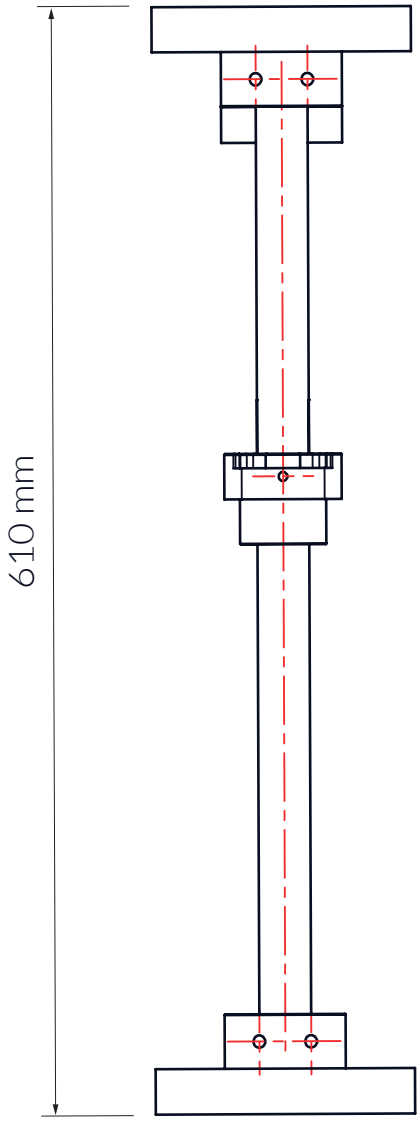

Figure B.4 Testing machine:technical draw with the measurements of the steel parts.

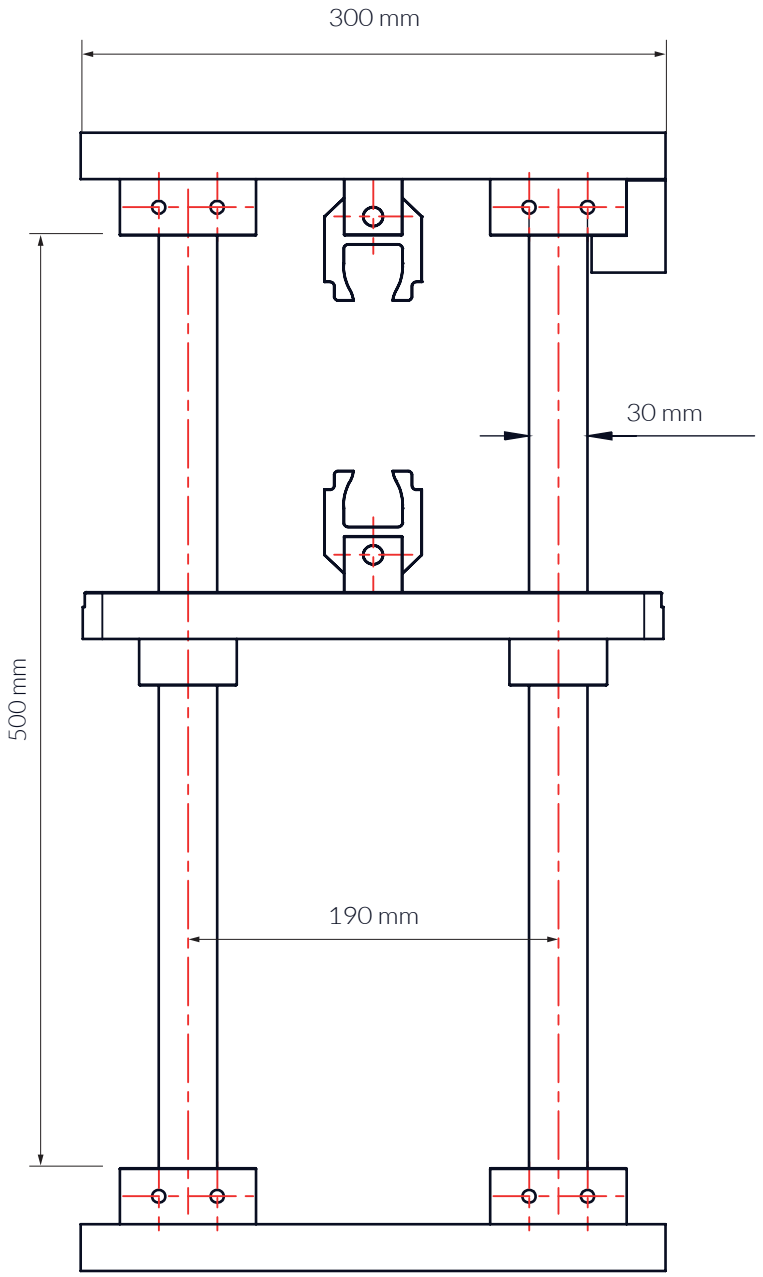

Figure B.5 Testing machine:technical draw: technical draw with the measurements of the steel parts.

Bibliography

[1] U. N. United Nations, https://www.un.org/sustainabledevelopment/news/communications-material/, 2018.

[2] EIT RawMaterials - Spring School on Circular Economy, https://eitrawmaterials.eu/events/spring-school-on-circular-economy/, 2019.

[3] Worldsteel ASSOCIATION, Steel - The permanent material in the circular economy, 2019.

[4] R. C. West, A. Copeland, High RAP Asphalt Pavements: Japanese practice - Lesson lerned, National Asphalt Pavement Association 139 (2015) 62.

[5] W. Buttlar, R. Roque, Development and evaluation of the strategic highway research program measurement and analysis system for indirect tensile testing at low temperatures, Transportation Research Record: Journal of the Transportation Research Board 1454 (1994) 163–171.

[6] Z. Zhang, R. Roque, B. Birgisson, B. Sangpetngam, Identification and verification of a suitable crack growth law., Journal of the Association of Asphalt Paving Technologists 70 (2001) 206–2041.

[7] R. Roque, B. Birgisson, B. Sangpetngam, Z. Zhang, Hot mix asphalt fracture mechanics: A fundamental crack growth law for asphalt mixtures, Journal of the Association of Asphalt Paving Technologist 71 (2002) 816–827.

[8] Y. A. Mehta, A. Nolan, E. Dubois, S. Zorn, P. Shirodkar, FHWA- NJ-2014- 002: Correlation between Multiple Stress Creep Recovery (MSCR) Results and Polymer Modification of Binder, Technical Report, Rowan University, 2014.

[9] A. Jiménez Del Barco Carrión, D. Lo Presti, G. D. Airey, Binder design of high RAP content hot and warm asphalt mixture wearing courses, Road Materials and Pavement Design 16 (2015) 460–474.

[10] W. N. Findley, J. S. Lai, K. Onaran, Creep and Relaxation of Nonlinear Viscoelastic Materials - With an Introduction to Linear Viscoelasticity, 1976.

[11] D. C. Montgomery, Introduction to Statistical Quality Control, 7 th ed., John Wiley & Sons, Inc., 2009.

[12] A. Montepara, E. Romeo, M. Isola, G. Tebaldi, The Role of Fillers on Cracking Behavior of Mastics and Asphalt Mixtures, Journal of the Association of Asphalt Pavement Technologists 80 (2011) 161–191.

[13] B. Birgisson, A. Montepara, E. Romeo, R. Roncella, R. Roque, G. Tebaldi, An optical strain measurement system for asphalt mixtures, Materials and Structures/-Materiaux et Constructions 42 (2009) 427–441.

[14] N. Laframboise, S. Acevedo, Man versus: Mother Nature, Finance and Development 51 (2014) 44–47.

[15] B. S. Underwood, Z. Guido, P. Gudipudi, Y. Feinberg, Increased costs to US pavement infrastructure from future temperature rise, Nature Climate Change 7 (2017) 704–707.

[16] P. P. Gudipudi, B. S. Underwood, A. Zalghout, Impact of climate change on pavement structural performance in the United States, Transportation Research Part D: Transport and Environment 57 (2017) 172–184.

[17] S. A. Markolf, C. Hoehne, A. Fraser, M. V. Chester, B. S. Underwood, Transportation resilience to climate change and extreme weather events – Beyond risk and robustness, Transport Policy 74 (2019) 174–186.

[18] European Commition, COM(2015) 614 final - Closing the loop - An EU action plan for the Circular Economy, Technical Report, 2015.

[19] European Commition, COM(2018) 29 final - on a monitoring framework for the circular economy, Technical Report, 2018.

[20] European Commition, COM(2019) 190 final - on the implementation of the Circular Economy Action Plan., Technical Report, 2019.

[21] B. Underwood, Multiscale modeling approach for asphalt concrete and its implications on oxidative aging, in: Advances in Asphalt Materials, Elsevier, 2015, pp. 273–302.

[22] D. Anderson, W. Goetz, Mechanical Behavior and Reinforcement of Mineral Filler-Asphalt Mixtures : Technical Paper, Technical Report, Joint Highway Research Project, 1973.

[23] B. M. Harris, K. D. Stuart, Analysis of mineral fillers and mastics used in stone matrix asphalt, Asphalt Paving Technology: Association of Asphalt Paving Technologists-Proceedings of the Technical Sessions 64 (1996) 54–95.

[24] L. Cooley, A. M. Stroup-Gardiner, E. R. Brown, D. I. Hanson, M. O. Fletcher, Characterization of asphalt-filler mortars with superpave binder tests, Journal of Association of Asphalt Paving Technologists 67 (1998) 42–65.

[25] A. Roberto, E. Romeo, A. Montepara, R. Roncella, Effect of fillers and their fractional voids on fundamental fracture properties of asphalt mixtures and mastics, Road Materials and Pavement Design 21 (2020) 25–41.

[26] A. F. Faheem, H. U. Bahia, Modelling of Asphalt Mastic in Terms of Filler-Bitumen Interaction, Road Materials and Pavement Design 11 (2010) 281–303.

[27] A. F. Faheem, C. Hintz, H. U. Bahia, I. L. Al-Qadi, S. Glidden, Influence of Filler Fractional Voids on Mastic and Mixture Performance, Transportation Research Record: Journal of the Transportation Research Board 2294 (2012) 74–80.

[28] Y. Cheng, J. Tao, Y. Jiao, Q. Guo, C. Li, Influence of Diatomite and Mineral Powder on Thermal Oxidative Ageing Properties of Asphalt, Advances in Materials Science and Engineering 2015 (2015) 1–10.

[29] Y. Cheng, J. Tao, Y. Jiao, G. Tan, Q. Guo, S. Wang, P. Ni, Influence of the properties of filler on high and medium temperature performances of asphalt mastic, Construction and Building Materials 118 (2016) 268–275.

[30] E. Romeo, B. Birgisson, A. Montepara, G. Tebaldi, The effect of polymer modification on hot mix asphalt fracture at tensile loading conditions, International Journal of Pavement Engineering 11 (2010) 403–413.

[31] Y.-R. Kim, D. N. Little, I. Song, Effect of Mineral Fillers on Fatigue Resistance and Fundamental Material Characteristics: Mechanistic Evaluation, Transportation Research Record: Journal of the Transportation Research Board 1832 (2003) 1–8.

[32] J. Van Rompu, H. Di Benedetto, T. Gallet, G. Gauthier, New fatigue test on bituminous binders and mastics using an annular shear rheometer prototype and waves propagation, in: Advanced Testing and Characterization of Bituminous Materials, 2009.

[33] J. Van Rompu, H. Di Benedetto, M. Buannic, T. Gallet, C. Ruot, New fatigue test on bituminous binders: Experimental results and modeling, Construction and Building Materials 37 (2012) 197–208.

[34] H. Di Benedeto, Q. T. Nguyen, C. Sauzéat, Nonlinearity, Heating, Fatigue and Thixotropy during Cyclic Loading of Asphalt Mixtures, Road Materials and Pavement Design 12 (2011) 129–158.

[35] Y.-R. Kim, H.-J. Lee, Evaluation of the effect of aging on mechanical and fatigue properties of sand asphalt mixtures, KSCE Journal of Civil Engineering 7 (2003) 389–398.

[36] Y. R. Kim, D. N. Little, R. L. Lytton, J. D'Angelo, R. Davis, G. Rowe, G. Reinke, M. Marasteanu, E. Masad, R. Roque, L. Tashman, Use of dynamic mechanical analysis (DMA) to evaluate the fatigue and healing potential of asphalt binders in sand asphalt mixtures, in: Asphalt Paving Technology: Association of Asphalt Paving Technologists-Proceedings of the Technical Sessions, 2002, pp. 176–206.

[37] Y. R. Kim, D. N. Little, R. L. Lytton, Fatigue and healing characterization of asphalt mixtures, Journal of Materials in Civil Engineering 15 (2003) 75–83.

[38] R. Taylor, G. D. Airey, Influence of surface interactions between bitumen and mineral fillers on the rheology of bitumen-filler mastics, 2008.

[39] F. Cardone, F. Frigio, G. Ferrotti, F. Canestrari, Influence of mineral fillers on the rheological response of polymer-modified bitumens and mastics, Journal of Traffic and Transportation Engineering (English Edition) 2 (2015) 373–381.

[40] E. Dall'Asta, V. Ghizzardi, R. Brighenti, E. Romeo, R. Roncella, A. Spagnoli, New experimental techniques for fracture testing of highly deformable materials, Frattura ed Integrita Strutturale 10 (2016) 161–171.

[41] Y.-R. Kim, D. N. Little, Linear Viscoelastic Analysis of Asphalt Mastics, Journal of Materials in Civil Engineering 16 (2004) 122–132.

[42] A. Faheem, H. Wen, L. Stephenson, H. Bahia, Effect of Mineral Filler on Damage Resistance Characteristics of Asphalt Binders, Journal of the Association of Asphalt Paving Technologists 77 (2008).

[43] A. Faheem, H. Bahia, Conceptual phenomenological model for interaction of asphalt binders with mineral fillers, Association of Asphalt Paving Technologists 78 (2009) 679–720.

[44] B. Delaporte, H. Di Benedetto, P. Chaverot, G. Gauthier, Effect of Ultrafine Particles on Linear Viscoelastic Properties of Mastics and Asphalt Concretes, Transportation Research Record: Journal of the Transportation Research Board 2051 (2008) 41–48.

[45] B. Delaporte, J. Van Rompu, H. Di Benedetto, P. Chaverot, G. Gauthier, New procedure to evaluate fatigue of bituminous mastics using an annular shear rheometer prototype, in: Pavement Cracking: mechanisms, modeling, detection, testing and case histories, CRC Press, 2008, pp. 457–467.

[46] R. Miró, A. H. Martínez, F. E. Pérez-Jiménez, R. Botella, A. Álvarez, Effect of filler nature and content on the bituminous mastic behaviour under cyclic loads, Construction and Building Materials 132 (2017) 33–42.

[47] M. Hospodka, B. Hofko, R. Blab, Introducing a new specimen shape to assess the fatigue performance of asphalt mastic by dynamic shear rheometer testing, Materials and Structures/Materiaux et Constructions 51 (2018).

[48] O. J. Vacin, J. Stastna, L. Zanzotto, Creep Compliance of Polymer Modified Asphalt, Asphalt Mastic and Hot Mix Asphalt, Transportation Research Record Annual miting (2003).

[49] H. U. Bahia, D. I. Hanson, M. Zeng, H. Zhai, M. A. Khatri, R. M. Anderson, Characterization of Modified Asphalt Binder in Superpave Mix Design, Technical Report, 2001.

[50] ASTM D7405, Standard Test Method for Multiple Stress Creep and Recovery (MSCR) of Asphalt Binder Using a Dynamic Shear Rheometer, 2010.

[51] J. J. Williams, Two Experiments for Measuring Specific Viscoelastic Cohesive Zone Parameters, Ph.D. thesis, Texas A&M University, 2001.

[52] Y.-R. Kim, F. A. C. De Freitas, D. H. Allen, Experimental characterization of ductile fracture-damage properties of asphalt binders and mastics, 87th Annual meeting of Transportation Research Board (2008).

[53] J. Qiu, M. van de Ven, S. Wu, A. Molenaar, J. Yu, Self-healing characteristics of bituminous mastics using a modified direct tension test, Journal of Intelligent Material Systems and Structures 25 (2014) 58–66.

[54] R. Roque, B. Birgisson, C. Drakos, B. Dietrich, Development and field evaluation of energybased criteria for top-down cracking performance of hot mix asphalt, Journal of the Association of Asphalt Paving Technologists 72 (2004) 229–260.

[55] M. Thierry, M. Salomon, J. van Nunen, L. van Wassenhove, Strategic Issues in Product Recovery Management, California Management Review 37 (1995) 114–135.

[56] Thomas J. Van Dam, John T. Harvey, Stephen T. Muench, Kurt D. Smith, Mark B. Snyder, Imad L. Al-Qadi, Hasan Ozer, Joep Meijer, Prashant V. Ram, Jeffery R. Roesler, A. Kendall, Thomas J. Van Dam, John T. Harvey, Stephen T. Muench, Kurt D. Smith, Mark B. Snyder, Imad L. Al-Qadi, Hasan Ozer, Joep Meijer, Prashant V. Ram, Jeffery R. Roesler, A. Kendall, FHWA-HIF-15-002 - Towards Sustainable Pavement Systems : A Reference Document, Technical Report, 2015.

[57] A. K. Mohamed, H. A. Mahdy, K. A. Kandil, The use of waste plastics in hot asphalt mixes in Egypt, International Journal of Engineering and Advanced Technology 7 (2018) 65–69.

[58] E. Bocci, Use of ladle furnace slag as filler in hot asphalt mixtures, Construction and Building Materials 161 (2018) 156–164.

[59] E. Pasquini, G. Giacomello, M. Skaf, V. Ortega-Lopez, J. M. Manso, M. Pasetto, Influence of the Production Temperature on the Optimization Process of Asphalt Mixes Prepared with Steel Slag Aggregates Only, in: Lecture Notes in Civil Engineering, volume 48, 2020, pp. 214–223.

[60] A. Roberto, A. Montepara, E. Romeo, S. Tatalovic, The Use of a Polyethylene-Based Modifier to Produce Modified Asphalt Binders on Site, in: Lecture Notes in Civil Engineering, volume 48, 2020, pp. 346–355.

[61] A. Jimenez Del Barco-Carrion, M. Pérez-Martínez, A. Themeli, D. Lo Presti, P. Marsac, S. Pouget, F. Hammoum, E. Chailleux, G. D. Airey, Evaluation of bio-materials' rejuvenating effect on binders for high-reclaimed asphalt content mixtures, Materiales de Construccion 67 (2017) 1–11.

[62] G. Tebaldi, E. V. Dave, A. Cannone Falchetto, M. Hugener, D. Perraton, A. Grilli, D. Lo Presti, M. Pasetto, A. Loizos, K. Jenkins, A. Apeagyei, J. Grenfell, M. Bocci, Recommendation of RILEM TC237-SIB: protocol for characterization of recycled asphalt (RA) materials for pavement applications, Materials and Structures/Materiaux et Constructions 51 (2018) 1–8.

[63] H. Motz, J. Geiseler, Products of steel slags an opportunity to save natural resources, Waste Management 21 (2001) 285–293.

[64] V. Ortega-López, J. M. Manso, I. I. Cuesta, J. J. González, The long-term accelerated expansion of various ladle-furnace basic slags and their soil-stabilization applications, Construction and Building Materials 68 (2014) 455–464.

[65] M. Pasetto, A. Baliello, E. Pasquini, M. Skaf, V. Ortega-López, Performance-Based Characterization of Bituminous Mortars Prepared With Ladle Furnace Steel Slag, Sustainability 12 (2020) 1777.

[66] M. Skaf, V. Ortega-López, J. Fuente-Alonso, A. Santamaría, J. Manso, Ladle furnace slag in asphalt mixes, Construction and Building Materials 122 (2016) 488–495.

[67] J. O. Akinmusuru, Potential beneficial uses of steel slag wastes for civil engineering purposes, Resources, Conservation and Recycling 5 (1991) 73–80.

[68] J. Setién, D. Hernández, J. González, Characterization of ladle furnace basic slag for use as a construction material, Construction and Building Materials 23 (2009) 1788–1794.

[69] I. Z. Yildirim, M. Prezzi, Chemical, mineralogical, and morphological properties of steel slag, Advances in Civil Engineering 2011 (2011).

[70] C. Shi, S. Hu, Cementitious properties of ladle slag fines under autoclave curing conditions, Cement and Concrete Research 33 (2003) 1851–1856.

[71] L. Kriskova, Y. Pontikes, Ö. Cizer, G. Mertens, W. Veulemans, D. Geysen, P. T. Jones, L. Vandewalle, K. Van Balen, B. Blanpain, Effect of mechanical activation on the hydraulic properties of stainless steel slags, Cement and Concrete Research 42 (2012) 778–788.

[72] S. Choi, J.-M. Kim, D. Han, J.-H. Kim, Hydration properties of ladle furnace slag powder rapidly cooled by air, Construction and Building Materials 113 (2016) 682–690.

[73] V. S. Ramachandran, P. J. Sereda, R. F. Feldman, Mechanism of Hydration of Calcium Oxide, Nature 201 (1964) 288–289.

[74] G. Wang, Y. Wang, Z. Gao, Use of steel slag as a granular material: Volume expansion prediction and usability criteria, Journal of Hazardous Materials 184 (2010) 555–560.

[75] J. M. Montenegro, M. Celemín-Matachana, J. Cañizal, J. Setién, Ladle Furnace Slag in the Construction of Embankments: Expansive Behavior, Journal of Materials in Civil Engineering 25 (2013) 972–979.

[76] I. M. Asi, H. Y. Qasrawi, F. I. Shalabi, Use of steel slag aggregate in asphalt concrete mixes, Canadian Journal of Civil Engineering 34 (2007) 902–911.

[77] C. Johnson, M. Kaeppeli, S. Brandenberger, A. Ulrich, W. Baumann, Hydrological and geochemical factors affecting leachate composition in municipal solid waste incinerator bottom ash Part II. The geochemistry of leachate from Landfill Lostorf, Switzerland, Journal of Contaminant Hydrology 40 (1999) 239–259.

[78] A. Y. Dayioglu, A. H. Aydilek, B. Cetin, Preventing Swelling and Decreasing Alkalinity of Steel Slags Used in Highway Infrastructures, Transportation Research Record: Journal of the Transportation Research Board 2401 (2014) 52–57.

[79] S. Wu, Y. Xue, Q. Ye, Y. Chen, Utilization of steel slag as aggregates for stone mastic asphalt (SMA) mixtures, Building and Environment 42 (2007) 2580–2585.

[80] B. L. Evangelista, L. P. Rosado, C. S. G. Penteado, Life cycle assessment of concrete paving blocks using electric arc furnace slag as natural coarse aggregate substitute, Journal of Cleaner Production 178 (2018) 176–185.

[81] P. E. B. Liz Hunt, STEEL SLAG IN HOT MIX Final Rep ort STEEL SLAG IN HOT MIX Final Report, Research Article Volume 201 (2012) 5.

[82] A. Mladenovic, J. Turk, J. Kovac, A. Mauko, Z. Cotic, Environmental evaluation of two scenarios for the selection of materials for asphalt wearing courses, Journal of Cleaner Production 87 (2015) 683–691.

[83] A. Gundla, S. Underwood, Evaluation of in situ RAP binder interaction in asphalt mastics using micromechanical models, International Journal of Pavement Engineering 18 (2015) 798–810.

[84] A. Copeland, FHWA-HRt-11-021 -Reclaimed Asphalt Pavement in Asphalt Mixtures: State of the Practice, Technical Report, 2011.

[85] D. Lo Presti, K. Vasconcelos, M. Oreškovic, G. M. Pires, S. Bressi, On the degree of binder activity of reclaimed asphalt and degree of blending with recycling agents, Road Materials and Pavement Design (2019).

[86] M. Sabouri, T. Bennert, J. Sias Daniel, Y. Richard Kim, A comprehensive evaluation of the fatigue behaviour of plant-produced RAP mixtures, Road Materials and Pavement Design 16 (2015) 29–54.

[87] J. D. Doyle, I. L. Howard, Laboratory Investigation of High RAP Content Pavement Surface Layers. Final Report FHWA/MS-DOT-RD-10-212., Technical Report, Mississippi Department of Transportation, 2010.

[88] G. W. Maupin, S. D. Diefenderfer, Final Report VTRC 08-R22 research report Evaluation of Using Higher Percentages of Recycled Asphalt Pavement in Asphalt Mixes in Virginia Virginia Transportation Research Council, Technical Report 434, 2008.

[89] G. Falla, A. Blasl, R. Millow, D. Lo Presti, Mix design considerations for asphalt wearing courses with high reclaimed asphalt content, in: 6th International Conference Bituminous Mixtures and Pavements, CRC Press, Thessaloniki, Greece, 2015, pp. 561–566.

[90] N. Bueche, A.-G. Dumont, M. Pittet, S. Bressi, Asphalt Mixture with RAP: Mix Design Optimization, in: Canestrari F., Partl M. (eds) 8th RILEM International Symposium on Testing and Characterization of Sustainable and Innovative Bituminous Materials. RILEM Bookseries, volume 11, Springer, Dordrecht, 2016, pp. 607–618.

[91] C. Celauro, C. Bernardo, B. Gabriele, Production of innovative, recycled and high-performance asphalt for road pavements, Resources, Conservation and Recycling 54 (2010) 337–347.

[92] D. Lo Presti, R. Khan, N. Abdul Hassan, G. Airey, A. Collop, Laboratory Mix Design of Asphalt Mixture Containing Reclaimed Material, Advances in Materials Science and Engineering (2014) 1–11.

[93] F. Zhou, S. Hu, G. Das, T. Scullion, High RAP Mixes Design Methodology with Balanced Performance, Technical Report, Texas Department of Transportation, Austin, Texas 78763-5080, 2011.

[94] R. West, J. R. Willis, M. Marasteanu, Improved Mix Design, Evaluation, and Materials Management Practices for Hot Mix Asphalt with High Reclaimed Asphalt Pavement Content, Technical Report January, 2013.

[95] D. Lo Presti, A. Jiménez Del Barco Carrión, G. Airey, E. Hajj, Towards 100% recycling of reclaimed asphalt in road surface courses: Binder design methodology and case studies, Journal of Cleaner Production 131 (2016) 43–51.

[96] G. M. Pires, A. Jiménez Del Barco Carrión, G. D. Airey, D. L. Pres, Maximising asphalt recycling in road surface courses: The importance of a preliminary binder design, in: Bearing Capacity of Roads, Railways and Airfields - Proceedings of the 10th International Conference on the Bearing Capacity of Roads, Railways and Airfields, BCRRA 2017, October, 2018, pp. 1225–1232.

[97] F. Preti, S. Noto, B. C. S. Gouveia, G. Tebaldi, Evaluation of reliability of RILEM fragmentation test, in: Lecture Notes in Civil Engineering, volume 48, Springer, 2020, pp. 256–263.

[98] A. Stimilli, A. Virgili, F. Canestrari, New method to estimate the "re-activated" binder amount in recycled hot-mix asphalt, Road Materials and Pavement Design 16 (2015) 442–459.

[99] A. K. Apeagyei, J. R. A. Grenfell, G. D. Airey, Influence of aggregate absorption and diffusion properties on moisture damage in asphalt mixtures, Road Materials and Pavement Design 16 (2015) 404–422.

[100] H. M. Silva, J. R. Oliveira, C. M. Jesus, Are totally recycled hot mix asphalts a sustainable alternative for road paving?, Resources, Conservation and Recycling 60 (2012) 38–48.

[101] W. N. A. Wan Azahar, M. Bujang, R. P. Jaya, M. R. Hainin, N. Ngadi, M. M. Al Bakri Abdullah, Performance of Waste Cooking Oil in Asphalt Binder Modification, Key Engineering Materials 700 (2016) 216–226.

[102] M. Sabouri, Y.-T. Choi, Y. Wang, S. Hwang, C. Baek, R. Y. Kim, Effect of Rejuvenator on Performance Properties of WMA Mixtures with High RAP Content, in: RILEM Bookseries, volume 11, 2016, pp. 473–484.

[103] D. Sun, T. Lu, F. Xiao, X. Zhu, G. Sun, Formulation and aging resistance of modified bio-asphalt containing high percentage of waste cooking oil residues, Journal of Cleaner Production 161 (2017) 1203–1214.

[104] Z. Xie, N. Tran, G. Julian, A. Taylor, L. D. Blackburn, Performance of Asphalt Mixtures with High Recycled Contents Using Rejuvenators and Warm-Mix Additive: Field and Lab Experiments, Journal of Materials in Civil Engineering 29 (2017) 04017190.

[105] G. Mazzoni, E. Bocci, F. Canestrari, Influence of rejuvenators on bitumen ageing in hot recycled asphalt mixtures, Journal of Traffic and Transportation Engineering (English Edition) 5 (2018) 157–168.

[106] H. Ziari, A. Moniri, P. Bahri, Y. Saghafi, Evaluation of performance properties of 50% recycled asphalt mixtures using three types of rejuvenators, Petroleum Science and Technology 37 (2019) 2355–2361.

[107] R. B. Ahmed, K. Hossain, Waste cooking oil as an asphalt rejuvenator: A state-of-the-art review, Construction and Building Materials 230 (2020) 116985.

[108] M. Rathore, M. Zaumanis, Impact of laboratory mixing procedure on the properties of reclaimed asphalt pavement mixtures, Construction and Building Materials 264 (2020) 120709.

[109] S. K. Pradhan, U. C. Sahoo, Effectiveness of Pongamia pinnata oil as rejuvenator for higher utilization of reclaimed asphalt (RAP) material, Innovative Infrastructure Solutions 5 (2020) 92.

[110] R. Saha, R. S. Melaku, B. Karki, A. Berg, D. S. Gedafa, Effect of Bio-Oils on Binder and Mix Properties with High RAP Binder Content, Journal of Materials in Civil Engineering 32 (2020) 04020007.

[111] R. J. Cominsky, H. Gerald A, T. W. Kennedy, M. Anderson, The superpave mix design manual for new construction and overlays (No. SHRP-A-407)., Technical Report, Washington, DC, USA, 1994.

[112] E. Romeo, Two-dimensional digital image correlation for asphalt mixture characterisation: interest and limitations, Road Materials and Pavement Design 14 (2013) 747–763.

[113] C. Haan, B. Barfield, J. Hayes, Sediment Properties and Transport, Design Hydrology and Sedimentology for Small Catchments (1994) 204–237.

[114] A. Barhoum, M. L. García-Betancourt, H. Rahier, G. Van Assche, Physicochemical characterization of nanomaterials: polymorph, composition, wettability, and thermal stability, in: Emerging Applications of Nanoparticles and Architecture Nanostructures, Elsevier, 2018, pp. 255–278.

[115] R. Roque, W. G. Buttlar, B. E. Ruth, M. Tia, S. W. Dickison, B. Reid, Evaluation of SHRP Indirect Tension Tester to Mitigate Cracking in Asphalt Pavements and Overlays., Technical Report, Final Report to the Florida Department of Transportation, 1997.

[116] R. Roque, W. G. Buttlar, Development of a measurement and analysis system to accurately determine asphalt concrete properties using the indirect tensile mode, Asphalt Paving Technology: Association of Asphalt Paving Technologists-Proceedings of the Technical Sessions 61 (1992) 304–332.

[117] R. Roque, Z. Zhang, B. Sankar, Determination of Crack Growth Rate Parameters Of Asphalt Mixtures Using the Superpave IDT, Journal of the Association of Asphalt Paving Technologists 68 (1999) 404–433.

[118] G. White, The contribution of asphalt mastic to shear resistance, in: 6th Eurasphalt & Eurobitume Congress, Czech Technical University in Prague - Central Library, 2016.

[119] Bukowski J., J. Youtcheff, Harman T., The Multiple Stress Creep Recovery (MSCR) procedures - FHWA HIF 11 038, Technical Report, Federal Highway Administration (FHWA)-Office of Pavement Technology, 2011.

[120] J. De Visscher, A. Paez-Duenas, P. Cabanillas, V. Carrera, R. Cerny, G. Durand, T. Hagner, I. Lancaster, V. Carrera, R. Cerny, G. Durand, T. Hagner, I. Lancaster, European round robin tests for the Multiple Stress Creep Recovery Test and contribution to the development of the European standard test method, in: 6th Eurasphalt & Eurobitume Congress, Czech Technical University in Prague - Central Library, 2016.

[121] G. Mazurek, M. Pszczoła, C. Szydłowski, Non-linear mastic characteristics based on the modified MSCR (multiple stress creep recovery) test, Structure and Environment 11 (2019) 23–34.

[122] R. Roque, B. Ruth, Materials Characterization and Response of Flexible Pavements at Low Temperatures, in: Proceedings of the Association of Asphalt Paving Technologists, volume 56, 1987, pp. 130–167.

[123] E. Dubois, D. Y. Mehta, A. Nolan, Correlation between multiple stress creep recovery (MSCR) results and polymer modification of binder, Construction and Building Materials 65 (2014) 184–190.

[124] C. V. Phan, H. Di Benedetto, C. Sauzéat, D. Lesueur, Influence of Hydrated Lime on Linear Viscoelastic Properties of Bituminous Mixtures, in: RILEM Bookseries, volume 11, Kluwer Academic Publishers, 2019, pp. 667–680.

[125] C. Riccardi, A. Jiménez del Barco Carrión, D. L. Presti, A. Cannone Falchetto, M. Losa, M. Wistuba, A new procedure to determine the rheological properties of RAP binder and corresponding bituminous blends, Construction and Building Materials 154 (2017) 361–372.

[126] C. Riccardi, A. Cannone Falchetto, M. P. Wistuba, Experimental investigation of rutting in the different phases of asphalt mixtures, in: RILEM Bookseries, volume 20, Springer Netherlands, 2019, pp. 105–110.

[127] G. D. Airey, A. C. Collop, S. E. Zoorob, R. C. Elliott, The influence of aggregate, filler and bitumen on asphalt mixture moisture damage, Construction and Building Materials 22 (2008) 2015–2024.

[128] M. Pasetto, A. Baliello, G. Giacomello, E. Pasquini, Rheological characterization of warm-modified asphalt mastics containing electric arc furnace steel slags, Advances in Materials Science and Engineering 2016 (2016).

[129] E. Romeo, R. Roncella, S. Rastelli, A. Montepara, Mechanical influence of mineral fillers on asphalt mixture cracking behaviour, Asphalt Pavements - Proceedings of the International Conference on Asphalt Pavements, ISAP 2014 1 (2014) 903–911.

[130] H. Di Benedetto, F. Olard, C. Sauzéat, B. Delaporte, Linear viscoelastic behaviour of bituminous materials: From binders to mixes, Road Materials and Pavement Design 5 (2004) 163–202.

[131] M. C. Teguedy, B. Blaysat, E. Toussaint, S. Moreira, S. Liandrat, M. GréDiac, Investigation of the Tensile Behavior of Recycled Asphalts in the Small-Strain Domain with the Grid Method, Experimental Mechanics 58 (2018) 1291–1304.

[132] G. D. Airey, B. Rahimzadeh, Combined bituminous binder and mixture linear rheological properties, Construction and Building Materials 18 (2004) 535–548.

[133] C. McAlinden, J. Khadka, K. Pesudovs, Precision (repeatability and reproducibility) studies and sample-size calculation, Journal of Cataract & Refractive Surgery 41 (2015) 2598–2604.

[134] A. Zanobini, B. Sereni, M. Catelani, L. Ciani, Repeatability and Reproducibility techniques for the analysis of measurement systems, Measurement 86 (2016) 125–132.

[135] D. C. Montgomery, Design and analysis of experiments, 7 th ed., John Wiley & Sons, Inc., 2008.

[136] B. Giechaskiel, P. Dilara, J. Andersson, Particle Measurement Programme (PMP) Light-Duty Inter-Laboratory Exercise: Repeatability and Reproducibility of the Particle Number Method, Aerosol Science and Technology 42 (2008) 528–543.

[137] A. Montepara, E. Romeo, B. Birgisson, G. Tebaldi, Strain Localization and Damage Distribution in SBS Polymer Modified Asphalt Mixtures, Road Materials and Pavement Design 11 (2010) 899–915.

[138] Y. Yan, F. Preti, E. Romeo, G. Lopp, G. Tebaldi, R. Roque, Fracture energy density of interstitial component of asphalt mixtures, Materials and Structures 51 (2018) 118.

[139] R. Roncella, E. Romeo, L. Barazzetti, M. Gianinetto, M. Scaioni, Comparative analysis of digital image correlation techniques for in-plane displacement measurements, 2012 5th International Congress on Image and Signal Processing, CISP 2012 (2012) 721–726.

[140] N. Hasheminejad, C. Vuye, A. Margaritis, B. Ribbens, G. Jacobs, J. Blom, W. Den bergh, J. Dirckx, S. Vanlanduit, W. Van den bergh, J. Dirckx, S. Vanlanduit, Investigation of Crack Propagation and Healing of Asphalt Concrete Using Digital Image Correlation, Applied Sciences 9 (2019) 2459.

[141] C. M. Stewart, E. Garcia, Fatigue crack growth of a hot mix asphalt using digital image correlation, International Journal of Fatigue 120 (2019) 254–266.

[142] S. Saride, V. V. Kumar, Reflection Crack Assessment Using Digital Image Analysis, 2019, pp. 139–156.

[143] EN 1993-1-1:2014, Eurocode 3: Design of structures - Part 1-1: General rules and rules for buildings, 2014.

[144] W. Van den bergh, The Effect of Ageing on the Fatigue and Healing Properties of Bituminous Mortars., Ph.D. thesis, Delft University of Technology, 2011.

[145] D. B. Sánchez, J. Grenfell, G. Airey, S. Caro, Evaluation of the degradation of fine asphalt-aggregate mixtures containing high reclaimed asphalt pavement contents, Road Materials and Pavement Design 18 (2017) 91–107.